

# **Efficient Integration of Planar Antennas Considering Electromagnetic Interactions at Board Level**

vorgelegt von  
Diplom-Ingenieur  
Florian Ohnimus  
aus Lüneburg

von der Fakultät IV - Elektrotechnik und Informatik  
der Technischen Universität Berlin  
zur Erlangung des akademischen Grades

**Doktor der Ingenieurwissenschaften**  
**- Dr.-Ing. -**

genehmigte Dissertation

Promotionsausschuss

Vorsitzender:	Prof. Dr. Bernd Tillack
1. Bericht:	Prof. Dr. Dr. E.h. Herbert Reichl
2. Bericht:	Prof. Dr. Ege Engin

Tag der wissenschaftlichen Aussprache: 1.4.2011

Berlin 2011

D 83

## Danksagung

Die vorliegende Arbeit entstand während meiner Tätigkeit als wissenschaftlicher Mitarbeiter in der Arbeitsgruppe RF & High-Speed System Design (RSD) der Abteilung System Design and Integration (SDI) am Fraunhofer-Institut für Zuverlässigkeit und Mikrointegration (IZM) und dem Forschungsschwerpunkt Technologien der Mikroperipherik der Technischen Universität Berlin.

Ich möchte mich besonders bei meinem Doktorvater und Erstgutachter, Prof. Dr. Dr. E.h. Herbert Reichl, für die Betreuung meiner Arbeit, das Feedback und die wertvollen Ratschläge bedanken. Meinem Zweitgutachter, Prof. Dr. Ege Engin, möchte ich insbesondere für die Aufnahme und Betreuung während meines zweimonatigen Aufenthalts an der San Diego State University und die Fachdiskussionen danken. Für die Übernahme des Vorsitzes des Promotionsausschusses danke ich außerdem Prof. Dr. Bernd Tillack.

Des Weiteren danke ich meinem Abteilungsleiter, Dr. Stephan Guttowski, für die Unterstützung und Schaffung eines produktiven Arbeitsklimas. Ein ganz besonderer Dank gilt meinem Mentor, Dr. Ivan Ndip, für den unermüdlichen Einsatz als Gruppenleiter, die jahrelange Betreuung und die wertvollen Ratschläge, die maßgeblich zum Gelingen und zur Qualität dieser Arbeit beigetragen haben.

Ein weiterer großer Dank gilt meinen Arbeitskollegen der Arbeitsgruppe RSD, insbesondere Dr. Gerhard Fotheringham, Uwe Maaß, Christian Tschoban, Brian Curran, Robert Erxleben, Kai Löbbicke und Micha Bierwirth für die zahlreichen Fachdiskussionen und die vielen wertvollen Anregungen, sowie auch allen Kollegen der Abteilung SDI.

Nicht zuletzt möchte ich mich bei meinen Eltern, Dietlind und Hartwig Ohnimus, und Karl-Werner Pagels bedanken, die den Grundstein meiner Ausbildung gelegt haben. Mein letzter Dank gilt meiner langjährigen Freundin, Stefanie Zingelmann, denn du hast mir immer die nötige Kraft gegeben.

## Abstract

The (quasi) millimeter-wave range provides large spectral bandwidths for wireless short range microelectronic communication systems. Efficient planar antennas, with dimensions on the order of millimeters, are integrated at board level using printed circuit board technologies, thus, facilitating the realization of compact and low cost wireless modules. However, electromagnetic interactions occurring between planar antennas and board components sharing the same substrate may detune the antenna characteristics and also cause a high amount of undesired electromagnetic coupling at board level.

Therefore, in this work, an approach for defining a block out region around the planar antenna, where no board components should be placed is developed, thereby ensuring that the antenna characteristics remain within tolerable limits when the antenna is integrated at board level. This region, bounded by what will be termed the electromagnetic antenna boundary, is determined by evaluating the reactive electromagnetic power density excited on the substrate and deducing a threshold value.

Furthermore, a method for efficient calculation of electromagnetic coupling between planar antennas and transmission lines routed outside the electromagnetic antenna boundary is developed. This method is based entirely on a post processing step to field simulations i.e., the coupling is calculated based on the previously computed field distribution excited by the antenna on the ground plane. The coupling model uses the theory of field excited transmission lines together with the Baum-Liu-Tesche integral equations for obtaining the terminal voltages of the transmission line and, hence, the coupling terms.

Finally, planar shielding configurations including a mushroom-type electromagnetic bandgap structure and a surface wave reduced patch antenna, suitable for integration on low cost printed circuit boards, were implemented, characterized and compared.

Based on the proposed approaches, methods and results presented in this work, numerical full-wave simulation efforts as well as trial-and-error iterations are considerably reduced during the integration of planar antennas, thereby saving time and cost during the design process of compact wireless modules.

## Zusammenfassung

Der Quasi-Millimeterwellenbereich bietet große spektrale Bandbreiten für drahtlose mikroelektronische Kommunikationssysteme zum Datenaustausch über kurze Entfernungen. Effiziente Planarantennen, mit Abmessungen von einigen Millimetern, werden mittels Leiterplattentechnologien auf Board-Ebene integriert und ermöglichen somit die Realisierung von kompakten und kostengünstigen drahtlosen Funkmodulen. Jedoch führen elektromagnetische Interaktionen zwischen Planarantennen und Board-Komponenten auf demselben Substrat zu einer möglichen Verstimmung der Antennencharakteristika und verursachen ein hohes Maß an elektromagnetischer Kopplung auf Board-Ebene.

Aus diesem Grund wird in dieser Arbeit ein neuer Ansatz zur Definition einer Blockout-Region um die Planarantenne entwickelt, innerhalb der keine Board-Komponenten platziert werden sollten, um die Antennencharakteristika nach der Integration auf Board-Ebene innerhalb tolerierbarer Grenzen zu halten. Der Rand dieser Region wird als elektromagnetische Antennenumgrenzung (engl., electromagnetic antenna boundary) bezeichnet und wird durch die Evaluierung der von der Antenne angeregten reaktiven elektromagnetischen Leistungsdichte auf dem Substrat sowie der Festlegung eines Schwellwertes ermittelt.

Des Weiteren wird eine Methode zur effizienten Berechnung der elektromagnetischen Kopplung zwischen Planarantennen und Transmissionsleitungen, die außerhalb der elektromagnetischen Antennenumgrenzung geroutet werden, entwickelt. Diese Methode basiert ausschließlich auf einem Post-Prozess-Schritt zu Feldsimulationen, d.h. die Kopplung wird basierend auf der zuvor simulierten von der Antenne auf der Massefläche angeregten Feldverteilung berechnet. Das Kopplungsmodell benutzt die Theorie der feldangeregten Transmissionsleitungen zusammen mit den Baum-Liu-Tesche Integralgleichungen, um die Terminalspannungen der Transmissionsleitung und somit die Kopplungsterme zu erhalten.

Zuletzt wurden Planar-Schirmungskonfigurationen einschließlich einer pilzartigen elektromagnetischen Bandsperre und einer oberflächenwellenreduzierten Patch-Antenne, die zur Integration in kostengünstigen Leiterplatten geeignet sind, implementiert, charakterisiert und verglichen.

Basierend auf den in dieser Arbeit vorgeschlagenen Ansätzen, Methoden und Resultaten, werden numerische Simulationsaufwände sowie *Trial-und-Error*-Iterationen während der Integration von Planarantennen maßgeblich reduziert. Dadurch werden Zeit und Kosten in der Entwurfsphase von kompakten drahtlosen Modulen eingespart.

# Contents

<i>Danksagung</i> .....	II
Abstract .....	III
<i>Zusammenfassung</i> .....	IV
<b>1 Introduction .....</b>	<b>1</b>
1.1 Motivation .....	1
1.2 State-of-the-Art in Planar Antenna Integration at Board Level .....	4
1.2.1 Antennas and Transmission Lines.....	4
1.2.2 Techniques to Facilitate Integration .....	7
1.3 Main Contributions of Work .....	12
<b>2 Determination of Electromagnetic Boundary of Planar Antennas .....</b>	<b>13</b>
2.1 Overview of Proposed Approach .....	14
2.2 Theoretical Analysis of Antenna Fields .....	15
2.2.1 Fundamentals of Antennas and Transmission Lines.....	15
2.2.2 Complex Power Density of Excited Antenna .....	22
2.2.3 Modeling and Simulation of Antenna Fields .....	32
2.2.4 Determining the Electromagnetic Antenna Boundary .....	40
2.3 Comparison of Planar Antennas and Application of Antenna Boundary .....	44
2.3.1 Patch Antenna .....	45
2.3.2 Slot Antenna .....	46
2.3.3 Dipole Antenna .....	48

2.3.4	Comparison of Antenna Characteristics.....	49
2.3.5	Deduction of Electromagnetic Antenna Boundary .....	52
2.4	Summary .....	59
<b>3</b>	<b>Calculation of Coupling to Transmission Lines .....</b>	<b>60</b>
3.1	Overview of Proposed Method .....	60
3.2	Development of Coupling Model.....	61
3.3	Quantification of Coupling Model .....	69
3.3.1	Planar Antenna to Microstrip Line Coupling.....	69
3.3.2	Spectral Response of Complete Transmission Line Path.....	73
3.3.3	Simulation Errors caused by Lumped Ports .....	75
3.3.4	Measurement Results .....	76
3.4	Summary .....	78
<b>4</b>	<b>Quantification of Planar Configurations to Reduce Coupling .....</b>	<b>79</b>
4.1	Design and Implementation of Shielding Configurations.....	80
4.1.1	Planar Electromagnetic Bandgap (EBG) Structure.....	81
4.1.2	Planar Surface Wave Reduced (SWR) Antenna .....	87
4.1.3	Comparison of Configurations and Measurement Results.....	91
4.2	Coupling between SWR Antenna and Transmission Lines .....	94
4.3	Summary .....	95
<b>5</b>	<b>Design Recommendations, Conclusions and Outlook.....</b>	<b>96</b>

Appendix 1 - Overview of Full-wave Electromagnetic Field Simulations .....	101
Appendix 2 - Examination of Numerical Solution Accuracy .....	105
Appendix 3 - Microstrip Transmission Line Parameters .....	109
Appendix 4 - Prototyping and Measurement of Planar Structures.....	110
References .....	113
List of Figures .....	122
List of Tables.....	127
Short Biography and List of Publications .....	128

# 1 Introduction

## 1.1 Motivation

Over the past decade, the wireless market has been one of the main driving forces for low cost and high performance microelectronic equipment. The recent advances in system in package (SIP) technologies as well as in analog radio frequency (RF) front-end components, such as low noise amplifiers, power amplifiers, mixers, voltage controlled oscillators and frequency dividers, are paving the way for low cost and broadband wireless communication applications up into the millimeter-wave region [1-9]. The demand for even higher data-rates, lower power consumption and more size reduction is increasing rapidly. This trend is expected to continue in the future.

With the deployment of cellular networks for mobile terminals, there is an increasing interest in facilitating high data-rates over short distances of several meters. Examples of applications are wireless local/personal area networks (WLAN/WPAN), wireless sensor networks (WSN), high definition (HD) video streaming and wireless high speed data synchronization. Wireless systems operating in the (quasi) millimeter-wave range have distinct advantages over systems operating at lower microwave frequencies below 10 GHz:

- There is a vast amount of spectral bandwidth available at (quasi) millimeter-wave frequencies. The bandwidth can be exploited for very high data-rates.
- The required antenna size for efficient operation scales proportionally with the operating wavelength. Integrated antennas become physically smaller with increasing frequency potentially allowing for a high degree of system miniaturization.
- Planar antenna designs have been demonstrated with acceptable radiation performance at millimeter-wave frequencies. These configurations can be manufactured using low cost printed circuit board (PCB) technologies.

A desirable operation frequency is 24 GHz, where an unlicensed industrial, scientific and medical (ISM) frequency band is available. It offers a bandwidth of 250 MHz for communication and radar applications and is allocated by the International Telecommunication Union (ITU). Consequently, there have been numerous research activities



especially in the field of short range radar [10-22]. Strictly speaking, the millimeter-wave range spans from 30 GHz to 300 GHz. However, millimeter-wave specific challenges, such as surface wave propagation in substrates, also exist at 24 GHz considering typical PCB dimensions and materials.

Miniaturization is one of the key enablers for reducing cost and increasing performance of RF analog and high speed digital components. It is desirable to integrate analog and digital functions including the antenna at board level in close proximity to save space and obtain a high integration density. A conventional low cost integration concept of a wireless system is schematically shown in Figure 1.

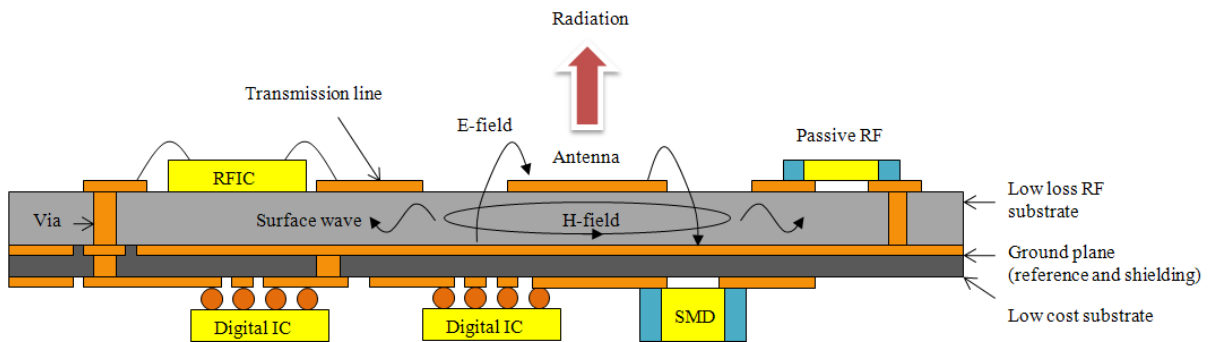


**Figure 1: Illustration of a compact wireless module based on a low cost PCB configuration.**

The RF front-end components are separated from the digital baseband components by the ground plane, which also acts as a low impedance reference for the transmission lines and supply voltages. The planar antenna is integrated together with the RF components on a low loss dielectric substrate. In order to reduce the manufacturing cost, the RF substrate is designed with only two metallization layers. The digital components, on the other hand, are integrated on a low cost substrate, such as FR4, which is placed below the ground plane. Such a configuration can be manufactured using standard PCB technologies.

The ideal integrated antenna is electromagnetically isolated from the board i.e., the signal fed to the antenna is radiated into a space wave with an efficiency of 100 %. Also, the antenna parameters, such as the input impedance and radiation patterns, are ideally independent of the board environment. However, in the case of a real antenna, the electromagnetic interactions between the antenna, the board as well as other system components, especially transmission lines, cannot be neglected. Furthermore, as the integration density and operating frequencies

increase, more electromagnetic coupling between the integrated antenna and transmission lines occurs, degrading system performance.

In order to illustrate this, consider the coupling between two 50  $\Omega$  microstrip transmission line segments compared to the coupling between a patch antenna and a microstrip transmission line segment operating at 24 GHz. In Figure 2, the simulation results of the coupling coefficients  $S_{21}$  in dependency of the edge-to-edge separation distance  $d$  are shown. The patch antenna and microstrip line segments have a length  $l=3.125$  mm and are placed on a 250  $\mu\text{m}$  thick grounded substrate with a relative permittivity of 3.75 and a dissipation factor of 0.006. These are common RF substrate parameters. Ports are placed at both ends of the transmission lines and at the end of the antenna feeding line.

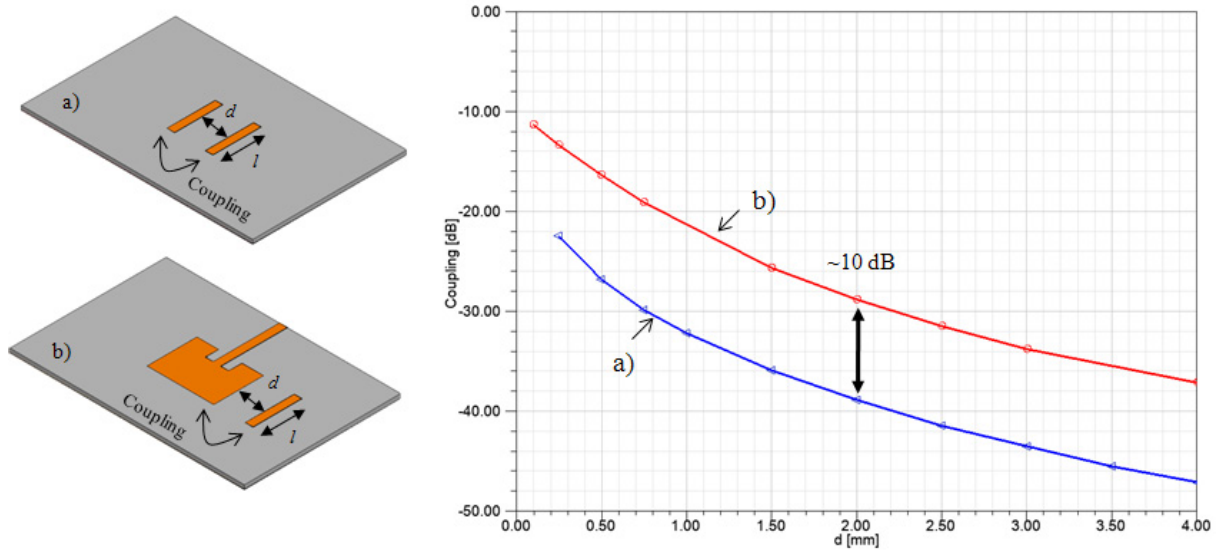


**Figure 2: Coupling between: (a) two transmission lines; and (b) a patch antenna and a transmission line at 24 GHz.**

It is observed that the coupling between the patch antenna and the transmission line segment is significantly higher (more than 10 dB) compared to the coupling between the two parallel transmission line segments. This results from the resonance nature of the antenna i.e., the excited electric and magnetic fields of the antenna are orders of magnitude higher than those on the transmission line. Therefore, the coupling between planar antennas and neighboring transmission lines must be considered as a major contributor to electromagnetic reliability (EMR) issues at board level. Controlling EMR issues is essential for the realization of compact wireless modules operating in the (quasi) millimeter-wave frequency bands and beyond.

## 1.2 State-of-the-Art in Planar Antenna Integration at Board Level

One of the challenges in integrating planar antennas in proximity to other board components on the same substrate is controlling undesired electromagnetic coupling. This undesired coupling can originate in the near- and far-field regions of the antenna. Unlike at lower frequencies, the far-field condition is met at board level in wireless modules operating at (quasi) millimeter-wave frequencies. This section gives an overview of the state-of-the-art in planar antenna design, planar transmission line analysis as well as techniques to facilitate antenna integration by reducing undesired coupling. The focus is on configurations, which can be manufactured using only two metallization layers on one dielectric substrate in low cost PCB technology.

### 1.2.1 Antennas and Transmission Lines

In recent years, research has focused on the design of planar passive components including antennas and transmission lines to facilitate (quasi) millimeter-wave modules using low cost PCB technologies. Up to date, a myriad of different planar antenna configurations have been proposed and demonstrated. The proposed planar antennas basically comprise three fundamental configurations. These include patch [23, 24], slot [25-27], and dipole [28-30] antenna types. Figure 3 shows an illustration of these three fundamental configurations with excitation voltage  $U$ .

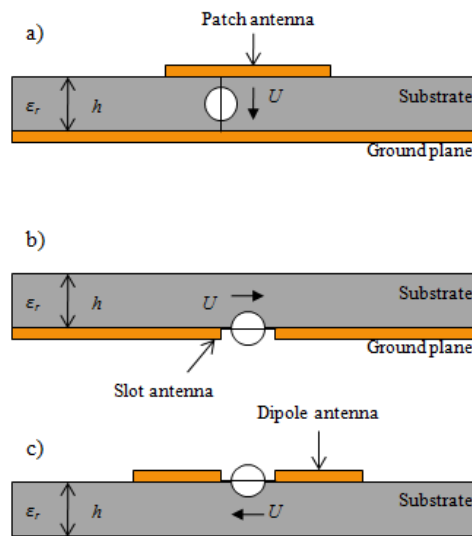


**Figure 3:** Cross sections of the three fundamental antenna types: (a) patch antenna on grounded substrate; (b) slot antenna in ground plane; and (c) dipole antenna on ungrounded substrate.

The patch antenna is excited with a voltage between the patch and the ground plane. The slot antenna, comprising a slot in the ground plane, is excited with a voltage across the slot in the ground plane. The dipole antenna, comprising two planar strips, is ideally operated without the presence of a ground plane to reduce the effects on undesired image currents.

Slot and patch antennas are unbalanced configurations and are generally fed through single ended transmission lines. Dipoles are balanced antennas, which are fed through differential transmission lines. A balun is required when the dipole is fed through a single ended transmission line.

These fundamental antenna configurations can be tailored to achieve characteristics such as: (1) high gain; (2) high efficiency/bandwidth; and (3) electronic reconfigurability, or a combination of these.

- 1) High gain has been achieved by grouping single antenna elements in an array configuration and designing the feeding network in such a way that the radiated fields produced by the current distribution on the individual elements are superimposed in phase for the desired angle of high gain (constructive interference). Examples of such configurations are single layer patch antenna arrays [31, 32], multilayer configurations including aperture coupled patches [33] as well as configurations comprising alternatively arranged electromagnetically coupled patches [34, 35].

Other designs have exploited dielectric lenses to achieve high gain in direction normal to the substrate by focusing the radiation [36].

For high gain operation in lateral direction (end-fire radiation), planar Yagi-Uda arrays [20] have also been proposed.

- 2) Dielectric losses in the substrate, which increase with frequency, cause a reduction of the antenna efficiency. Elevated patch antennas supported by metal stubs [37, 38] have been proposed, significantly improving both bandwidth and efficiency. The bandwidth is simultaneously increased by this because the effective permittivity underneath the patch is also reduced.

To overcome the bandwidth limitation imposed by substrates with a high dielectric constant yet low losses (e.g., ceramics), stacked patch configurations have been demonstrated [17].

- 3) The gain of an antenna is a passive quantity. Therefore, a high gain results in reduced space coverage and poses orientation restrictions for wireless modules. As a result, electronic beam reconfigurability is desirable in many applications to compensate the reduced space coverage by scanning the environment. Also, for many radar applications, beam steering is of fundamental importance to obtain an angular resolution. Multibeam radiation patterns and directivity diversity have been demonstrated [39]. Electronically reconfigurable radiation patterns have also been demonstrated [40, 41].

In conclusion, there has been much research in the field of tailoring and improving the characteristics of planar antennas suitable for low cost PCB applications.

However, up to date, electromagnetic interactions occurring between the excited antenna fields and board components, potentially resulting in a degradation of the antenna parameters, have not received much attention. Reports of a study on a 2.4 GHz patch antenna and a microstrip transmission line in close proximity [42] have shown that the antenna and transmission line parameters are degraded if the transmission line is routed too close to the antenna. Hence, the antenna cannot be treated as an isolated component as defined by its geometrical configuration.

The concept of defining electrical boundaries was introduced in [43, 44]. In these works, a methodology was developed for defining the electrical boundaries of geometrical discontinuities (such as transmission line bends, vias, wire bonds, bumps etc.) along a complete signal path at chip, package and board level. The main idea is that the electrical length of a component extends until the reactive power excited by the component (through higher order modes) diminishes. Defining these electrical boundaries enables the components to be analyzed independently without considering the impact of other components in the immediate vicinity. This leads to a better understanding of their electromagnetic behavior and also facilitates the development of design rules for integration. However, integrated planar antennas were not considered.

Planar transmission lines routed at board level are essential components of wireless modules required for signal distribution purposes as well as for antenna feeding lines. Transmission lines are placed directly on the substrate as conducting strips, representing signal lines, and are referenced to the ground plane. In the case of a microstrip line, the ground plane is situated underneath the substrate below the signal line. The ground plane of the coplanar waveguide, on the other hand, is situated in the same plane as the signal line and separated by

a gap, thus, requiring only one metallization layer. These two configurations are the most commonly used impedance controlled transmission lines in low cost PCB applications. However, their open field nature makes these transmission lines vulnerable towards undesired coupling through neighboring board components, such as the antenna. To date, single and coupled transmission lines have been thoroughly modeled and analyzed [45]. Based on the telegrapher's equations, analytical and simulation techniques have been employed to extract the propagation constant and impedance as well as the characteristic per-unit-length parameters of single and coupled transmission lines.

Coupling from external fields to transmission lines has also been analyzed. Formulations for the equivalent sources of the inhomogeneous telegrapher's equations of transmission lines have been developed [46-55]. Together with the Baum-Liu-Tesche (BLT) integral equations, coupling from external plane waves has been efficiently calculated [56]. In [57], an approach for assessing coupling between integrated mobile phone antennas and PCB transmission lines together with a fitting algorithm is proposed.

However, although techniques for the calculation of coupling between transmission lines (crosstalk) and from external fields to transmission lines have been proposed, no techniques are available for calculating coupling between planar antennas and transmission lines sharing the same substrate apart from complete time and resource consuming full-wave field simulations. As was shown previously, this coupling can be significantly higher than crosstalk between neighboring transmission lines. These aspects are essential for the integration of planar antennas in compact wireless modules at board level.

### **1.2.2 Techniques to Facilitate Integration**

Planar antennas are printed directly on dielectric substrates. Grounded and ungrounded substrates are capable of guiding electromagnetic energy in the form of surface waves [58]. These surface waves have been thoroughly analyzed in the context of antenna arrays i.e., multiple antenna elements grouped together on the same substrate. Surface waves are undesirable for array applications because they result in a reduction of the array gain. A percentage of the power is coupled into a surface wave mode and not launched into the space wave mode. Furthermore, based on analyses of the coupling between rectangular patch antennas [58], ring shaped patch antennas [59] and slot antenna arrays [60], it was concluded that the primary reason for an increased mutual coupling between these antenna elements is surface wave excitation and propagation in the substrate. Reflections and stray radiation of the

surface waves at the substrate edges also distort the radiation pattern. Moreover, antenna array configurations suffer from impedance mismatch at the antenna feeding points caused by mutually coupled surface waves. Altogether, surface waves are considered as one of the primary coupling mechanisms at board level.

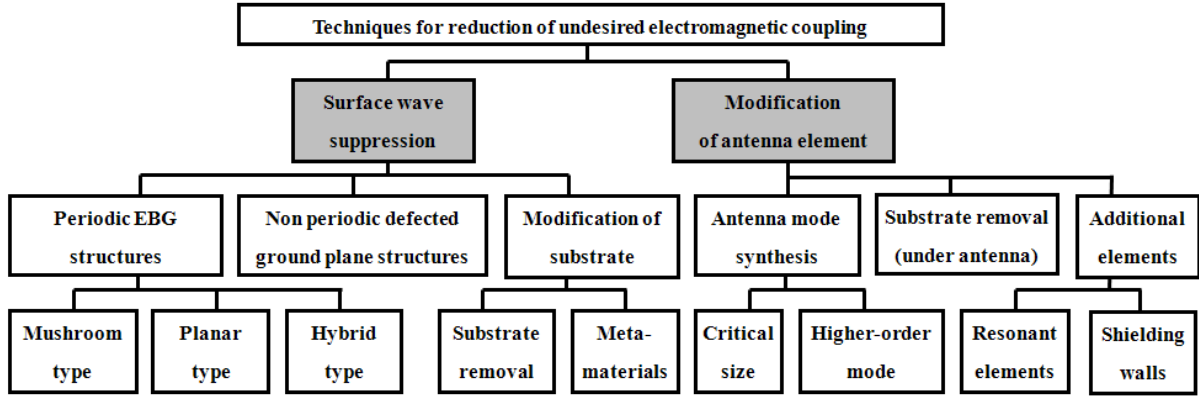


**Figure 4: Classification of techniques for the reduction of undesired electromagnetic coupling caused by surface waves.**

Therefore, in order to facilitate the integration of planar antennas, research has focused on techniques for the reduction of undesired coupling between antenna elements caused by surface waves. The primary motivation for this research has been in the field of improving antenna array performance. Figure 4 shows an overview and classification of the state-of-the-art techniques that have been proposed and studied so far.

Basically, the techniques can be grouped into two categories. These include techniques for surface wave suppression in the substrate and techniques by which the antenna elements are modified for reduced surface wave excitation.

### 1.2.2.1 Surface Wave Suppression

One approach to reduce undesired electromagnetic coupling is to suppress the surface wave in the substrate once it has been excited by the antenna.

Figure 5 shows an illustration of the different techniques for surface wave suppression in substrates. The three main techniques that have been studied in literature include: (1) integration of electromagnetic bandgap structures (EBG); (2) integration of defected ground plane structures (DGS); and (3) modification of the substrate material itself.

- 1) EBG structures have been exploited to reduce undesired mutual coupling [61, 62] between planar antennas. Within a band of frequencies, the EBG structure behaves like a distributed LC filter for the surface wave. EBG structures are designed periodically in two dimensions on the substrate. Apart from the cell dimensions and cell spacing, the number of cells determine the suppression properties [63, 64]. A commonly used geometry is the mushroom type EBG structure [65] comprising metal patches on the substrate which are shorted to the ground plane by vias. Multilayer substrate configurations have also been proposed to allow a separate optimization of patch antenna and EBG cells [66, 67].

Although the majority of studies regarding the integration of EBG structures have been conducted on patch antennas, the use of EBG structures for suppressing mutual coupling has also been studied with slot [68] and dipole [69] antennas. Since vias introduce a high cost factor for the manufacturing of the EBG structure, planar EBG structures have been proposed [70, 71]. Furthermore, the radial propagation of surface waves have led to the development of EBG structures with circular symmetry [72, 73].

Other techniques to suppress surface wave propagation in substrates include metal via fences embedded periodically in the substrate [74]. It must be noted that these via fences are not resonant cells and, thus, strictly speaking cannot be considered as EBG structures. However, because of the required periodicity, they are categorized in this group.

- 2) Another technique to reduce undesired electromagnetic coupling caused by surface waves is to implement a structure that allows controlled scattering of the surface wave. For this purpose, DGS have been proposed [75-77]. The basic idea is to realize a defect in the ground plane that disturbs the current distribution of the surface wave mode. A drawback, however, is that the scattering of surface waves distort the far-field radiation pattern.
- 3) Techniques that artificially modify the substrate e.g., with periodic rectangular holes [78], have also been studied for surface wave suppression. The basic idea here is that the effective dielectric constant of the substrate is decreased, which lowers the surface wave power propagated by the surface wave mode. Of course, complete substrate removal [79] would reduce the surface wave power effectively. From a practical point of view this approach is less feasible because the substrate also acts as a carrier in wireless modules. Research has also focused on meta-materials [80]. These materials behave as a double negative medium displaying a negative permeability and a negative permittivity.



However, these materials are also dispersive and their surface wave suppression effect is frequency band limited.

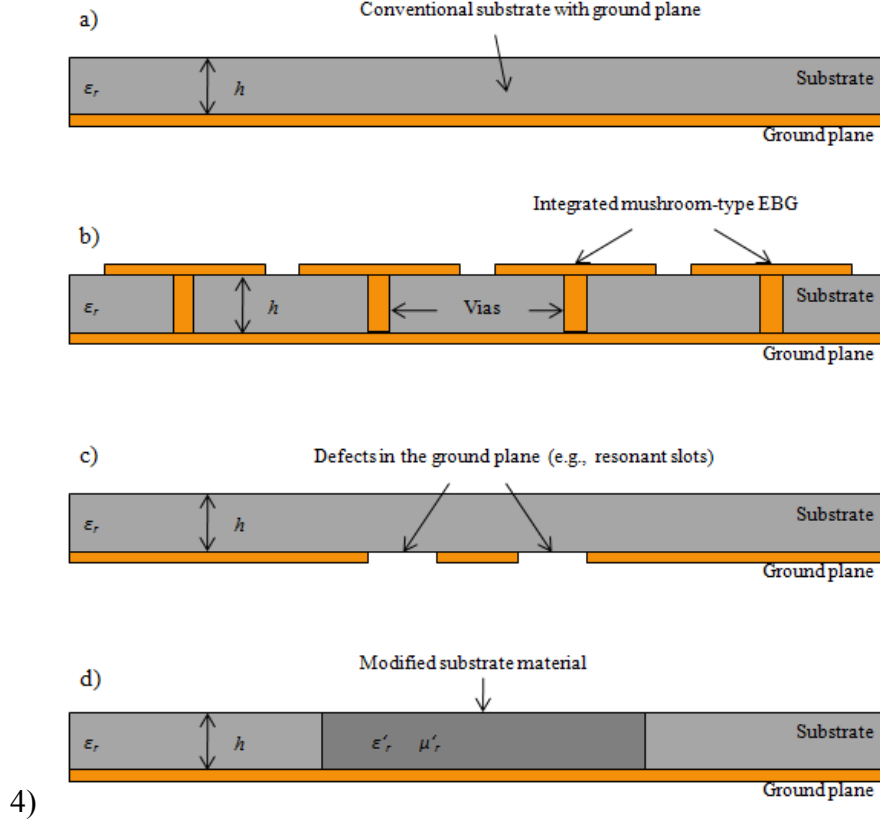


**Figure 5: Cross sections of configurations for surface wave suppression: (a) conventional substrate with ground plane; (b) integration of EBG structure; (c) integration of DGS; and (d) modification of substrate material.**

So far, the proposed techniques have mainly aimed at reducing mutual coupling in antenna arrays i.e., between the antenna elements of the array. The main drawback to this set of techniques originates from the required large lateral dimensions of these configurations. This arises from the resonance properties as well as the required periodicity needed to ensure the surface wave suppression effect. In the case of low cost board applications with only two metallization layers, these structures need to be integrated adjacent to the antenna where the surface wave propagates, typically requiring more board space than the antenna element itself.

### 1.2.2.2 Planar Antennas with Reduced Surface Wave Excitation

Some of the limitations of the surface wave suppression techniques discussed in the previous section have lead to research focusing on the modification of the antenna element itself in

such a way that the surface wave mode excitation is reduced. By this, surface wave suppressing structures placed beside the antenna can be avoided and board space is potentially saved.

The antenna elements have been modified in many ways to achieve a reduction of surface wave excitation such as: (1) antenna mode synthesis; (2) substrate removal; and (3) integration of additional elements.

- 1) A commonly employed technique is to synthesize the field distribution of the antenna mode by ensuring phase cancellation of the surface wave fields produced by the radiating apertures of the antenna [81]. For this purpose, the antenna must have a critical size [82], which is generally larger than the required physical dimensions needed to obtain the resonance condition. Therefore, the antennas need to be modified in order to obtain the resonance condition simultaneously with the surface wave field cancellation condition. Shorting posts [83] and elliptical patch geometries [84] have been proposed. Another approach to overcome the problem of simultaneously meeting the two conditions is proposed in [85] by introducing a slot antenna with two arcs.

Higher order mode patch antennas have been studied in [86] and were found to reduce surface wave excitation.

- 2) Techniques by which substrate material underneath as well as in the vicinity [87] of the antennas is selectively removed have been demonstrated to achieve a reduction of surface wave excitation. Since the surface wave uses the dielectric (grounded or ungrounded) as a waveguide, the surface wave excitation is reduced. Although the performance can be substantially improved, expensive processing technologies are required for the manufacturing.
- 3) Additional elements have also been integrated in the near-field region of patch antennas. These additional elements are considered as being part of the antenna since the input impedance and radiation pattern are strongly dependent on them. Examples of such configurations include resonant embedded strips in the substrate [88] or parasitic strips on top of the substrate [89] beside the antenna as well as an annular ring [90] or an octagonal metallic bar [91] around the antenna. Other designs have implemented a cavity comprising a metal ring shorted to the ground plane with via fences acting as shielding walls [92].

In conclusion, techniques to reduce surface wave excitation of planar antenna elements have been demonstrated. However, in general, the modifications of the antenna elements to ensure reduced surface wave mode excitation result in physically larger antenna elements compared to conventional antenna elements, thus, requiring more board space. Since the antennas are optimized for minimum surface wave excitation, co-optimization of a different antenna parameter (e.g. impedance bandwidth, gain or polarization) is generally challenging. Furthermore, the feasibility of implementing these techniques for reducing coupling to transmission lines and, hence, facilitating compact wireless modules has not been shown.

### 1.3 Main Contributions of Work

In order to support and optimize the design process of compact wireless modules with integrated planar antennas, the main contributions of this work are as follows:

- **Development of an approach for defining the block out region around planar antennas, where no board components should be placed thereby ensuring that the antenna characteristics remain within tolerable limits when the antenna is integrated at board level. This block out region is bounded by what will be termed the electromagnetic antenna boundary.**
- **Development of a method for efficient calculation of coupling from the planar antenna fields to transmission lines routed on the same substrate outside the electromagnetic antenna boundary. This method is based entirely on a post processing step to full-wave field simulations i.e., the coupling is readily determined based on the previously computed field distribution excited by the antenna on the ground plane.**
- **Quantification of planar configurations to reduce coupling suitable for implementation on low cost PCBs and evaluation of these with regards to shielding effectiveness and required board space.**

## 2 Determination of Electromagnetic Boundary of Planar Antennas

An antenna transforms the power of a guided mode on a transmission line into the power of a spherical transverse electromagnetic (TEM) space wave mode. If the antenna is a linear system and all materials are isotropic, this mode conversion process is reciprocal. The power propagated by these fundamental modes is illustrated in Figure 6 by considering a patch antenna on a grounded dielectric substrate for low cost PCB applications.

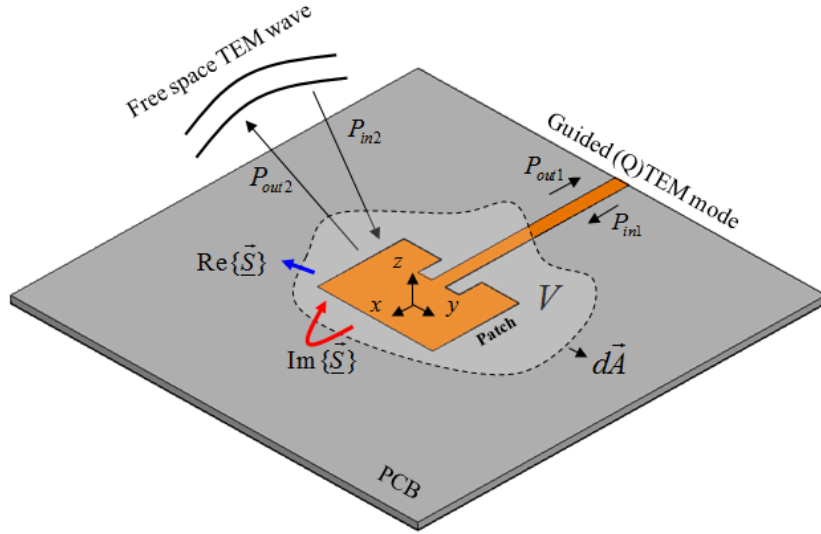


**Figure 6: Illustration of the complex power density transfer to and from a planar antenna configuration integrated on a PCB. The coordinate system is centered, and the plane  $z=0$  is on the ground plane.**

$P_{in1}$  and  $P_{out1}$  are the input and output powers of the quasi TEM mode on the microstrip transmission line, and  $P_{in2}$  and  $P_{out2}$  are the input and output powers of the TEM space wave mode in the far-field of the antenna. The mode conversion is achieved in the antenna structure where a resonance mode is excited.

However, the antenna also radiates a portion of the power in the lateral plane on the substrate where other board components are placed. This is indicated by the real power density  $\text{Re}\{\vec{S}\}$ . Furthermore, as a result of an enforced resonance condition on the planar antenna (resonator), the stored energy in the near-field region is high. This is indicated by the reactive power density  $\text{Im}\{\vec{S}\}$ . The antenna parameters depend primarily on this near-field distribution. Intuitively, the near-field region is larger than the geometrical dimensions of the antenna, loosely indicated by  $V$ . Board components placed on the substrate close to the antenna interact with the near-fields potentially altering the antenna parameters. Hence, in order to integrate

planar antennas, it is desirable to deduce a 2D block out region in the plane of the substrate around the physical antenna structure where no components should be placed such that the antenna parameters remain within acceptable limits. This region is bounded by what will be termed the electromagnetic antenna boundary.

## 2.1 Overview of Proposed Approach

An overview of the proposed approach for determining the electromagnetic antenna boundary is shown in Figure 7.

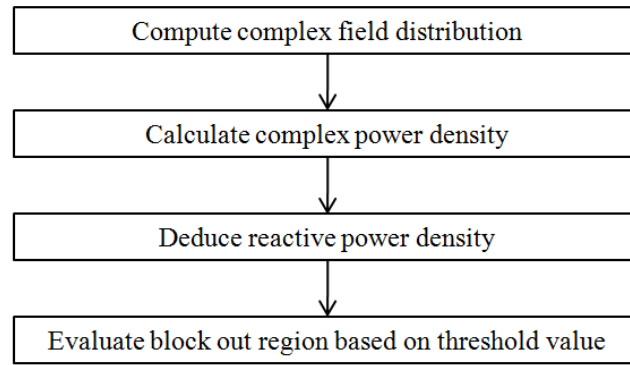


**Figure 7: Overview of approach to determine electromagnetic antenna boundary.**

In the first step, the excited fields of the planar antenna are computed on the plane of the substrate. These comprise primarily the tangential magnetic field components,  $\underline{H}_x$  and  $\underline{H}_y$ , and the normal electric field component  $\underline{E}_z$  on a grounded substrate configuration. With these field components, the complex power density  $\underline{\vec{S}}$  is calculated. The reactive power density, given by the imaginary part  $\text{Im}\{\underline{\vec{S}}\}$ , is then evaluated in order to deduce the electromagnetic antenna boundary. A threshold value of  $\text{Im}\{\underline{\vec{S}}\}$  is calculated next, and the distance from the antenna at which this threshold value is reached is determined, marking the electromagnetic antenna boundary. Board components placed beyond this distance outside the block out region will not alter the antenna characteristics significantly, and weak coupling can be assumed i.e., the secondary fields excited on the board component (victim) by the primary antenna fields (aggressor) do not alter the near-field distribution of the antenna beyond tolerable limits. Based on this approach, the antenna can be safely integrated.

In the next section, a theoretical analysis of the excited antenna fields and a characterization of the complex Poynting vector are presented.

## 2.2 Theoretical Analysis of Antenna Fields

In order to describe the behavior of electric and magnetic fields in the vicinity of an antenna, Maxwell's equations, comprising Ampere's law, Faraday's law of induction and Gauss's laws provide the foundation for further analysis [93]:

$$\vec{\nabla} \times \underline{\vec{H}} = \underline{\vec{J}} + j\omega\varepsilon\underline{\vec{E}} \quad (1)$$

$$\vec{\nabla} \times \underline{\vec{E}} = -j\omega\mu\underline{\vec{H}} \quad (2)$$

$$\vec{\nabla} \cdot \underline{\vec{H}} = 0 \quad (3)$$

$$\vec{\nabla} \cdot \underline{\vec{E}} = \underline{q} \quad (4)$$

Under the assumption of simple linear media, as is the case for the planar antennas considered in this work, the source quantities,  $\underline{\vec{J}}$  (current density) and  $\underline{q}$  (charge density), as well as the field quantities  $\underline{\vec{E}}$  (electric field) and  $\underline{\vec{H}}$  (magnetic field) are expressed in the frequency domain. Charge density and current density are related through the continuity equation.

$$\vec{\nabla} \cdot \underline{\vec{J}} = -j\omega\underline{q} \quad (5)$$

### 2.2.1 Fundamentals of Antennas and Transmission Lines

The next step in solving for the field quantities is to find general solutions to Maxwell's equations. For this purpose, wave equations are derived for free space propagation and guided modes on transmission lines.

#### 2.2.1.1 Wave Equations for General Radiation Problems

In the general analysis of radiation problems, the sources are known and must be brought into connection with the fields [94]. A common procedure is to define potential functions for the fields. The magnetic flux density has no divergence. Therefore, the magnetic field in a homogeneous space can be written as the curl of a vector potential.

$$\vec{H} = \vec{\nabla} \times \vec{A} \quad (6)$$

Inserting (6) into (2) results in the following expression:

$$\vec{\nabla} \times (\vec{E} + j\omega\mu\vec{A}) = 0 \quad (7)$$

Because the curl of the expression within the parenthesis is zero, the expression can also be written as a scalar potential:

$$\vec{\nabla} \varphi = -\vec{E} - j\omega\mu\vec{A} \leftrightarrow \vec{E} = -\vec{\nabla} \varphi - j\omega\mu\vec{A} \quad (8)$$

In order to derive the wave equation with these potential functions, equation (8) can be inserted into (1).

$$\vec{\nabla} \times \vec{\nabla} \times \vec{A} = \omega^2 \epsilon\mu\vec{A} + \vec{J} - j\omega\epsilon\vec{\nabla} \varphi \quad (9)$$

Finally, together with the vector identity (10) and the Lorentz convention (11) the inhomogeneous wave equation (12) is found.

$$\vec{\nabla} \times \vec{\nabla} \times \vec{A} = \vec{\nabla} (\vec{\nabla} \cdot \vec{A}) - \vec{\nabla}^2 \vec{A} \quad (10)$$

$$\vec{\nabla} \cdot \vec{A} = -j\omega\epsilon\varphi \leftrightarrow \varphi = -\frac{1}{j\omega\epsilon} \vec{\nabla} \cdot \vec{A} \quad (11)$$

$$\vec{\nabla}^2 \vec{A} + \omega^2 \epsilon\mu\vec{A} = -\vec{J} \quad (12)$$

The Lorentz convention is chosen based on the fact that no physical information about the divergence of the vector potential is given. Thus, it can be defined to simplify the equation.

In an analogue manner, the wave equation can also be expressed in terms of the scalar potential:

$$\vec{\nabla}^2 \underline{\varphi} + \omega^2 \epsilon \mu \underline{\varphi} = -\frac{q}{\epsilon} \quad (13)$$

The next step is to find solutions to the above wave equations. Possible solutions for both scalar and vector auxiliary functions are retarded potentials [93].

$$\underline{\vec{A}} = \frac{1}{4\pi} \iiint_V \underline{\vec{J}}(\vec{r}_s) \frac{e^{-j\beta|\vec{r}|}}{|\vec{r}|} dV \quad (14)$$

$$\underline{\varphi} = \frac{1}{4\pi\epsilon} \iiint_V q(\vec{r}_s) \frac{e^{-j\beta|\vec{r}|}}{|\vec{r}|} dV \quad (15)$$

$$\vec{r} = \vec{r}_f - \vec{r}_s \quad (16)$$

$$\beta = \omega\sqrt{\epsilon\mu} \quad (17)$$

The vectors  $\vec{r}_s$  and  $\vec{r}_f$  point to the source volume and to the point of observation, respectively. The expressions indicate that the effects need a finite time of propagation. The phase constant  $\beta$  has a negative leading sign indicating that the radiated energy moves away from its sources. Finally, the sources can be brought into connection with the fields by using (6) and (8).

$$\underline{\vec{H}} = -\frac{1}{4\pi} \iiint_V \underline{\vec{J}}(\vec{r}_s) \times \vec{\nabla} \left( \frac{e^{-j\beta|\vec{r}|}}{|\vec{r}|} \right) dV \quad (18)$$

$$\underline{\vec{E}} = -\frac{j\omega\mu}{4\pi} \iiint_V \underline{\vec{J}}(\vec{r}_s) \frac{e^{-j\beta|\vec{r}|}}{|\vec{r}|} dV - \frac{1}{4\pi\epsilon} \iiint_V q(\vec{r}_s) \vec{\nabla} \left( \frac{e^{-j\beta|\vec{r}|}}{|\vec{r}|} \right) dV \quad (19)$$

**Auxiliary Concept of Magnetic Charge:** In some radiation problems, a vector potential is introduced for the electric field by assuming there exists a magnetic current density  $\underline{\vec{J}}_m$  and, hence, a magnetic charge density  $\underline{q}_m$ . Consequently, (2) and (3) are modified accordingly.



$$\vec{\nabla} \times \vec{E} = -j\omega\mu\vec{H} + \vec{J}_m \quad (20)$$

$$\vec{\nabla} \cdot \mu\vec{H} = q_m \quad (21)$$

In analogy to the above approach for defining a vector potential for the magnetic field vector, it will be further assumed that both the electric current density and charge density are zero. Then, the electric displacement field has no divergence:

$$\vec{\nabla} \cdot \epsilon\vec{E} = 0 \quad (22)$$

A vector potential for the electric field can now be defined in analogy to (6).

$$\vec{E} = -\vec{\nabla} \times \vec{F} \quad (23)$$

With the same procedure as above for deriving (12), the wave equation for the vector potential  $\vec{F}$  is found.

$$\vec{\nabla}^2 \vec{F} + \omega^2 \epsilon\mu\vec{F} = -\vec{J}_m \quad (24)$$

The introduction of vector and scalar potential functions for the field quantities simplifies the analysis of boundary value problems significantly. This is essential for the analytical calculation of propagating modes and simple radiating structures.

The wave equations in terms of fields and auxiliary functions can be simplified when considering guided wave structures such as transmission lines. Transmission lines are used as examples of typical board components in this work because they are prone to high coupling with antenna fields as a result of their open field structure. Therefore, the classical transmission line model for describing wave propagation is presented next.

### 2.2.1.2 Wave Equation for Transmission Lines

Transmission lines are guided wave structures, which are described with a 1D wave equation. Furthermore, since the fields are bound to the transmission line, voltages and currents are

introduced for the electric and magnetic fields, respectively. The voltages and currents on the transmission line are not only time and frequency dependent but also have a spatial dependency when the transmission line length is on the order of or larger than the wavelength. Therefore, it is necessary to describe transmission lines with distributed elements.

Figure 8 shows the equivalent circuit of an infinitesimally short transmission line of length  $dx$  and the distributed per-unit-length parameters [45]. The inductance  $L'$  and capacitance  $C'$  per-unit-length result from the current flow and charge storage on the transmission line.

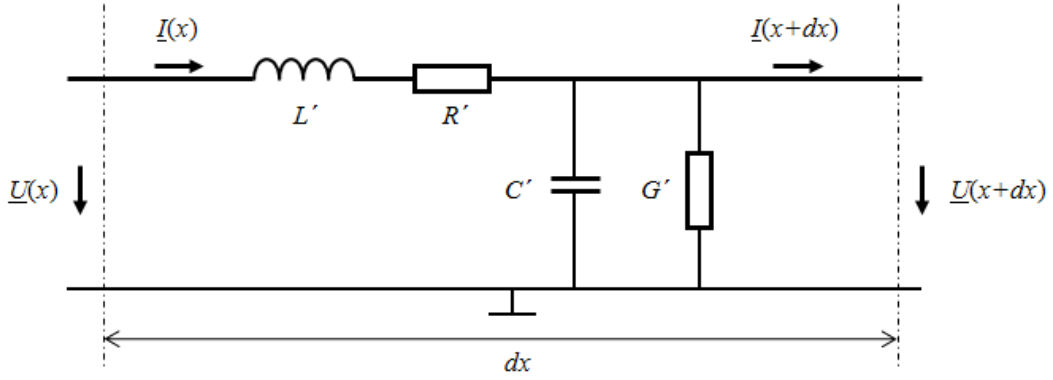


**Figure 8: Equivalent circuit model of an infinitesimal transmission line piece with the distributed per-unit-length parameters.**

The resistance  $R'$  and conductance  $G'$  per-unit-length account for the conductor and dielectric losses, respectively. The voltages,  $\underline{U}(x)$  and  $\underline{U}(x+dx)$ , as well as the currents,  $\underline{I}(x)$  and  $\underline{I}(x+dx)$ , characterize the terminals of the transmission line section. Based on the equivalent circuit,  $\underline{U}(x)$  and  $\underline{I}(x)$  are expressed in the form of differential equations with the limit that  $dx \rightarrow 0$  (telegrapher's equations).

$$\frac{\partial \underline{U}(x)}{\partial x} = -(R' + j\omega L') \underline{I}(x) \quad (25)$$

$$\frac{\partial \underline{I}(x)}{\partial x} = -(G' + j\omega C') \underline{U}(x) \quad (26)$$

Inserting (25) into (26) yields the wave equation for the voltage on the transmission line.

$$\frac{\partial^2 \underline{U}(x)}{\partial x^2} = \underline{\gamma}^2 \underline{U}(x) \quad (27)$$

The propagation constant  $\underline{\gamma}$  depends on the per-unit-length transmission line parameters.

$$\underline{\gamma} = \sqrt{(R' + j\omega L')(G' + j\omega C')} \quad (28)$$

The characteristic impedance  $\underline{Z}_0$  of the transmission line is given as follows:

$$\underline{Z}_0 = \sqrt{\frac{R' + j\omega L'}{G' + j\omega C'}} \quad (29)$$

In the case of a transmission line with low losses i.e.,  $\omega L' \gg R'$  and  $\omega C' \gg G'$ , the impedance becomes real and the propagation constant is imaginary with only the phase constant  $\beta$ .

$$\underline{Z}_0 = \sqrt{\frac{L'}{C'}} \quad (30)$$

$$\beta = \omega \sqrt{L'C'} \quad (31)$$

Based on these transmission line parameters, wave propagation on transmission lines is fully described. Finally, in order to round off this section, two fundamental theorems applicable to the results in this work are presented next.

### 2.2.1.3 Important Theorems applicable to Antennas and Transmission Lines

Reciprocity of antennas and transmission lines is an important characteristic. Consider two antennas or, more generally, two electromagnetically coupled structures termed 1 and 2. The Lorentz reciprocity theorem states that in a volume  $V$  surrounded by the surface  $\vec{A}$  the following relationship is valid for electric and magnetic fields and their current sources [93]:

$$\iiint_V (\vec{J}_1 \vec{E}_2 - \vec{J}_2 \vec{E}_1) dV = \oint\!\!\!\oint_A (\vec{E}_1 \times \vec{H}_2 - \vec{E}_2 \times \vec{H}_1) d\vec{A} \quad (32)$$

$\vec{J}_1$  and  $\vec{J}_2$  are the current sources, and  $\vec{E}_1$ ,  $\vec{E}_2$ ,  $\vec{H}_1$  and  $\vec{H}_2$  are the corresponding electric and magnetic fields of the sources, respectively. The volume integral can be evaluated as [93]:

$$\iiint_V (\vec{J}_1 \vec{E}_2 - \vec{J}_2 \vec{E}_1) dV = \oint_A \vec{J}_1 d\vec{A} \int_S \vec{E}_2 d\vec{s} - \oint_A \vec{J}_2 d\vec{A} \int_S \vec{E}_1 d\vec{s} \quad (33)$$

$$= I_1 U_2 - I_2 U_1 \quad (34)$$

$I_1$ ,  $I_2$ ,  $U_1$  and  $U_2$  are the currents and the voltages at the terminals of 1 and 2, respectively. The above relationship assumes that the medium inside the volume is linear and isotropic. For a very large volume  $V \rightarrow \infty$ , it can be further shown that [93]:

$$I_1 U_2 = I_2 U_1 \quad (35)$$

Thus, it can be concluded that two passive transmitting and receiving antennas behave like a reciprocal two port network. The same applies to the radiation pattern of an antenna, which is the same in transmitting mode and in receiving mode.

Another important theory is the duality theorem. It is possible to express the fields of one antenna as the fields of the complementary antenna by interchanging the field quantifies and material parameters [95]. Consider the magnetic current density  $\vec{J}_m$  introduced above. The first two of Maxwell's equations are then written as follows:

$$\vec{\nabla} \times \vec{H} = j\omega\epsilon\vec{E} \quad (36)$$

$$\vec{\nabla} \times \vec{E} = -j\mu\omega\vec{H} + \vec{J}_m \quad (37)$$

Maxwell's equations are now fully symmetric. The fields produced by the electric current source  $\vec{J}$  can be interchanged to yield those produced by the magnetic current source  $\vec{J}_m$ .

$$\vec{E} \rightarrow \vec{H}' \quad (38)$$

$$\vec{H} \rightarrow -\vec{E}' \quad (39)$$

$$\vec{J} \rightarrow \vec{J}_m' \quad (40)$$

$$\varepsilon \rightarrow \mu' \quad (41)$$

In the next subsection, an in-depth analysis of the complex power density produced by the antenna fields is given.

### 2.2.2 Complex Power Density of Excited Antenna

The antenna fields can be expressed in terms of power and energy. Consider the schematic representation of the patch antenna configuration with the microstrip feeding line in Figure 6. The Poynting theorem is the energy conservation law in electrodynamics [93]. It is expressed in the frequency domain in integral form as follows:

$$\oint_A \vec{S} d\vec{A} = -\frac{1}{2} \iiint_V \vec{E} \cdot \vec{J}^* dV + j2\omega \iiint_V (w_E - w_M) dV \quad (42)$$

$$\vec{S} = \frac{1}{2} \vec{E} \times \vec{H}^* \quad (43)$$

The power density  $\vec{S}$  (Poynting vector) exiting or entering the volume  $V$  through the surface element  $d\vec{A}$  is equal to the power delivered by the sources  $\vec{J}$  plus the rate of change (described by  $j\omega$  in the frequency domain) of the stored energy densities  $w_E$  and  $w_M$  inside  $V$ .

$$w_E = \frac{1}{4} \varepsilon |\vec{E}|^2 \quad (44)$$

$$w_M = \frac{1}{4} \mu |\vec{H}|^2 \quad (45)$$

If losses are present,  $\underline{\mu}$  and  $\underline{\varepsilon}$  can be expressed as complex quantities. In this case, the imaginary parts account for the electric and magnetic losses, respectively. However, to simplify the following discussion, a lossless environment is considered and the spatial power decay of evanescent near-fields as well as propagating space and surface waves are analyzed. An understanding of the spatial behavior of the propagating and reactive power density is essential for defining the electromagnetic antenna boundary.

### 2.2.2.1 Power Decay of Evanescent Near-fields and Propagating Space Waves

The complex spatial power decay is analyzed next using a basic radiating structure, which can be treated analytically. The Hertzian dipole comprises an infinitesimal current source  $\underline{I}_z$  pointing in  $z$  direction with the length  $dl$ . This is considered an ideal antenna for which a closed form analytical expression of its fields can be derived. The vector potential (14) reduces to [94]:

$$\underline{A}_z = \frac{1}{4\pi} \frac{\underline{I}_z dl}{r} \cdot e^{-j\beta r} \quad (46)$$

Equation (46) can be transformed into a spherical coordinate system.

$$\vec{\underline{A}} = \underline{A}_z \cos(\theta) \vec{e}_r - \underline{A}_z \sin(\theta) \vec{e}_\theta = \frac{1}{4\pi} \frac{\underline{I}_z dl}{r} (\cos(\theta) \vec{e}_r - \sin(\theta) \vec{e}_\theta) e^{-j\beta r} \quad (47)$$

The rotation operator (6) can also be expressed in spherical coordinates [93].

$$(\vec{\nabla} \times \vec{\underline{A}}) \vec{e}_r = \frac{1}{r \sin(\theta)} \left( \frac{\partial}{\partial \theta} (\underline{A}_\phi \sin(\theta)) - \frac{\partial \underline{A}_\theta}{\partial \phi} \right) \quad (48)$$

$$(\vec{\nabla} \times \vec{\underline{A}}) \vec{e}_\phi = \frac{1}{r} \left( \frac{\partial}{\partial r} (r \underline{A}_\theta) - \frac{\partial \underline{A}_r}{\partial \theta} \right) \quad (49)$$

$$(\vec{\nabla} \times \vec{\underline{A}}) \vec{e}_\theta = \frac{1}{r} \left( \frac{1}{\sin(\theta)} \frac{\partial \underline{A}_r}{\partial \phi} - \frac{\partial}{\partial r} (r \underline{A}_\phi) \right) \quad (50)$$

Applying (47) to (48)-(50) yields the magnetic field component of the current source after some minor calculation steps [96].

$$\underline{H}_\phi = \frac{\underline{I}_z dl}{4\pi} \beta^2 \left( j \frac{1}{\beta r} + \frac{1}{(\beta r)^2} \right) \sin(\theta) e^{-j\beta r} \quad (51)$$

Finally, the electric field components can be found by inserting (51) into (1) yielding:

$$\underline{E}_r = 2Z_0 \frac{I_z dl}{4\pi} \beta^2 \left( \frac{1}{(\beta r)^2} - j \frac{1}{(\beta r)^3} \right) \cos(\theta) e^{-j\beta r} \quad (52)$$

$$\underline{E}_\theta = Z_0 \frac{I_z dl}{4\pi} \beta^2 \left( j \frac{1}{\beta r} + \frac{1}{(\beta r)^2} - j \frac{1}{(\beta r)^3} \right) \sin(\theta) e^{-j\beta r} \quad (53)$$

$Z_0$  is the free space wave impedance. With these field components, the complex Poynting vector (43) is found.

$$\underline{\vec{S}} = -\frac{1}{2} \left( \underline{E}_r \underline{H}_\phi^* \underline{\vec{e}}_\theta - \underline{E}_\theta \underline{H}_\phi^* \underline{\vec{e}}_r \right) \quad (54)$$

$$\underline{\vec{S}} = Z_0 \frac{|I_z|^2 dl^2}{16\pi^2} \beta^4 \left( \underline{X}_r \underline{\vec{e}}_r + \underline{X}_\theta \underline{\vec{e}}_\theta \right) \sin(\theta) \quad (55)$$

$$\underline{X}_r = \left( \frac{1}{(\beta r)^2} - j \frac{1}{(\beta r)^3} \right) \sin(\theta) \quad (56)$$

$$\underline{X}_\theta = j \left( \frac{1}{(\beta r)^3} + \frac{1}{(\beta r)^5} \right) \cos(\theta) \quad (57)$$

It can be observed in (56) and (57) that the reactive power density  $\text{Im}\{\underline{\vec{S}}\}$  spatially decays with  $1/r^5$  (15 dB/octave) and  $1/r^3$  (9 dB/octave) and, thus, dominates for small values of  $r$ , hence, close to the antenna.

$$\left| \text{Im}\{\underline{\vec{S}}\} \right| \sim \frac{1}{r^n}, n=3,5 \quad (58)$$

On the other hand, the real power density  $\text{Re}\{\underline{\vec{S}}\}$  decays with  $1/r^2$  (6 dB/octave) in  $r$  direction (56). This term, pointing away from the source, describes the propagation of power away

from the antenna. The power density of the radiated space wave can be described as the distribution of power on a spherical surface  $4\pi r^2$  in the far-field of the antenna.

$$\left| \text{Re}\{\vec{S}\} \right| \sim \frac{1}{r^2} \quad (59)$$

The real power density dominates for large values of  $r$  further away from the antenna. Thus far, the influence of the dielectric substrate has not been considered. Therefore, an analysis of surface wave modes and their spatial decay behavior is given in the next subsection.

### 2.2.2.2 Power Decay of Propagating Surface Waves

A grounded dielectric substrate is capable of guiding surface waves. An in depth study of surface waves on grounded and ungrounded substrates was done by Collin [97] and Harrington [98]. In this section, a typical PCB substrate configuration used for (quasi) millimeter-wave applications is considered, and the influence of the substrate height and dielectric constant on the surface wave fields is analyzed. As a starting point, consider the grounded substrate configuration in Figure 9. The substrate has a height  $h$  and relative permittivity  $\epsilon_r$ .

The configuration is assumed to extend infinitely in  $y$  direction. Therefore, there is no spatial field dependency on  $y$ . The wave propagation is considered in  $x$  direction with the wave number  $k_x$  (propagation constant). At this stage, only the transverse magnetic (TM) modes are considered.

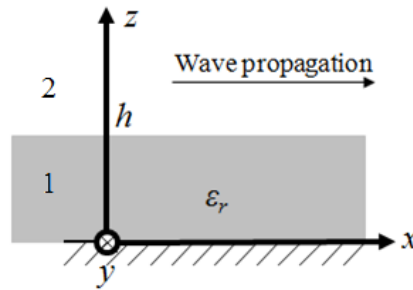


**Figure 9: Grounded substrate used for the calculation of surface wave fields.**

Solutions are constructed with the vector potential and the scalar solution function  $\underline{\psi}_{TM}$  assuming the following condition:



$$\vec{A} = \underline{\Psi}_{TM} \cdot \vec{e}_x \quad (60)$$

Note that the electric and magnetic fields are easily found using (6), (8) and (11). A set of solutions for region 1 ( $0 < z < h$ ) and region 2 ( $h < z < \infty$ ) is given in [98]:

$$\underline{\Psi}_{TM,1} = A \sin(uz) e^{-jk_x x} \quad (61)$$

$$\underline{\Psi}_{TM,2} = B e^{-vz} e^{-jk_x x} \quad (62)$$

$A$  and  $B$  are amplitude factors. The separation equations for the wave numbers in each region are readily found [98].

$$u^2 + k_x^2 = \frac{\omega^2}{c_0^2} \epsilon_r \quad (63)$$

$$-v^2 + k_x^2 = \frac{\omega^2}{c_0^2} \quad (64)$$

The notation of the wave numbers  $u$  and  $v$  is chosen such that both are real in the case of wave propagation. Next, the wave number  $k_x$  is eliminated by inserting (63) into (64).

$$u^2 + v^2 = \frac{\omega^2}{c_0^2} (\epsilon_r - 1) \quad (65)$$

Boundary conditions are evaluated next. The tangential electric and magnetic field components in the plane of the substrate/air interface at  $z=h$  must be equal. The following expression results [98]:

$$uh \tan(uh) = \epsilon_r vh \quad (66)$$

Next, the characteristic transcendental equations can be set up and brought into a convenient form for a graphical solution.

$$f(uh) = \frac{uh \tan(uh)}{\epsilon_r} = \left(r_0^2 - (uh)^2\right)^{1/2} \quad (67)$$

$$r_0^2 = \left(\frac{h\omega}{c_0}\right)^2 (\epsilon_r - 1) \quad (68)$$

The equation of circles with radius  $r_0$  is observed on the RHS of (67). On the LHS, there are tangent functions. A direct analytical solution of the transcendental equation does not exist. However, it can be solved graphically. The solutions are the intersection points of the two functions. The graphical solution technique for transcendental equations has an advantage over numerical solution techniques because it allows for physical insight into the behavior of the parameters. Figure 10 shows solutions to (67) corresponding to the intersection points of the tangent and circle functions. The parameter  $h$  is normalized to the wavelength  $\lambda$  for generality of the results.

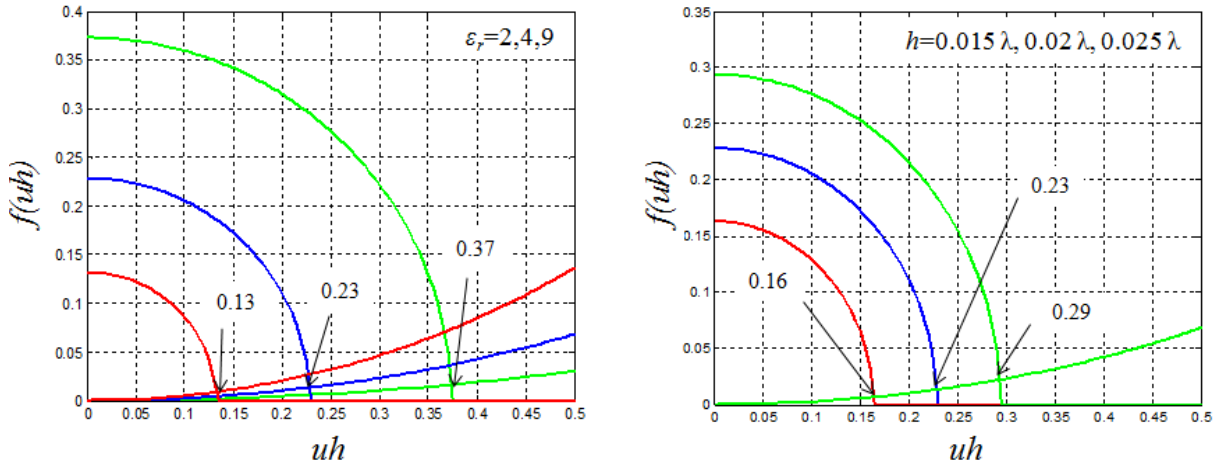


**Figure 10: Solutions of the transcendental equations for different values of  $\epsilon_r$  and  $h$ .**

Solutions are plotted for three  $\epsilon_r$  and three  $h$  values of the substrate. It is observed that for the chosen values of  $\epsilon_r$  and  $h$  (relative to  $\lambda$ ) there only exists one solution in the first quadrant. Therefore, only the lowest order  $TM_0$  mode exists on these substrate configurations for the analyzed wavelength. Once the graphs are plotted, the intersections points can be determined,

and the values of  $u$  are calculated. The values of  $v$  are determined by inserting  $u$  into the separation equations. Once both values are found for a parameter set ( $\epsilon_r$  and  $h$ ), the problem is solved, and the fields can be evaluated. The field variation in the direction normal to the substrate i.e., the variation with respect to  $z$ , is of interest.

Figure 11 and Figure 12 show the plots of the longitudinal and transverse electric field components for three variations of  $\epsilon_r$  and three variations of  $h$  with  $\lambda=16.67$  mm ( $f=18$  GHz).

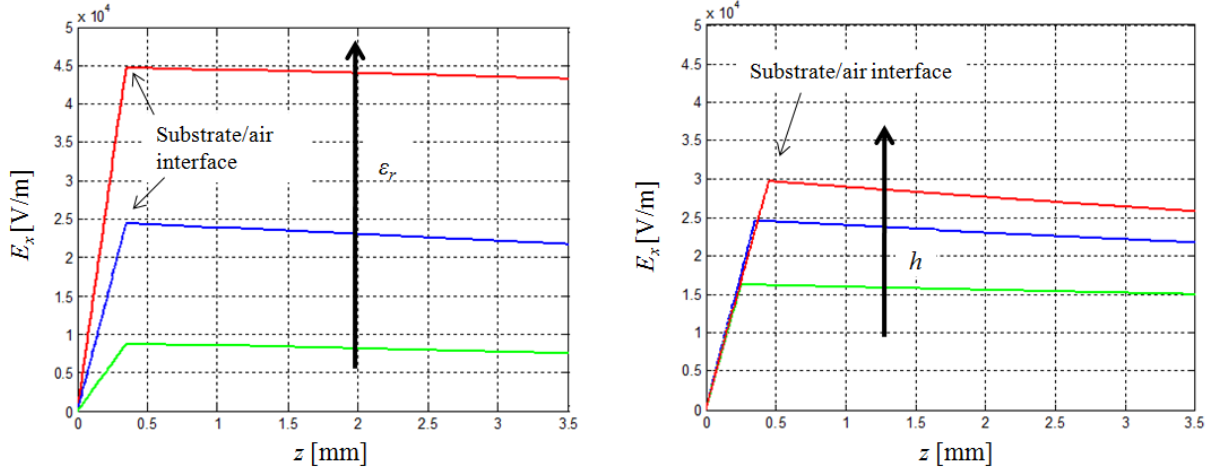


Figure 11: Longitudinal electric field of  $TM_0$  surface wave with  $\lambda=16.67$  mm ( $f=18$  GHz).

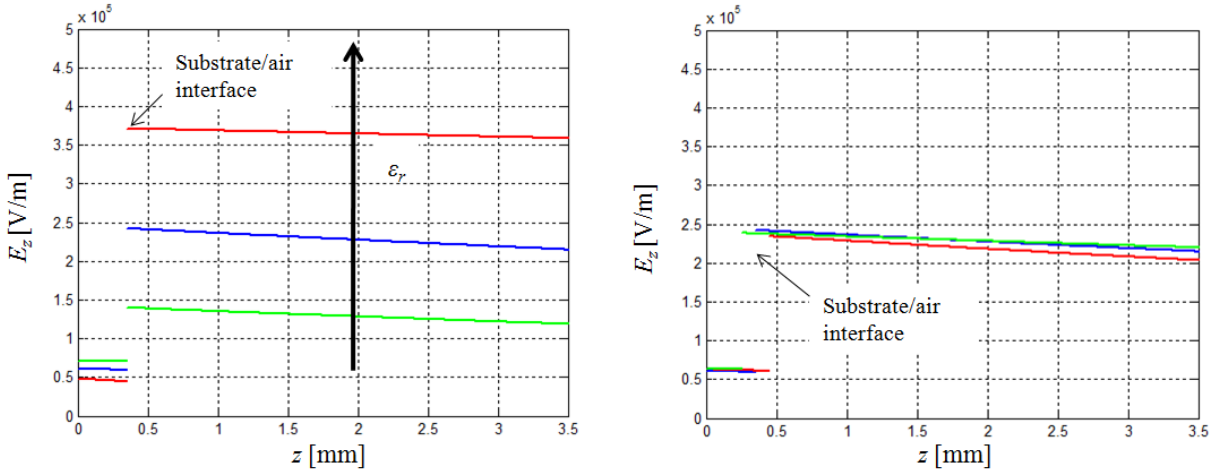


Figure 12: Transverse electric field of  $TM_0$  surface wave with  $\lambda=16.67$  mm ( $f=18$  GHz).

It is observed that the magnitude of the longitudinal component  $E_x$  is about 10 times smaller than the transverse component  $E_z$ . The influence of the dielectric constant of the substrate is more significant on the magnitude of the electric field than the height of the substrate. The

field strength at the substrate/air interface increases with increasing substrate height and increasing dielectric constant. It is also observed that  $E_z$  is insensitive to the substrate height.

The radial propagation of the surface waves away from the region of excitation has not been considered so far. The surface wave was assumed to propagate in  $x$  direction. To estimate the spatial decay rate, cylindrical coordinates are introduced. These offer the advantage of a realistic radial spatial dependency of the propagating surface wave power density.

The TM and TE surface wave modes propagate in radial direction. It is assumed that the surface wave is excited at the origin of the coordinate system. For propagation in  $r$  direction, the vector potentials (6) and (23) in cylindrical coordinates assume the following simple forms:

$$\vec{A} = \underline{\Psi}_{TM} \cdot \vec{e}_r \quad (69)$$

$$\vec{F} = \underline{\Psi}_{TE} \cdot \vec{e}_r \quad (70)$$

Note that  $r = (x^2 + y^2)^{0.5}$  is the radius in cylindrical coordinates (also referred to as  $\rho$ ). The radial variation of the  $n^{\text{th}}$  mode of the potentials is described with a Hankel function of second kind [98].

$$\underline{\Psi}_{TM/TE} \sim H_n^{(2)}(k_r r) \quad (71)$$

A set of solutions for region 1 ( $0 < z < h$ ) and region 2 ( $h < z < \infty$ ) can be found [98]:

$$\underline{\Psi}_{TM,1} = A_{TM} \sin(uz) \cos(n\varphi) H_n^{(2)}(k_r r) \quad (72)$$

$$\underline{\Psi}_{TE,1} = A_{TE} \cos(uz) \cos(n\varphi) H_n^{(2)}(k_r r) \quad (73)$$

$$\underline{\Psi}_{TM,2} = B_{TM} e^{-vz} \cos(n\varphi) H_n^{(2)}(k_r r) \quad (74)$$

$$\underline{\Psi}_{TE,2} = B_{TE} e^{-vz} \cos(n\varphi) H_n^{(2)}(k_r r) \quad (75)$$

The separation equations for the two regions are given by the following:

$$u^2 + k_r^2 = \frac{\omega^2}{c_0^2} \varepsilon_r \quad (76)$$

$$-v^2 + k_r^2 = \frac{\omega^2}{c_0^2} \quad (77)$$

After some calculations, the equation for determining the cut-off frequencies of the modes is obtained [98].

$$f_c = n \frac{c_0}{4h(\varepsilon_r - 1)} \quad (78)$$

Only odd TM modes with even orders  $n=0, 2, 4, \dots$  and even TE modes with odd orders  $n=1, 3, 5, \dots$  exist on a grounded substrate. The lowest order  $n=0$  TM surface wave mode propagates down to DC. The cut-off frequency for the first higher order surface wave mode, the  $TE_1$  mode, considering a typical PCB substrate configuration with  $h=250 \mu\text{m}$  and  $\varepsilon_r=4$ , is 272 GHz. Therefore, for the frequencies and PCB technology considered in this work, only propagation of the fundamental  $TM_0$  mode needs to be considered. Finally, from (72)-(75), the power density distribution of the  $TM_0$  surface wave mode is obtained.

$$\left| \text{Re} \left\{ \bar{\underline{S}} \right\} \right| \sim \left| H_0^{(2)}(k_r r) \right|_{r \rightarrow \infty}^2 \sim \frac{1}{r} \quad (79)$$

The power density decay is proportional to  $1/r$  (3 dB/octave). The power is guided by the dielectric material along the substrate and distributed on a cylindrical surface. The spatial decay rate of surface waves is, thus, slower than the spatial decay rate of space waves (59).

### 2.2.2.3 Comments on Power Coupling to Board Components

Based on the previous results, Figure 13 shows an overview of the possible coupling mechanisms that are evoked by planar antennas. The planar antenna radiates a surface wave on the substrate in addition to the primary desired space wave. These far-field modes were

differentiated by their characteristic spatial decay behavior (59) and (79). However, close to the antenna, reactive power stands in the near-field and decays rapidly with increasing distance (58). Coupling mechanisms are also evoked in the near-field.

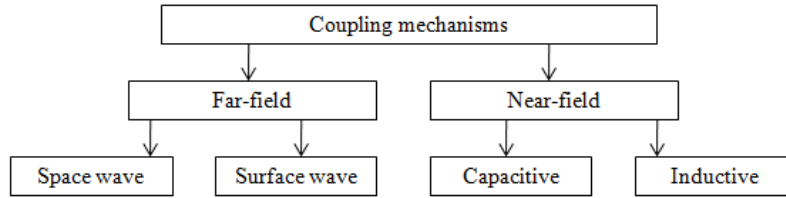


**Figure 13: Overview of coupling mechanisms between planar antennas and board components.**

To illustrate this, Figure 14 shows the current and charge distributions,  $\vec{J}$  and  $q$ , on the patch antenna. The charge distribution on the patch antenna has a maximum at the edge of the radiating apertures of the patch. At the center of the patch, the charge distribution exhibits a node. Therefore, capacitive coupling is highest at the radiating apertures. On the other hand, the current distribution has a maximum at the center of the patch. Therefore, inductive coupling is at its maximum at the center of the patch. These capacitive and inductive coupling mechanisms are illustrated with the capacitance  $C_{12}$  and the mutual inductance  $M_{12}$ .

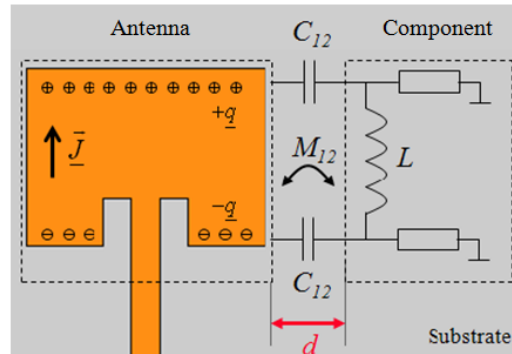


**Figure 14: Illustration of distributed nature of capacitive and inductive coupling from a resonant patch antenna.**

These electromagnetic interactions at the antenna near-fields directly affect the charge and current distribution on the antenna, inevitably also altering the antenna parameters. This is one of the main reasons to define the electromagnetic antenna boundary at which the reactive power density of the near-fields has decayed far enough so that the weak coupling assumption can be made.

### 2.2.3 Modeling and Simulation of Antenna Fields

The electromagnetic fields excited by antennas have been analyzed from a theoretical point of view in the previous section. A specific example of an ideal planar antenna is studied in this section in order to quantify the spatial decay of the propagating and reactive power density as well as the influence of the substrate and antenna feed on the excited fields. In literature, models for describing and approximating the fields and parameters of planar antennas and linking these to the physical dimensions of the antenna have been proposed. These are necessary for first order designs, which are used to create 3D models containing the geometrical and material parameters of the antenna and to compute the antenna with a numerical full-wave electromagnetic field solver. The most commonly employed planar antenna is the patch antenna. Therefore, it is used as an example in this section.

#### 2.2.3.1 Analytical Planar Antenna Models

Figure 15 shows the geometry of a typical patch antenna on a grounded substrate, which is used in the analysis throughout this section. The patch resonator comprises a rectangular patch of width  $w$  and length  $l$ . The height of the substrate is  $h$ , and it has a relative dielectric constant  $\epsilon_r$ . The feeding point is located at a distance  $s$  in negative  $x$  direction from the center of the patch resonator. The coordinate system is located at the center of the patch resonator on the ground plane.

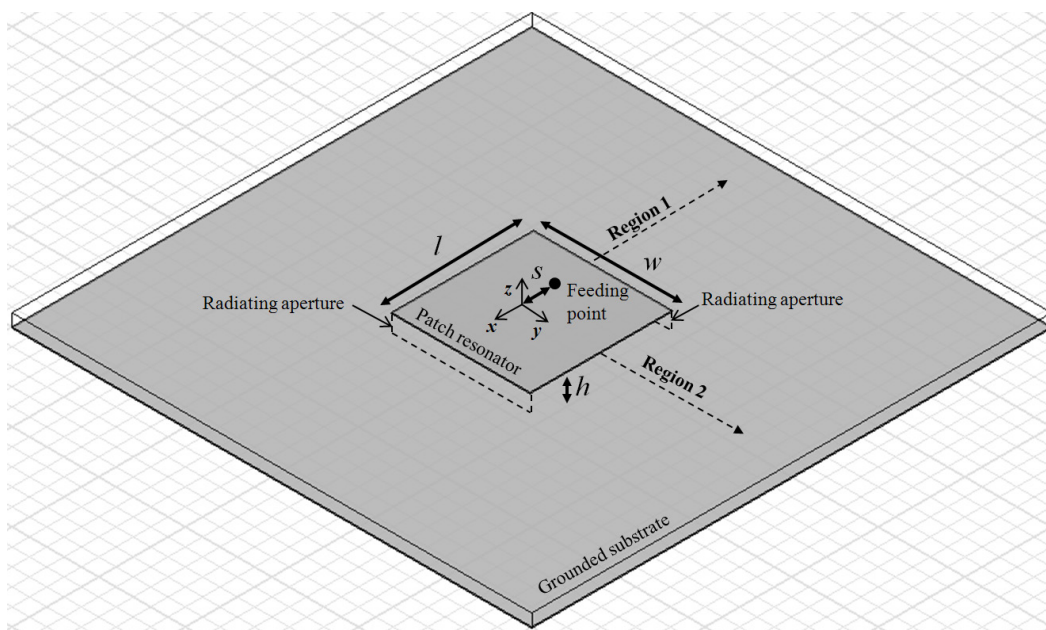


Figure 15: Model of patch antenna on a grounded dielectric substrate.

Three common methods for the design and analysis of patch antennas have been studied and applied in literature [94, 99]: (1) the cavity model; (2) the transmission line model; and (3) the full-wave simulation model.

With the cavity model, the field distribution of the excited patch antenna is approximated analytically by finding the field distribution between patch and ground plane with simplified boundary conditions. For this purpose, the patch is modeled as a parallel plate waveguide with magnetic walls. The resonance frequencies of the cavity are determined for all cavity resonance modes ( $m$ ,  $n$  and  $p$  are the mode orders and  $c_0$  is the speed of light).

$$\frac{\omega^2}{c_0^2} \epsilon_r = \left( \frac{m\pi}{l} \right)^2 + \left( \frac{n\pi}{w} \right)^2 + \left( \frac{p\pi}{h} \right)^2 \quad (80)$$

Based on the cavity model, the electric and magnetic field distributions underneath the patch antenna can be approximated for the fundamental  $TM_{100}$  resonance mode. The electric field of this mode is  $z$  directed and sinusoidal along the non radiating apertures and constant along the radiating apertures.

$$\underline{E}_z = jE_0 \sin\left(\frac{\pi}{l}x\right) \quad (81)$$

At the antenna resonance frequency, a standing wave is excited on the patch i.e., the magnetic field underneath the patch antenna is  $90^\circ$  out of phase with the electric field.  $E_0$  and  $H_0$  are the field amplitudes at the resonance frequency.

$$\underline{H}_y = H_0 \cos\left(\frac{\pi}{l}x\right) \quad (82)$$

The transmission line model, on the other hand, treats the patch antenna like a microstrip transmission line. Consider again the lowest order  $TM_{100}$  mode on the patch antenna. Figure 16 shows a circuit model of the patch antenna. The radiating apertures of the antenna are modeled with a parallel RC circuit ( $R_1$ ,  $R_2$ ,  $C_1$  and  $C_2$ ) to capture the effects of the stray fields and radiation. The patch itself is modeled with a wide and low impedance microstrip transmission line with characteristic impedance  $Z_0$  and phase constant  $\beta$ . The antenna feeding



point, where the source voltage  $\underline{U}_{in}$  with source impedance  $Z_{in}$  is connected, is located at a distance  $s$  from the center of the patch, as also illustrated in Figure 15.

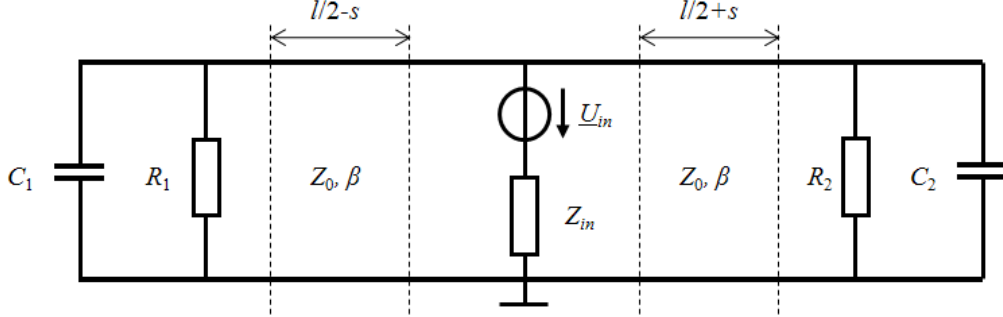


**Figure 16: Parameterized transmission line model of a conventional rectangular patch antenna for excitation with the  $TM_{100}$  mode.**

Analytical approximations for the design of patch antennas are available in open literature [100]. These approximations are useful for determining the physical patch antenna parameters prior to simulations. The patch width  $w$  is typically chosen first. The practical patch width should be chosen in order to ensure that no additional resonance mode is excited across the patch width. Next, the effective relative dielectric constant  $\epsilon_{reff}$  for this patch width is calculated in the static case [94]:

$$\epsilon_{reff} = \frac{\epsilon_r + 1}{2} + \frac{\epsilon_r - 1}{2\sqrt{1 + 12\frac{h}{w}}} \quad (83)$$

To consider the effects of the fringing fields of the patch antenna at the radiating apertures, the effective patch length extension  $\Delta l$  is used.

$$\Delta l = 0.412h \frac{(\epsilon_{reff} + 0.3)\left(\frac{w}{h} + 0.264\right)}{(\epsilon_{reff} - 0.258)\left(\frac{w}{h} + 0.8\right)} \quad (84)$$

Finally, the required patch length  $l$  for obtaining resonance at the frequency  $f_R$  is determined using the following expression.

$$l = \frac{c_0}{2f_R} \frac{1}{\sqrt{\epsilon_{reff}}} - 2\Delta l \quad (85)$$

A good impedance match for the excitation of the  $TM_{100}$  mode is obtained by placing the feeding point  $s$  between the center and the edge of the patch, roughly according to the following approximation for the input resistance  $R_{in}$  at resonance [94]:

$$R_{in} \approx R_{edge} \sin^2 \left( \frac{\pi}{l + 2\Delta l} x \right) \quad (86)$$

$R_{edge}$  is the effective resistance of both radiating apertures as seen at the feeding point. The input reactance is ideally zero at the resonance frequency of the patch.

Although the cavity and transmission line models provide physical insight into the operation of patch antennas and are useful for first qualitative approximations, the parasitic effects cannot be captured accurately. Therefore, numerical full-wave simulations need to be performed to obtain a realistic and accurate distribution of the complex power density as well as of its spatial decay behavior as its transitions from the near- to the far-field. Appendix 1 gives an overview of the numerical full-wave solution techniques and the solver used in this work.

### 2.2.3.2 Simulation of Antenna Field under Idealized Conditions

The analytical approximations allow a first estimation of the antenna dimensions. Numerical full-wave simulations are required to compute the fields excited by the antenna on the substrate in the vicinity of the antenna. The dimensions of the patch in the preceding example were approximated first with (83)-(85) and fine tuned for operation with the  $TM_{100}$  and a resonance frequency  $f=c_0/\lambda_0$ . Since all materials are linear, this model is frequency scalable and all the physical dimensions are normalized to the wavelength  $\lambda_0$ . The substrate height was set to  $h=0.02 \lambda_0$  with a relative dielectric constant  $\epsilon_r=3.75$ . First, a practical width for the patch was chosen  $w=0.25 \lambda_0$ . Next,  $\epsilon_{reff}=3.34$  was determined with (83). Finally, the patch length  $l=0.24 \lambda_0$  was calculated using (84) and (85). Based on these values, a simulation model was constructed. The antenna is excited with an idealized horizontal current at the center of the patch i.e., an  $x$  directed current across the entire patch width in order to remove

the influence of the antenna feed (at first) on the excited fields. Figure 17 shows a plot of the current density of the  $TM_{100}$  mode.

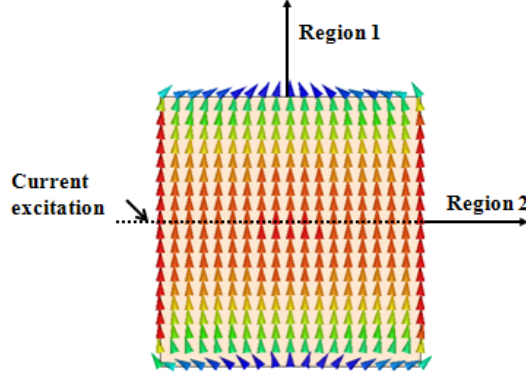


**Figure 17: Distribution of current density on the patch resonator with the "idealized" current excitation.**

Two regions in the direction of the arrows were defined for studying the magnitude and spatial decay of the electric and magnetic fields (see Figure 15). The regions are oriented in the two principle planes of the patch antenna on the ground plane: region 1 in the E-plane ( $x < 0, y = 0, z = 0$ ); and region 2 in the H-plane ( $x = 0, y > 0, z = 0$ ). Since the antenna is symmetrical in both principle planes, it is sufficient to define these regions from the center of the patch because the spatial field decays on the other side are identical.

The simulated electric and magnetic field distributions, which were computed directly by the field solver in the volume, are evaluated in the vicinity of the patch antenna on the ground plane. The complex power density is calculated with the tangential magnetic field components,  $\underline{H}_x$  and  $\underline{H}_y$ , and the normal electric field  $\underline{E}_z$ , according to (43).

$$\vec{S} = -\frac{1}{2} \left( \underline{E}_z \underline{H}_y^* \vec{e}_x - \underline{E}_z \underline{H}_x^* \vec{e}_y \right) \quad (87)$$

Of course, the complex power density can also be computed on top of the substrate. Since the substrate height is electrically short, however, the variation with respect to the  $z$  coordinate of the fields within the substrate can be assumed constant.

Figure 18 shows the logarithmic plot of the simulated propagating power density excited by the patch antenna on the ground plane. The power in the lateral plane is primarily launched in region 1 in the form of a surface wave mode. It is observed that the power decays slowly with increasing distance in region 1. The propagating power density in region 2, on the other hand,

decays faster with increasing distance. The current anti node on the patch resonator is also indicated with an arrow. The antenna is excited with a current source on the patch.

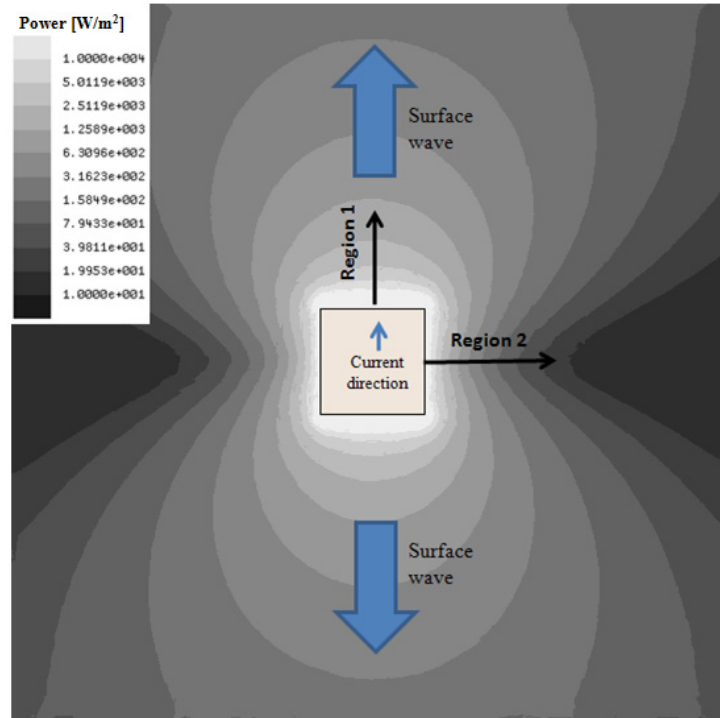


Figure 18: Simulation of the propagating power density excited by the patch antenna on the ground plane.

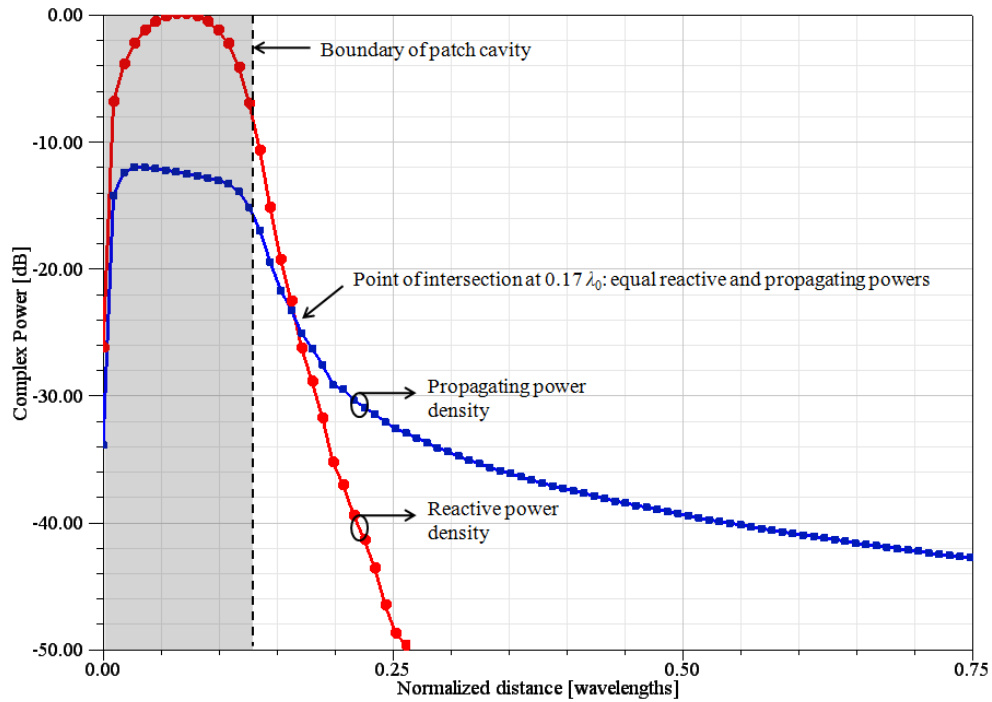


Figure 19: Simulation of the spatial complex power density excited by the patch antenna on the ground plane in region 1.

The complex power density in region 1, where the surface wave power of the patch antenna is primarily radiated, is studied in more depth. Figure 19 shows the simulated complex power density in region 1 in dependency of distance from the center of the patch resonator.

The magnitudes of the real and imaginary parts, describing the propagating power and reactive power density, are plotted in decibels. The curves are normalized to the maximum reactive power density underneath the patch resonator.

The reactive power density dominates underneath the patch resonator with a 12 dB higher magnitude. However, it is observed that the reactive power density decays faster than the propagating power density with increasing distance from the physical boundary of the patch cavity. The point of intersection, where the reactive power equals the propagating power, is located at a distance of approximately  $0.17 \lambda_0$  from the center of the patch. Beyond this distance, the reactive power density quickly decays below -50 dB.

Next, the influence of the antenna feed and the substrate height  $h$  on the excited fields of the antenna is quantified. A probe feed was introduced into the simulation model comprising a signal via connected to the patch. Figure 20 shows an illustration of the probe feed configuration. The probe feed is a common technique to excite a patch antenna. The signal via is isolated from the ground plane and fed from underneath the ground plane through a coaxial connection. The probe feed offset  $s=0.09 \lambda_0$  was determined by simulations based on the relationship in (86). The probe feed causes the resonance frequency of the antenna to drop by 1.5 % as a result of the additional feed inductance.

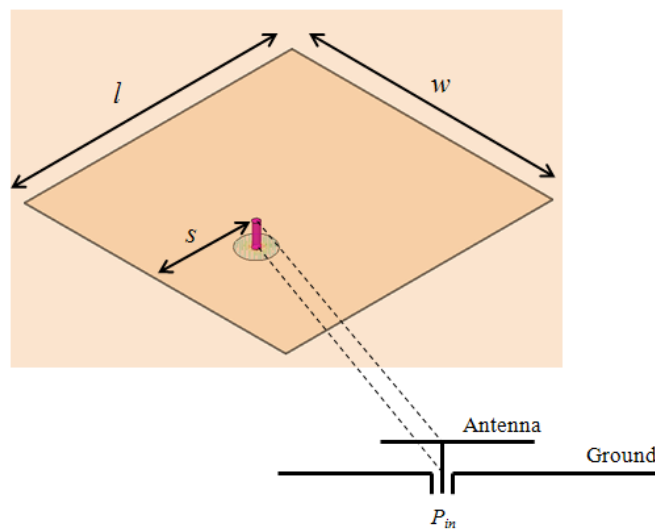
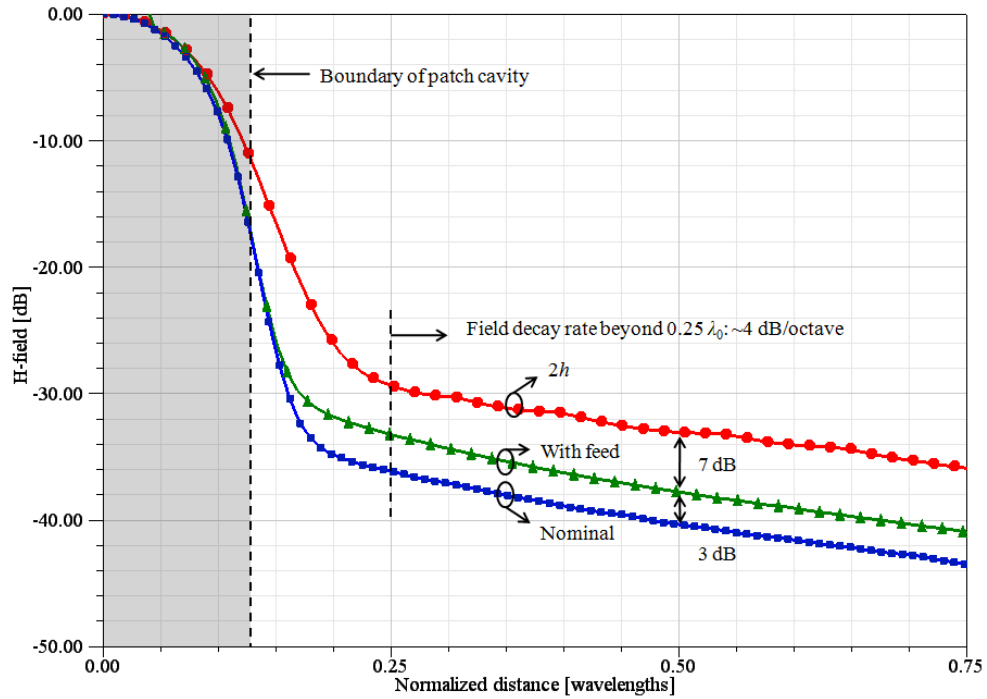
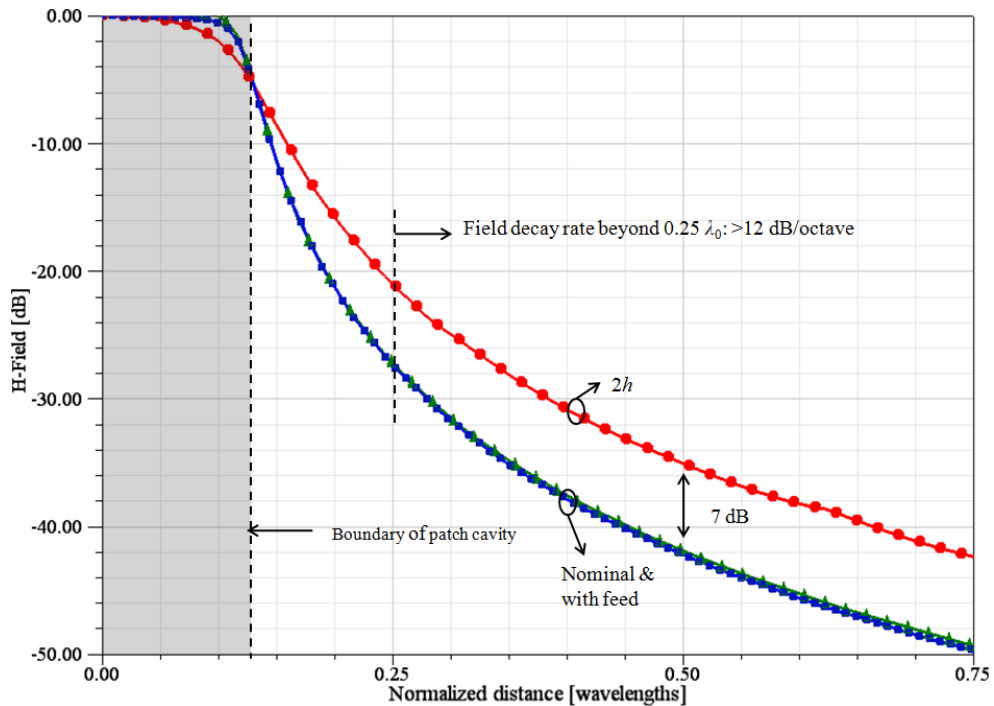


Figure 20: Configuration of the coaxial probe feed and the inset distance  $s$  from the patch edge.

Figure 21 and Figure 22 show the simulated magnetic fields on the ground plane with increasing distance from the antenna in regions 1 and 2 where only the  $y$  component of the magnetic field exists.



**Figure 21: Simulation of the normalized magnetic field excited by the patch antenna on the ground plane in region 1.**



**Figure 22: Simulation of the normalized magnetic field excited by the patch antenna on the ground plane in region 2.**

The results of the nominal configuration (with ideal current feed and substrate height  $h$ ) are compared to the results of the antenna with probe feed and with a thicker substrate i.e., double of the height  $2h$ , respectively. The physical boundary of the patch resonator is also indicated in the figures.

It is observed that the magnitudes of the magnetic fields increase by 3 dB and 10 dB for the cases with the probe feed and increased substrate height, respectively. Thus, more power is launched into the substrate. The spatial decay rates of the fields are approximately 4 dB/octave beyond a distance of roughly  $0.25 \lambda_0$  from the patch center for the three cases in region 1. This indicates not only the presence of the surface wave mode but also the settling of the reactive near-fields. Considering the magnetic field in region 2, on the other hand, only the configuration with increased substrate height causes higher field strengths to occur. Furthermore, since the spatial decay of the fields is greater than 12 dB/octave, propagating surface and space wave modes are not dominant in this region.

The results in this subsection are based on numerical simulations. The accuracy of numerical simulations needs to be verified. Therefore, a quantification of the solver accuracy as well as measurement results are presented in Appendix 2.

In summary, it is concluded that the antenna feed and substrate configuration have a significant effect on the excited fields of planar antennas. It was also shown that the reactive power density decays fast with increasing distance from the antenna while the propagating power density decays slower yielding high field strengths in the substrate and on the ground plane.

#### 2.2.4 Determining the Electromagnetic Antenna Boundary

So far in this chapter, the excited antenna fields were characterized from a theoretical point of view. It was shown that planar antennas give rise to propagating surface and space waves. Figure 23 shows an illustration of these far-field modes at board level.

The power of the space wave mode is distributed on a spherical surface ( $\sim 1/r^2$ ), and the power of the surface wave mode is distributed on a cylindrical surface ( $\sim 1/r$ ) and depends primarily on the substrate parameters  $h$  and  $\epsilon_r$ . Furthermore, reactive power density stands in the near-field of planar antennas, which decays with at least  $\sim 1/r^3$  with increasing distance from the antenna. Table 1 shows a summary of the different near- and far-field spatial decay rates that were examined.

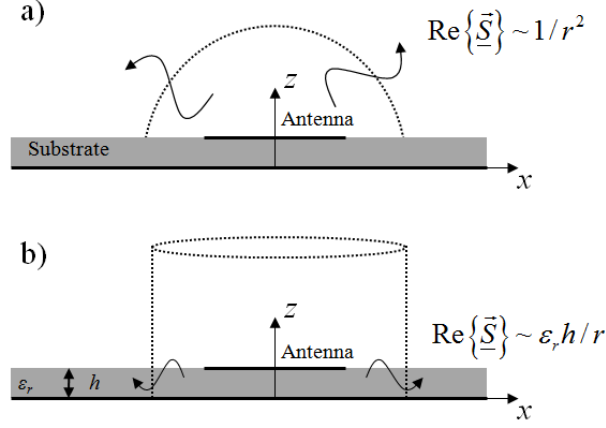


**Figure 23: Illustration of far-field waves radiated by a planar antenna configuration including: (a) the space wave mode; and (b) the surface wave mode.**

Type		Spatial field decay	
Far-field propagation	Surface wave	$1/r$	3 dB/octave
	Space wave	$1/r^2$	6 dB/octave
Reactive near-fields	Evanescent	$1/r^n, n>3$	>9 dB/octave

**Table 1: Summary of the spatial field decay rates near excited planar antennas.**

In literature, the space around an excited antenna has been divided into three general regions [94]: (1) the reactive near-field; (2) the radiating near-field and; (3) the far-field region. These regions are defined through the maximum physical dimension  $d$  of the antenna in relationship to the operating wavelength  $\lambda$ . The boundaries  $r_1$  and  $r_2$  of the three general field regions are in the range  $0 < r_1 < r_2 < \infty$ .

$$r_1 = 0.62 \sqrt{d^3 / \lambda} \quad (88)$$

$$r_2 = 2d^2 / \lambda \quad (89)$$

The radiating near-field, as defined above, only exists if  $d$  is large compared to  $\lambda$ . For small antennas with similar properties to short dipoles, the boundary between reactive near-field and far-field is defined by  $r_0$  as:

$$r_0 = 1 / \beta = \lambda / 2\pi \quad (90)$$



Unfortunately, the ideal infinitesimal dipole is practically the only antenna type, where this region can be given precisely. For this ideal structure, the averaged radial components of the reactive and propagating power densities (55) at the radian distance are equal. Furthermore, these field regions are very general and do not include the actual geometrical and material properties of planar antennas. Besides, defining a radius does not seem to be appropriate for planar antennas. In compact wireless modules, determining a realistic boundary for the reactive near-fields is necessary for efficient component placement and electromagnetic antenna size estimation.

Therefore, the proposed electromagnetic antenna boundary in this work is not based on specifying a distance directly, but is determined by evaluating the reactive power density  $|\text{Im}\{\vec{S}\}|$  of the excited planar antenna and deducing a threshold value  $|\text{Im}\{\vec{S}\}|_{\max}$ . The block out region is then defined as the set of all points in the plane for which the reactive power density is above the threshold value. Accordingly, the electromagnetic antenna boundary is defined as follows:

$$|\text{Im}\{\vec{S}\}| \begin{cases} > |\text{Im}\{\vec{S}\}|_{\max}, \text{ inside EM antenna boundary} \\ < |\text{Im}\{\vec{S}\}|_{\max}, \text{ outside EM antenna boundary} \end{cases} \quad (91)$$

A 2D block out region is desired in the context of planar antennas. Therefore, the considerations will be restricted to the ground plane (or substrate) of the antenna. Since the substrate is electrically thin, the values of the fields do not change in the direction of the  $z$  axis within the substrate i.e., they are practically the same on the top and bottom plane of the substrate.

Different approaches for defining the threshold value were considered. Since the reactive power density has a faster spatial decay rate in comparison to the propagating power density, a maximum ratio could be defined as  $|\text{Im}\{\vec{S}\}|/|\text{Re}\{\vec{S}\}|$ , or a maximum tolerable limit of  $|\text{Im}\{\vec{S}\}|$  could be given directly. However, these limits do not consider the antenna parameters including the operating frequency, antenna efficiency, input reflection coefficient and input power, which all take direct influence on the reactive near-field distribution and, hence, the reactive power density. Consequently, one possibility to define the threshold value is relating it to the power exiting the antenna structure  $P_{out2}$  (refer to Figure 6).

$$\left| \text{Im} \{ \bar{\underline{S}} \} \right|_{\max} = \frac{\pi P_{out2}}{\lambda^2} \quad (92)$$

This definition is motivated by the infinitesimal dipole, where the averaged radial components of the reactive and propagating power densities (55) at the radian distance are equal and assume this value.

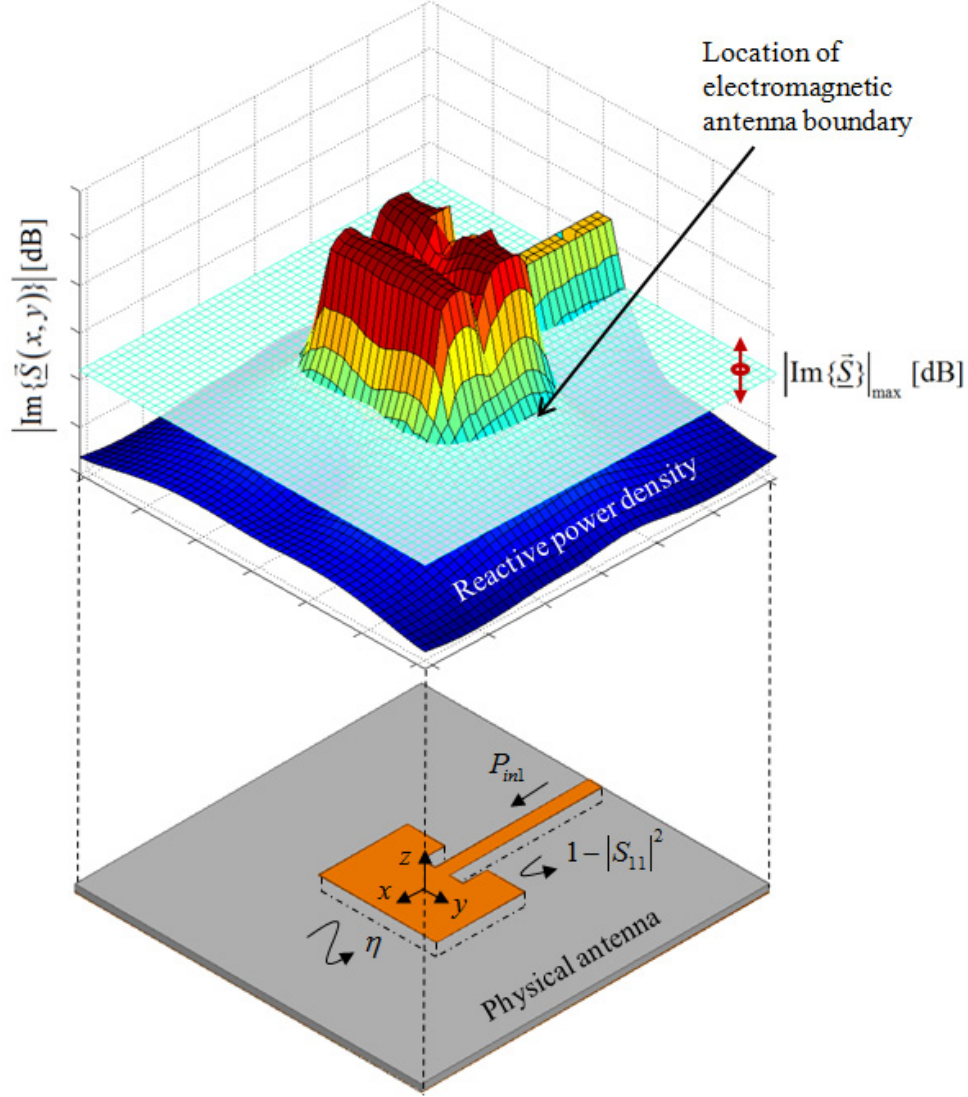


**Figure 24: Graphical illustration of the reactive power density, the threshold value for determining the electromagnetic antenna boundary as well as the antenna parameters.**

This threshold value can then also be expressed in terms of the input power of the antenna  $P_{in1}$ , the antenna efficiency  $\eta$  (including dielectric and conductor losses of the antenna) and the input reflection coefficient  $S_{11}$ .

$$\left| \text{Im} \left\{ \bar{S}(P_{in1}, \eta, S_{11}) \right\} \right|_{\max} = \frac{\pi P_{in1}}{\lambda^2} (1 - |S_{11}|^2) \eta \quad (93)$$

The actual power delivered to the antenna is contained in the term  $1 - |S_{11}|^2$  considering impedance mismatch with the feeding line. The power contained in the near-fields including the power loss (conductor and dielectric losses) is given by  $\eta$ . Therefore, the expression is also valid for different antenna efficiencies.

Figure 24 shows a graphical illustration of the reactive power density and the electromagnetic antenna boundary defined in the 2D plane. The feasibility of defining the electromagnetic antenna boundary is shown in the next section by considering three planar antenna configurations. It is shown that additional space near the antenna needs to be considered as being part of the antenna and that board components should not be placed there. This ensures that the antenna parameters are preserved when the antenna is integrated.

### 2.3 Comparison of Planar Antennas and Application of Antenna Boundary

In this section, different planar antenna configurations are studied and compared with regards to their excited field distributions, and their electromagnetic antenna boundaries are deduced. Three planar antennas comprising a patch antenna, slot antenna and dipole antenna are considered. These antennas are differentiated by their geometry and radiation characteristics. The patch antenna primarily radiates perpendicular to the ground plane in one direction. The slot antenna also primarily radiates perpendicular away from the ground plane, but in both directions above and below. The dipole antenna primarily radiates in lateral direction i.e., in the plane of the substrate. Another differentiation between the antenna configurations is the antenna feed. The patch and slot antennas are single ended configurations i.e., they are fed through a single microstrip line referenced to the ground plane. The dipole antenna, on the other hand, is fed through a differential line comprising two microstrip lines operated with  $180^\circ$  phase shift between them. As a result, the dipole is not driven against the ground plane. All three antennas were designed to operate at 24 GHz on the same substrate configuration. Appendix 1 gives an overview of the numerical full-wave solution techniques and the solver that was used to design and optimize of the antennas. A typical high frequency PCB substrate with two copper metallization layers was used. The substrate has a relative dielectric constant  $\epsilon_r=3.75$ , dielectric loss tangent  $\tan(\delta)=0.006$ , height  $h=250 \mu\text{m}$  and copper metallization thickness  $t=17.5\mu\text{m}$ . The copper metallization has a conductivity of 58 MS/m. In Appendix 4,

an overview of the manufacturing process, used for the fabrication of all planar configurations, is given. The antennas, fed through impedance controlled microstrip lines (see Appendix 3), are optimized for impedance matching with less than -10 dB reflection coefficient and high radiation efficiency within the bandwidth of operation. The antennas were driven with 1 mW (0 dBm) source power in the simulations.

### 2.3.1 Patch Antenna

The patch antenna depicted in Figure 25 comprises a metallic patch above the ground plane. The patch is excited with its fundamental  $\lambda/2$  resonance mode (lowest order TM mode). The patch length  $l_p$  and width  $w_p$ , which primarily determine the resonance frequency and impedance of the patch resonator, respectively, were optimized for resonance at 24 GHz on the substrate configuration. The dimensions  $l_p=3.175$  mm and  $w_p=4.25$  mm were determined after the optimization.

The concept of this antenna is similar to the ideal patch antenna already analyzed in Section 2.2.3.2 apart from the feeding technique. The inset feed is used so that the microstrip line can be placed on the same layer as the patch. The length  $s$  of the inset and the width  $g$  of the gaps were optimized to ensure impedance matching to the 50  $\Omega$  microstrip line at 24 GHz.

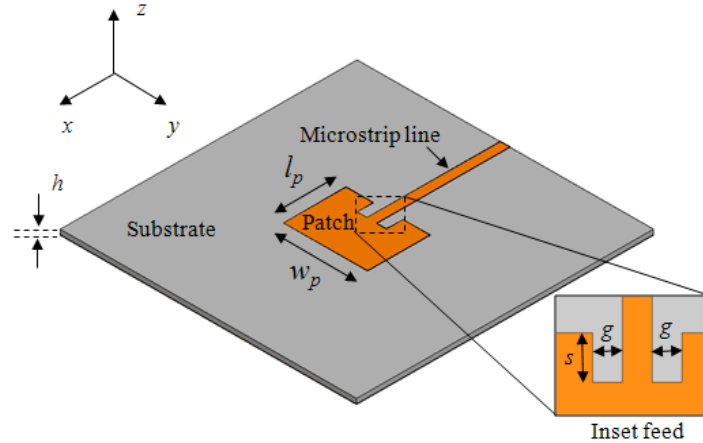


**Figure 25: Simulation model and dimensions of the 24 GHz inset fed patch antenna.**

In order to characterize the input reflection coefficient and impedance bandwidth, a test structure of the antenna was manufactured and measured. Figure 26 shows the measured reflection coefficient  $S_{11}$  and a comparison with the full-wave simulation results.

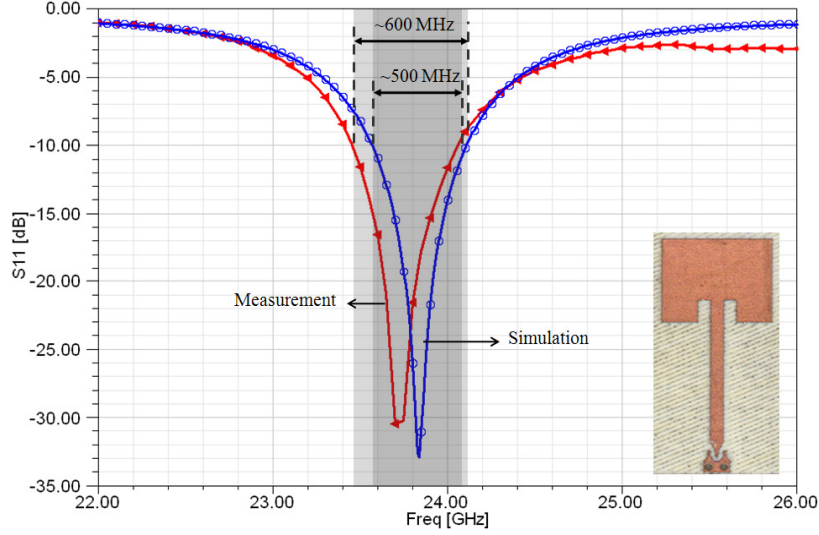


**Figure 26: Measurement of the reflection coefficient  $S_{11}$  of the patch antenna and comparison to full-wave simulation. The top view of the manufactured antenna with the feeding line and contact pads is also shown.**

The impedance bandwidth of the antenna is evaluated at the -10 dB points around the resonance frequency. A slight discrepancy of the resonance frequency between the simulation and measurement results is observed. The slightly higher measured bandwidth of 600 MHz, compared to 500 MHz in simulation, is primarily caused by technological tolerances as well as by additional losses such as the surface roughness of the copper. It must also be considered that the influence of the GSG (ground, signal, ground) probe adapter was not included in the simulation model.

### 2.3.2 Slot Antenna

The slot antenna configuration in Figure 27 comprises a  $\lambda/2$  slot resonator. The antenna is fed through a  $50\ \Omega$  microstrip line at the edge of the slot. A shorting via is used to connect the end of the microstrip line to the ground plane. This allows good impedance matching to  $50\ \Omega$ . The position of the shorting via can be adjusted to match the slot antenna to a variety of feeding line impedances. A slot length  $l_s=4.5\text{ mm}$  and width  $w_s=150\ \mu\text{m}$  were determined after optimization to ensure resonance near 24 GHz.

Note that the slot resonator radiates above and below the ground plane. Its radiation pattern and field distribution are similar to those of a magnetic  $\lambda/2$  dipole antenna, where the equivalent magnetic current density is assumed to flow in the slot. The radiation patterns are analyzed further on in Section 2.3.4.

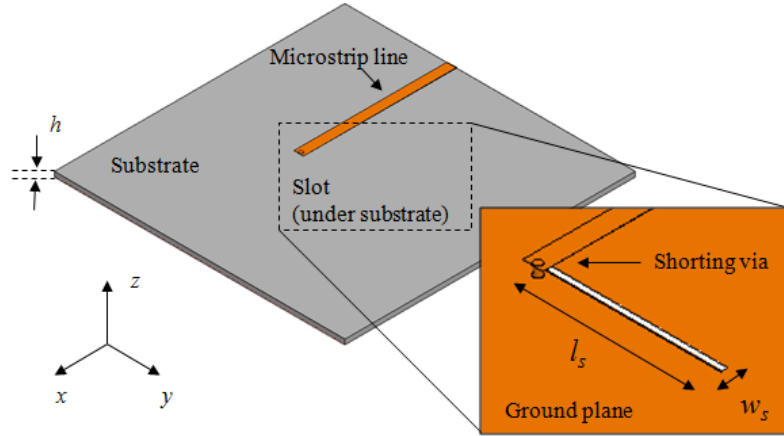


Figure 27: Simulation model and dimensions of the 24 GHz edge fed slot antenna.

The measurement of the slot antenna poses challenges with respect to the placement on a metallic wafer chuck. Therefore, the slot antenna was placed on a 3 cm thick Styrofoam™ block at the edge of the chuck before it was probed. This is necessary to reduce the influence of the parasitic proximity effects introduced by the metallic wafer chuck. The ground plane of the slot antenna is not continuous, and the radiation below the ground plane causes image currents to be excited and reflections to occur inevitably altering the antenna parameters. Styrofoam™ is chosen for its low dielectric constant and loss tangent ensuring negligible capacitive loading of the antenna. Figure 28 shows the measurement and simulation results of the slot antenna.

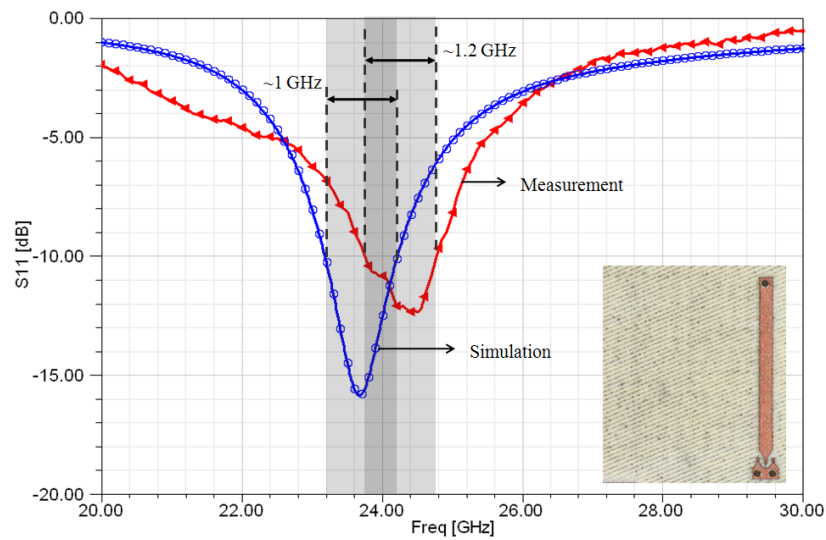
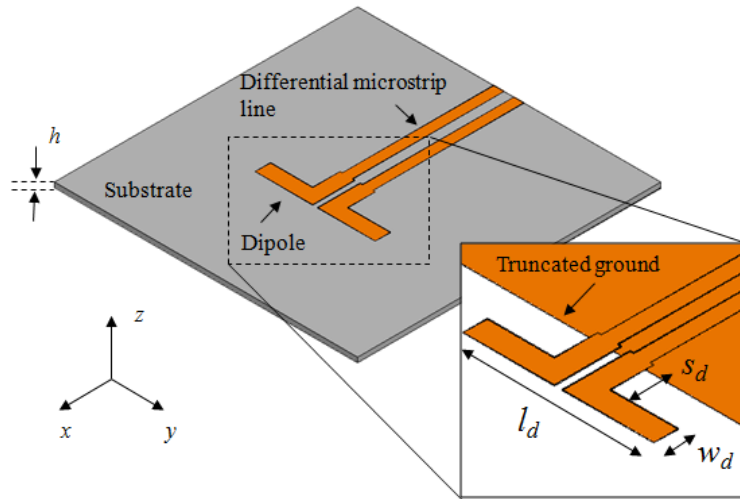


Figure 28: Measurement of the reflection coefficient  $S_{11}$  of the slot antenna and comparison to full-wave simulation. The top view of the manufactured antenna with the feeding line and contact pads is also shown.

Similarly to the results of the patch antenna, it is observed that the measured bandwidth of 1.2 GHz is slightly higher than the simulated bandwidth of 1 GHz. This higher value is attributed to additional losses such as the surface roughness of the copper metallization. The GSG probe adapter was also not included in the simulation model.

### 2.3.3 Dipole Antenna

The dipole antenna in Figure 29 is fed through a differential microstrip line with an impedance of  $100\ \Omega$ . The differential line comprises two  $50\ \Omega$  microstrip lines connected to the two printed dipole arms.



**Figure 29: Simulation model and dimensions of the 24 GHz center fed dipole antenna.**

The ground plane underneath the dipole is truncated to eliminate image currents, which would inevitably cancel the antenna mode. The dipole is designed to operate in approximately  $3/4\ \lambda$  mode and is located at a distance  $s_d=1.35\ \text{mm}$  from the edge of the ground plane. This is necessary to ensure that the ground plane acts as a reflector. The dipole length  $l_d=5.95\ \text{mm}$  and the dipole width  $w_d=0.75\ \text{mm}$  were fine tuned with full-wave simulations.

The reflection coefficient of the dipole antenna was measured by implementing a two port S-parameter measurement. By converting the single ended S-parameters to differential S-parameters, the differential response of the antenna was obtained. Figure 30 shows the results. Note that the dipole antenna was also measured on a 3 cm thick Styrofoam™ block to minimize the influence of the chuck. The experimental characterization is in satisfactory agreement with the simulation results.

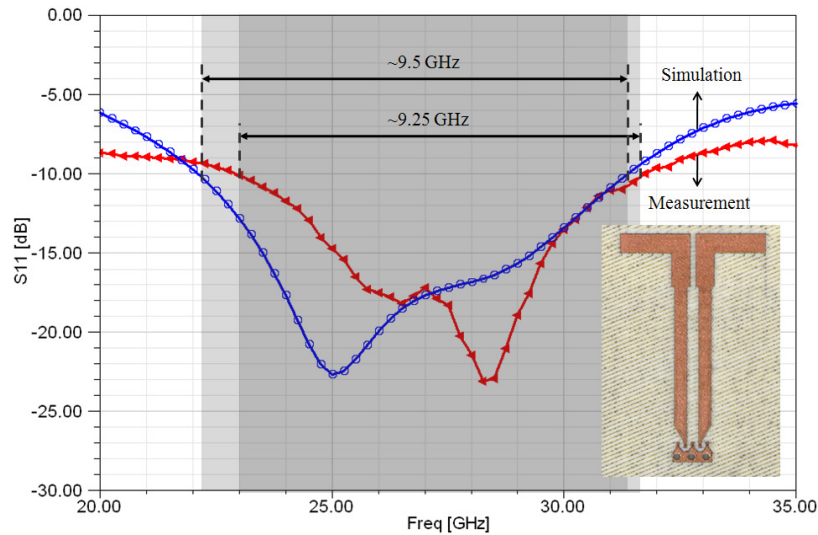


**Figure 30: Measurement of the reflection coefficient  $S_{11}$  of the dipole antenna and comparison to full-wave simulation. The top view of the manufactured antenna with the feeding line and contact pads is also shown.**

### 2.3.4 Comparison of Antenna Characteristics

In comparison to other board components, planar antennas excite particularly strong electric and magnetic fields in the lateral plane of the substrate. Figure 31 and Figure 32 show the simulated magnitudes of the electric and magnetic fields of the patch, slot and dipole antennas on the ground plane, respectively. The slight ripples, observed in both figures, are a result of reflections at the substrate and ground plane edges, reflections at the antenna feeding point, due to impedance mismatch, and minor stray reflections at the PML boundary conditions (see Appendix 1). All these effects cause standing waves to occur. The sizes of the substrate areas are 25 mm X 25 mm.

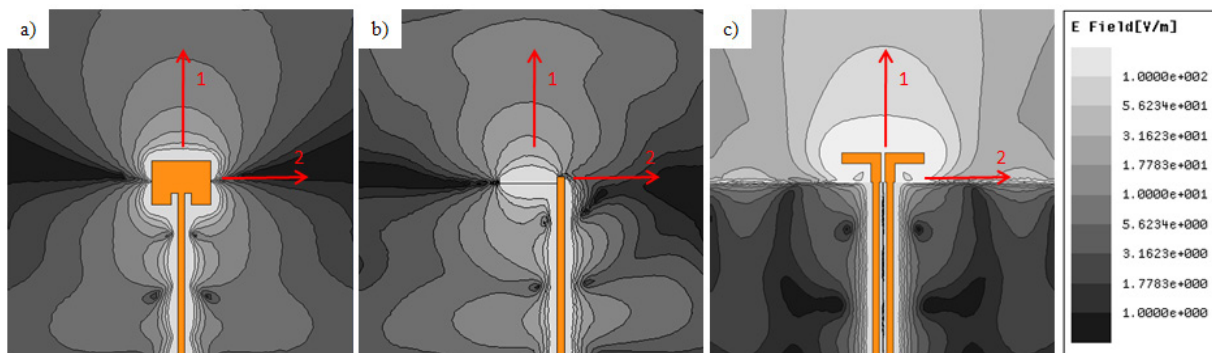


**Figure 31: Comparison of the simulated electric field distributions on the ground planes in the vicinity of the: (a) patch antenna; (b) slot antenna; and (c) dipole antenna.**



Since a standing wave is excited on the antenna structures at resonance, a voltage maximum exists at the radiating apertures of the patch antenna, in the center of the slot antenna and at the ends of the dipole antenna. These are the regions of high electric field strength. The electric field is orientated normal on the ground plane comprising primarily the  $z$  component. On the other hand, there are current maxima in the center of the patch antenna, at the ends of the slot antenna and in the center of the dipole antenna. In this region, the magnetic field of the standing wave is at its maximum. The magnetic field is orientated tangential to the ground plane comprising only the  $x$  and  $y$  components.

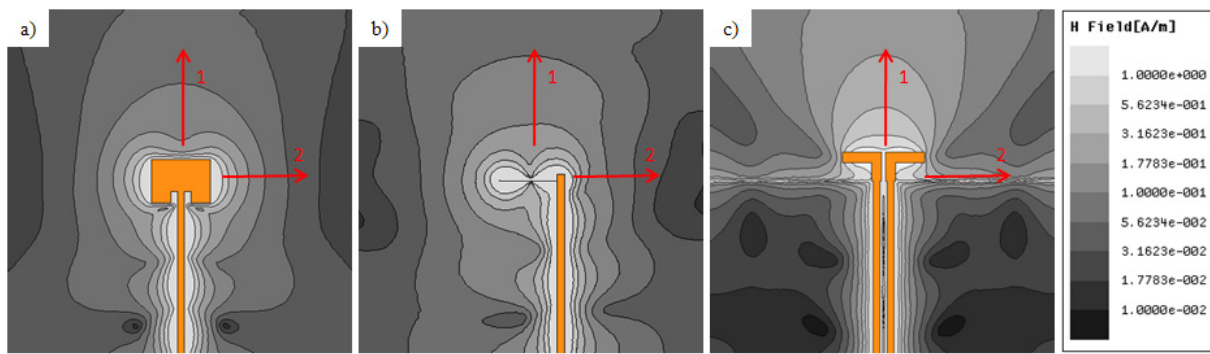


**Figure 32: Comparison of the simulated magnetic field distributions on the ground planes in the vicinity of the: (a) patch antenna; (b) slot antenna; and (c) dipole antenna.**

The field distributions of the patch and slot antennas are qualitatively similar. On the other hand, the electric and magnetic fields, excited by the dipole on the ground plane near the differential feeding line, are significantly lower compared to the patch and slot antenna. The reason for this is that the antenna is balanced and not driven against the ground plane. Therefore, the amount of coupling to be expected to components referenced to the same ground plane as the unbalanced patch or slot antenna is significantly higher than in the case of the balanced dipole antenna. However, in the case of the dipole antenna the ground plane is truncated below the dipole itself. Therefore, valuable board space on the substrate around the dipole cannot be used for components that need a ground reference.

The radiation patterns of the three antennas are also compared. Figure 33 shows a comparison of the computed radiation patterns of the gain in the two principle elevation planes i.e., the  $xz$  and  $yz$  planes.

The radiation of the patch antenna is directed primarily in positive  $z$  direction i.e., in the direction normal to the substrate and ground plane, with a maximum gain of 6.5 dBi. The slot antenna radiates in both positive and negative  $z$  directions with a maximum gain of 4.5 dBi.

On the other hand, the dipole radiates in lateral  $x$  direction with a maximum gain 5 dBi. All three antennas are linear polarized.

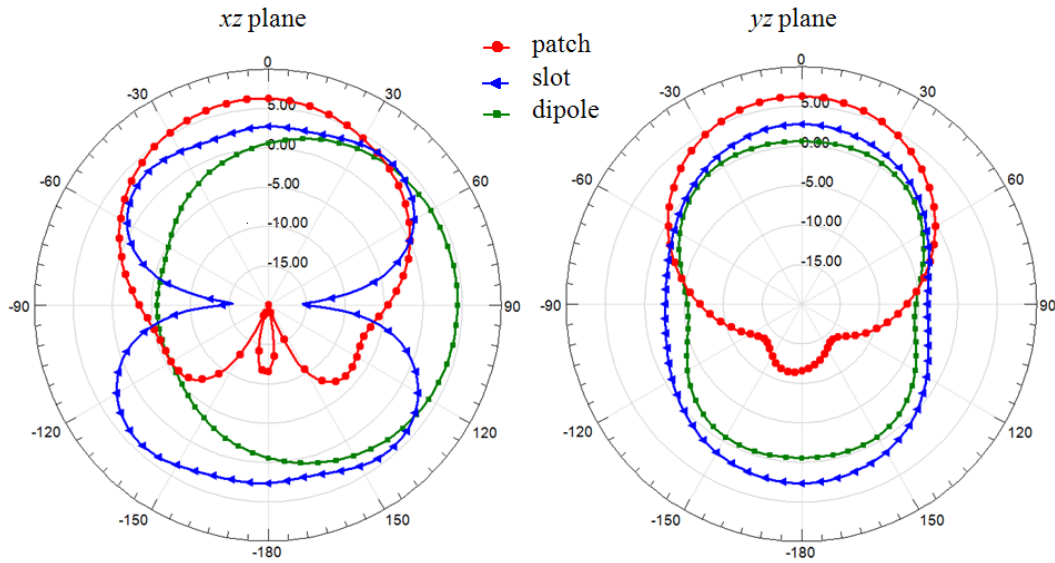


**Figure 33: Comparison of the simulated radiation patterns (gain) of the patch, slot and dipole antenna in two principle elevation planes.**

Table 2 shows a summary and comparison of the simulated antenna parameters. These include the impedance bandwidth, radiation efficiency  $\eta$  and gain as well as the physical dimensions at 24 GHz.

Type	Antenna Parameters		
	-10 dB BW [GHz]	$\eta$ [%] / Gain [dBi]	Phys. dimensions [mm <sup>2</sup> ]
Patch	0.5	80 / 6.5	3.175x4.25
Slot	1	90 / 4.5	4.5x0.15
Dipole	9.5	94 / 5	5.95x0.75 (2.1)

**Table 2: Comparison of the simulated parameters of the planar antennas at 24 GHz.**

The simulated radiation efficiencies of the antennas (including dielectric and conductor losses) show that the patch antenna has the lowest efficiency of 80 %. The slot antenna achieves an efficiency of 90 % and the dipole antenna has the highest efficiency of 94 %. The dipole antenna also displays the highest bandwidth of 9.5 GHz, attributed not only to its larger physical dimensions compared to the other antennas, but also to its spatial separation from the ground plane. Typical wireless modules employ large ground planes to ensure low impedance references for the transmission lines, active components and power distribution network. Since the dipole needs to be separated from the ground plane, which acts as a reflector,

valuable board space is potentially inefficiently utilized. Also, since single ended transmission lines are often used, an additional balun is required to feed the dipole. These are the main disadvantages of the planar dipole antenna because both factors, truncated ground plane and additional balun, require additional board space.

In conclusion, the characterized antennas exhibit satisfactory radiation performance for 24 GHz communication applications.

### 2.3.5 Deduction of Electromagnetic Antenna Boundary

The electromagnetic antenna boundary, as introduced in Section 2.2.4, is defined for the three planar antenna configurations. For this purpose, (93) is evaluated. All antennas are fed with  $P_{in1}=1$  mW (0 dBm) input power. The antenna efficiencies  $\eta$  are taken from Table 2. Since all the antennas exhibit small reflection coefficients,  $<-10$  dB at 24 GHz,  $S_{11}$  is neglected. Table 3 shows the calculated reactive power density threshold values for the antenna boundaries.

Type	$ \text{Im}\{\bar{S}\} _{\max} [\mu\text{W}/\text{mm}^2]$
Patch antenna	16
Slot antenna	18
Dipole antenna	19

Table 3: Comparison of the calculated threshold values.

The patch antenna exhibits the lowest threshold because it has the lowest efficiency. The dipole antenna, on the other hand, exhibits the highest efficiency and also has the highest threshold value.

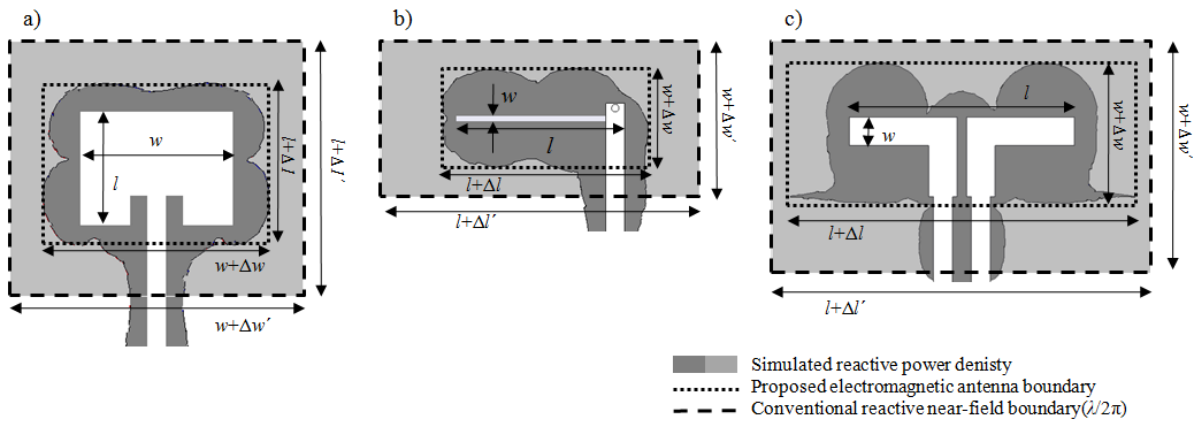


Figure 34: Simulated reactive power density on the ground plane of the planar antennas.

The electric and magnetic fields of the three planar antennas have been simulated (Figure 31 and Figure 32 show the results). With these fields, the Poynting vector was computed according to (43), and the magnitude of the imaginary part was determined and evaluated on the ground planes of the planar antennas. In Figure 34, the isolines of the reactive power density, as given in Table 3, are shown.

Two rectangles are constructed around the structures of each antenna. The geometrical parameters  $\Delta l$ ,  $\Delta l'$  and  $\Delta w$ ,  $\Delta w'$  are introduced to describe the electrical size increase compared to the physical antenna lengths  $l$  and antenna widths  $w$ , respectively. Please note that the block out area so defined is not rectangular. For practical design guidelines, it is advantageous to work with the circumscribed rectangle. The inner rectangles define the proposed electromagnetic antenna boundary. The outer rectangles define the conventional textbook reactive near-field boundary (90) located at the distance  $\lambda/2\pi$  from the antenna surfaces/edges. This corresponds to a minimum distance of approximately 2 mm on each side of the antenna. Notice that the conventional reactive near-field boundary is considerably larger than the proposed electromagnetic antenna boundary. The electrical size of the antenna is “overestimated” using the standard textbook approach. This potentially leads to inefficient usage of available board space during antenna integration.

Table 4 shows a summary of the deduced antenna boundaries of the three planar antenna types. From here on,  $l+\Delta l$  is referred to as the electrical antenna length. Likewise,  $w+\Delta w$  is referred to as the electrical antenna width.

Antenna	Dimensions					
	Physical size			Electrical size		
	$l$ [mm]	$w$ [mm]	Area [mm <sup>2</sup> ]	$l+\Delta l$ [mm]	$w+\Delta w$ [mm]	Area [mm <sup>2</sup> ]
Patch	3.175	4.25	13.5	4.6	6.5	29.9
Slot	4.5	0.15	0.7	5.5	2.7	14.9
Dipole	5.95	0.75 (2.1)	12.4	9	3.75	33.8

**Table 4: Deduced dimensions of the electromagnetic antenna boundary of the antennas.**

Figure 35 shows a graphical representation of the physical antenna dimensions in comparison to the electrical antenna dimensions as defined by the electromagnetic antenna boundaries.

The patch antenna has the smallest physical and electrical length. Note that the length is the resonance determining dimension because it supports the standing wave. The physical and electrical length of the dipole is largest. Unlike the patch and slot antenna, which are operated in  $\lambda/2$  resonance mode, the dipole is operated in  $3\lambda/4$  resonance mode. On the other hand, the patch antenna has the largest physical and electrical width. The fields of the resonance mode

of the patch antenna are almost completely confined in the substrate. Primarily, the widths of the antennas determine the bandwidth and impedance properties. The slot has the smallest physical width. Since the currents flow along the perimeter of the slot, the electrical width is increased significantly in comparison to its physical width.

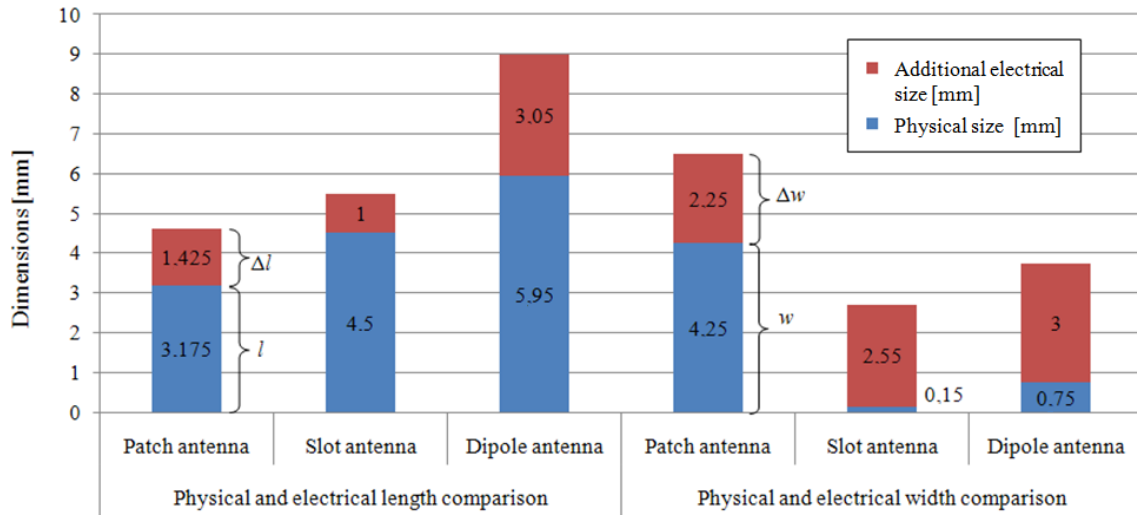
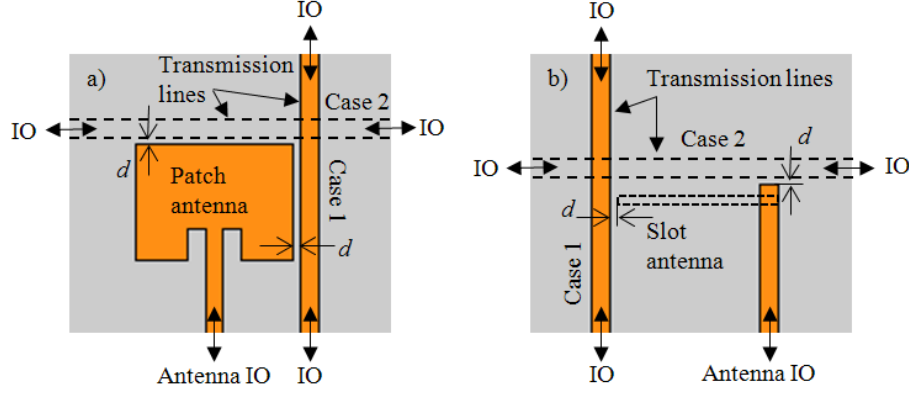


Figure 35: Comparison between the physical and additional electrical sizes of the planar antennas.

In order to illustrate the feasibility of using the electromagnetic antenna boundary for the integration of planar antennas, it is necessary to quantify the effects of components, such as transmission lines placed inside this boundary, on the antenna parameters.

### 2.3.5.1 Influence of Transmission Lines Routed within the Antenna Boundary

The magnitude of the electromagnetic interactions, occurring when board components are placed inside the electromagnetic antenna boundary, depends on the size, orientation, distance and material properties of the component. A typical board component is a planar transmission line, which, similar to the antenna, has an open field structure. It is desirable to route transmission lines close to planar antennas in order to efficiently exploit available board space. The assumption of weak coupling is valid when the secondary fields excited on the victim have negligible effects on the characteristics and fields of the aggressor. In this section, it is shown that transmission lines routed outside the electromagnetic antenna boundary only have a negligible effect on the antenna parameters.



**Figure 36: Illustration of the planar antennas with microstrip transmission lines routed inside electromagnetic antenna boundary of the (a) patch and (b) slot antennas.**

Figure 36 shows an illustration of the patch and slot antennas with additional microstrip lines. The microstrip lines are routed past the antennas with a separation distance  $d$  as illustrated. Complete full-wave simulations were conducted so that the electromagnetic interactions between the planar antennas and transmission lines are captured. The inputs and outputs of the transmission lines are marked with IO. At these ends, the transmission lines are matched terminated such that only minimal reflections  $< -10$  dB occur. The power coupled to the transmission line mode is, thus, directed away from the antenna. Notice that the dipole antenna is not considered in this study because the dipole antenna is not directly placed on the ground plane. Hence, grounded microstrip lines cannot be routed inside its electromagnetic antenna boundary.

The microstrip lines are designed for a characteristic impedance of  $50 \Omega$  (see Appendix 3). This corresponds to a width of  $500 \mu\text{m}$  based on the substrate configuration. The transmission lines are routed orthogonal and parallel to the antennas, denoted as case 1 and case 2, respectively. Figure 37 shows the simulation results of the relative change of the resonance frequency  $\Delta f$  of the antennas in dependency of the separation distance  $d$ . The corresponding electrical sizes, as specified by the electromagnetic antenna boundaries, are also depicted for both antennas. It is observed that the resonance frequencies settle below  $0.1\%$  from their nominal values with increasing values of  $d$  (the nominal values refer to the case where no additional transmission lines are on the substrate). Close to the antennas, when the transmission line is routed inside the electromagnetic antenna boundaries, the resonance frequencies are detuned by over  $1\%$  for the patch antenna and over  $0.6\%$  for the slot antenna.

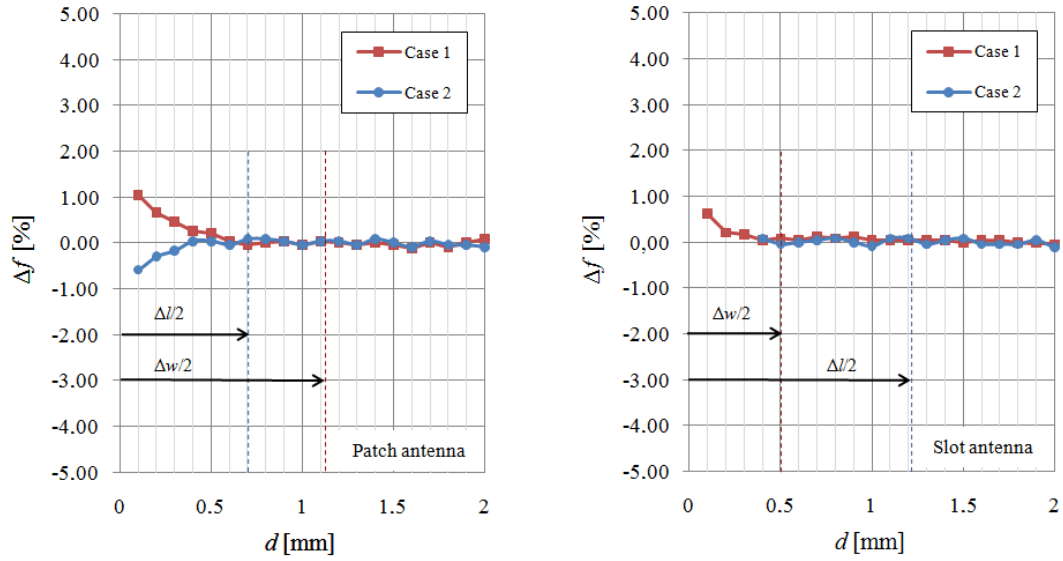


**Figure 37: Effects on the resonance frequencies of the antennas for different transmission line separation distances  $d$ .**

The detuning in case 1 is attributed to parallel inductive loading increasing the resonance frequency, whereas in case 2, shunt capacitive loading causes the frequency to decrease.

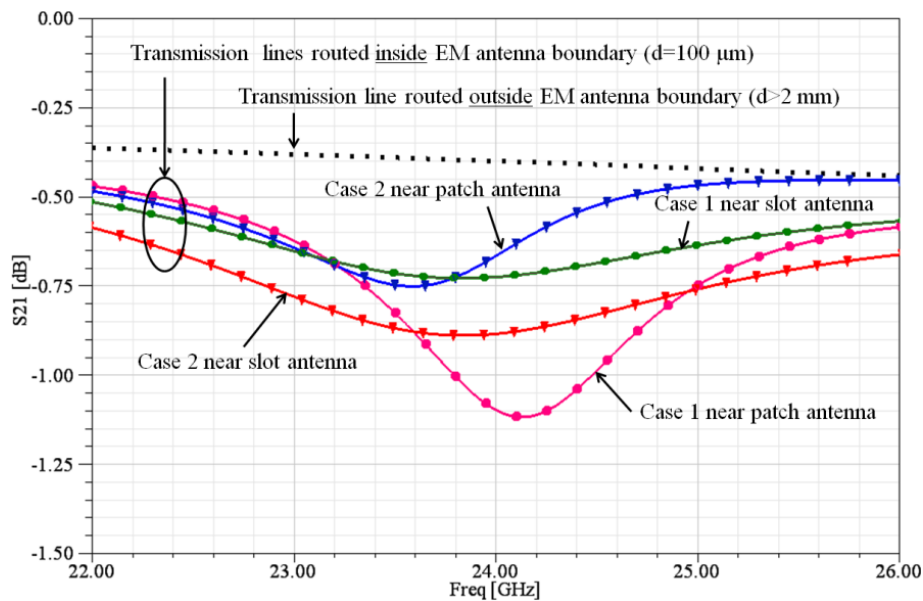


**Figure 38: Effects on the insertion loss of the microstrip transmission line routed inside the antenna boundaries.**

The strong electromagnetic interactions occurring when the transmission line is routed inside the electromagnetic antenna boundary also have effects on the transmission line parameters.

Consider the simulated transmission coefficient  $S_{21}$  between the IOs of the microstrip line as depicted in Figure 38. The transmission line has a total length of 6.25 mm in each case.

The transmission coefficient of the microstrip line was simulated in the case that the line is routed outside the electromagnetic antenna boundary. This is used as a reference. It is observed that the electromagnetic interactions with the antenna are negligible in this case, and the insertion loss remains unperturbed. The transmission coefficients of the different transmission line routing paths in the vicinity of the patch and slot antenna undergo degradation concerning their attenuation. As can be observed, the fields on the transmission line strongly couple to the resonance modes of the antennas. The highest transmission loss is observed at the antenna resonance frequencies.

The results in this subsection have shown that the electromagnetic antenna boundary can be used to determine the critical region around the antenna where the weak coupling assumption is not fulfilled. Degradation of the antenna parameters must be considered if transmission lines are routed within the electromagnetic antenna boundary. Keeping transmission lines outside the electromagnetic antenna boundary ensures that the antenna parameters are not altered significantly.

### 2.3.5.2 Influence of Ground Plane Size

The ground plane of the planar antenna plays a significant role for the distribution of reactive power density and, hence, the resulting antenna parameters. Therefore, the influence of the ground plane size on the antenna gain is studied on all three planar antenna configurations.

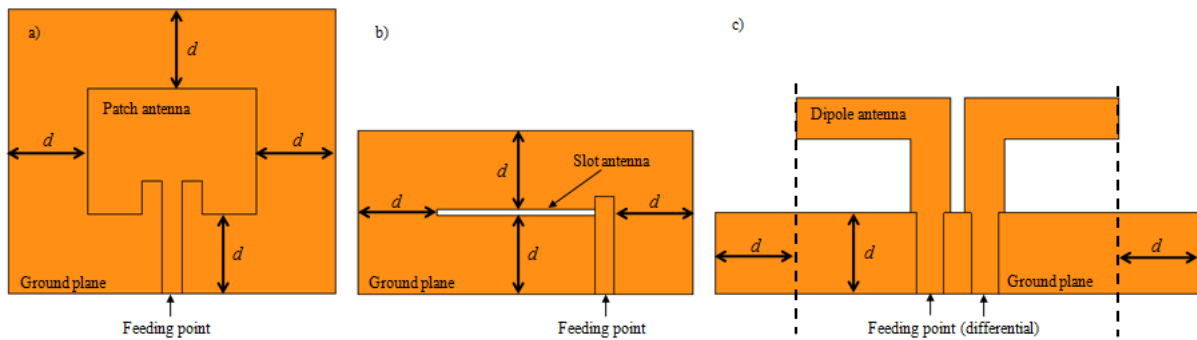


Figure 39: Illustration of the planar antennas with reduced ground plane sizes.

Consider Figure 39, where the antenna configurations with their respective ground planes are shown. For illustrative purposes, the substrate is not visible. The parameter  $d$  is introduced to



define the ground plane size respective to the physical antenna size. In the case of the patch and slot antennas, the ground plane sizes are directly related to the patch and slot sizes, respectively. In the case of the dipole antenna, the distance between the dipole and ground plane is preserved, since it acts as a reflector and is, thus, part of the antenna. It should also be noted that the ground plane width and length are varied together as described by  $d$  for all three antennas. The electromagnetic antenna boundaries are evaluated at the distance where the rectangular size of the ground plane is at least the size as defined by the antenna boundaries i.e., at  $d=\max\{\Delta l/2, \Delta w/2\}$ .

The influence of the ground plane size on the antenna gains is studied. Figure 40 shows the plot of the simulated antenna gains in dependency of the ground plane sizes as described by  $d$ .

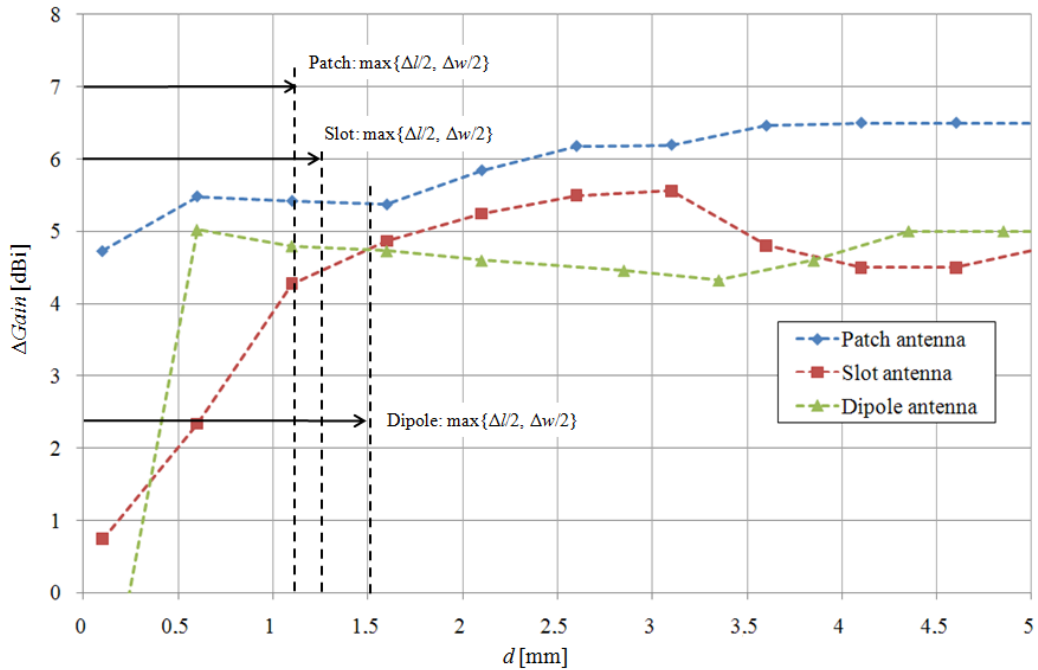


**Figure 40: Simulation results of the effects of reduced ground plane sizes on the antenna gains.**

The gain is evaluated in fixed directions. The patch antenna gain is given in positive  $z$  direction. The slot antenna gain is given in negative  $z$  direction. The dipole antenna gain is given in positive  $x$  direction. In the case of the patch antenna, the gain gradually increases with increasing values of  $d$  until it stabilizes at approximately 6.5 dBi. This is the value of the gain that was computed previously for large ground plane dimensions of 25 mm X 25 mm. The gain of the slot antenna is below 4 dBi for  $d < 1$  mm. This can be explained by the reduced lateral space that the slot current, flowing around the perimeter of the slot, has on the ground plane. The intermediate ground plane size, before the gain reaches 4.5 dBi for  $d > 4$  mm, is

explained by an overcompensation of the stray fields. Notice that in the case of the dipole antenna, the gain is below 0 dBi for  $d=0.1$  mm. Similarly to a Yagi-Uda antenna, the small ground plane acts like a director (shorted parasitic resonant dipole element) and not as a reflector and, hence, distorts the desired radiation pattern. For all antenna gain values, however, it is observed that their maximum changes, for ground plane sizes larger than the electromagnetic antenna boundaries, are below 1 dB. The gain values settle on larger ground planes.

Considering these results, it is concluded that the size of the ground is a crucial performance determining component of planar antennas. The size of the ground plane should be kept at least larger than the area specified the electromagnetic antenna boundary.

### 2.4 Summary

In this chapter, an approach for defining the electromagnetic antenna boundary was introduced. The approach is based on evaluating the distribution of reactive power density excited by the planar antenna on the ground plane and determining a threshold value.

As a starting point, a theoretical analysis of excited antenna fields was conducted at the beginning of this chapter in Section 2.2. The complex Poynting vector was used to characterize the propagating space and surface wave fields as well as the reactive near-fields, which are excited by planar antennas at board level. Modeling and simulation results for quantifying the influence of the dielectric substrate and antenna feed on the excited fields were presented. It was shown that the substrate height and antenna feed have significant influence on the magnitude of the excited fields of the antenna.

In Section 2.3, simulation and measurement results of three planar antennas, comprising a patch, slot and dipole configuration for operation at 24 GHz, were presented. The electromagnetic antenna boundaries were deduced. The influences of microstrip transmission lines, routed inside the electromagnetic antenna boundaries as well as the effects of finite ground plane sizes on the antenna gain were quantified.

The results in this chapter have shown that the electromagnetic antenna boundary can be used to: (1) define the block out region around the antenna where no board components should be placed; and (2) define the actual electromagnetic antenna size. This is beneficial for the integration of planar antennas since the antenna can now be treated as an “isolated” board component with respect to its electrical characteristics.

### 3 Calculation of Coupling to Transmission Lines

In the design phase of a wireless module, it is desirable to determine favorable positions and orientations of the transmissions lines routed in the vicinity of the planar antenna without performing extensive full-wave simulations for each possible case. Due to their open field structure, planar transmission lines are inherently sensitive to coupling from antenna fields. Thus, they may serve as prototypes of victims. In the previous chapter, an approach for defining the electromagnetic antenna boundary was developed. Transmission lines, placed within the electromagnetic antenna boundary, interact strongly with the near-field of the antenna such that the antenna parameters are potentially degraded. However, antenna fields also couple to transmission lines placed outside the electromagnetic antenna boundary on the same substrate. In this case, the weak coupling assumption is fulfilled. Based on this, an efficient method to calculate coupling is developed.

A typical example of the minimum isolation for an integrated antenna from the system is given in [101]. Here a maximum tolerable coupling value of -30 dB is required to obtain the desired bit-error-rate (BER) of  $10^{-6}$  at the receiver emphasizing the importance of rigorously examining the influence of undesired coupling during system design.

#### 3.1 Overview of Proposed Method

The proposed method is based entirely on a post processing step to a full-wave field simulation. This implies that the coupling is calculated based on the previously computed fields of the antenna. Although the weak coupling assumption is made i.e., the secondary fields excited on the transmission line have negligible influence on the primary antenna fields, the coupling is nevertheless reciprocal (see Section 2.2.1.3). All materials considered are isotropic and linear. Figure 41 shows an overview of the proposed method.

First, the magnetic field components, tangential to and on the ground plane,  $\underline{H}_x$  and  $\underline{H}_y$ , are computed for the designed antenna configuration. Next, the transmission line parameters of the transmission line, which is to be routed on the antenna substrate, are computed, using a 2D quasi-static or full-wave solver. The per-unit-length transmission line parameters, specifically the inductance  $L'$  and capacitance  $C'$  per-unit-length, are extracted. Based on the routing path  $p$  of the transmission line, the distributed current  $\underline{I}'_s$  and voltage  $\underline{U}'_s$  sources along the transmission line are determined. These distributed sources satisfy the inhomogeneous telegrapher's equations as will be shown in the next section.

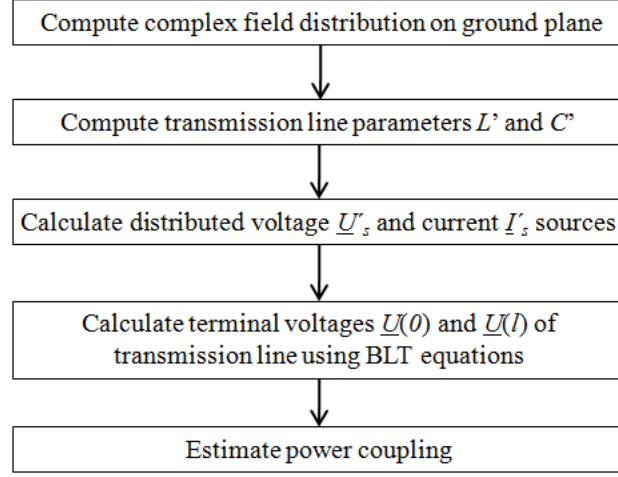


**Figure 41: Overview of method to calculate coupling from antenna fields to transmission lines.**

Figure 42 shows an illustration of a possible transmission line routing path  $p$  with all the relevant parameters. The letter  $p$  will be used as the natural parameterization ( $0 \leq p \leq l$ ) for the transmission line routing path. The terminal voltages  $\underline{U}(0)$  and  $\underline{U}(l)$  are calculated using the BLT (Baum, Liu, Tesche) integral formulations. Finally, together with the antenna input voltage  $U_{in}$ , coupling terms between the antenna and transmission line are estimated.

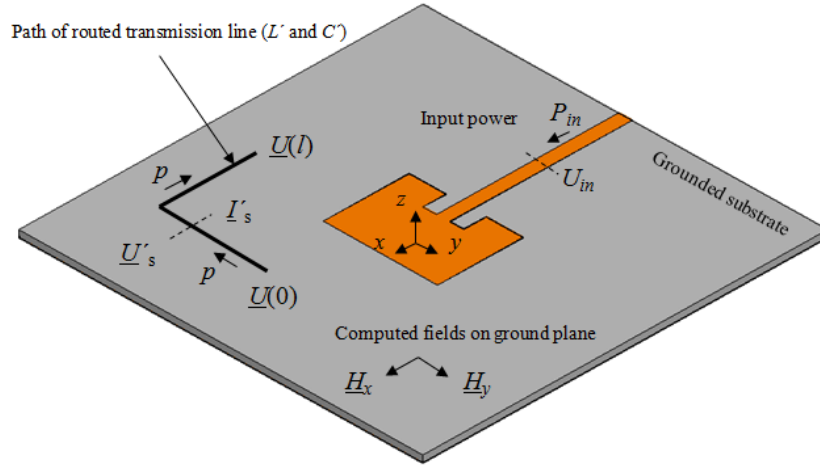


**Figure 42: Illustration of method to calculate coupling from antenna fields to transmission lines.**

### 3.2 Development of Coupling Model

In order to derive a model for the coupling of the antenna fields to transmission lines, distributed sources along the transmission line need to be derived. These distributed sources

are integrated over the transmission line path  $p$  to obtain terminal voltages at the ends. As a starting point, the telegrapher's equations are modified for the inhomogeneous case.

The telegrapher's equations (25) and (26) for the voltage and current on a transmission line are modified to include the coupling from an external field to the transmission line [56]. To illustrate this, Figure 43 shows the configuration of a terminated microstrip line on top of a grounded dielectric substrate. For simplicity, it is assumed that the transmission line is routed only in  $x$  direction i.e.,  $p=x$ . The derived equations are easily extended to include also a  $y$  directed routing path.

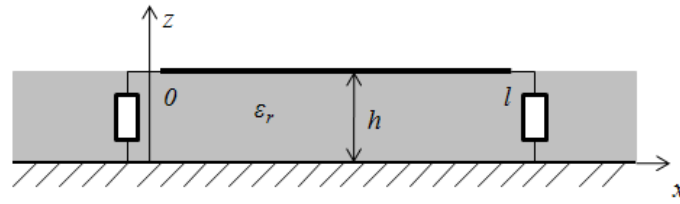


Figure 43: Configuration of a microstrip transmission line on a grounded substrate.

In order to derive the induced voltage on a transmission line from an external magnetic field excited by the antenna [56], the starting point is intuitively Faraday's law of induction (2), written in integral form by employing Stokes' theorem:

$$\oint_{\partial A} \vec{E} d\vec{s} = -j\omega\mu_0 \iint_A \vec{H} d\vec{A} \quad (94)$$

The contour integral of the electric field is calculated along the perimeter of the signal and reference conductors. The surface element  $d\vec{A}$  is  $y$  directed. Considering only one infinitesimally short transmission line section  $\Delta x$  yields the following expression:

$$\begin{aligned} & \int_0^h \underline{E}_z(x + \Delta x, z) dz - \int_0^h \underline{E}_z(x, z) dz \\ & + \int_x^{x+\Delta x} \underline{E}_x(x, 0) dx - \int_x^{x+\Delta x} \underline{E}_x(x, h) dx \\ & = j\omega\mu_0 \int_0^h \int_x^{x+\Delta x} \underline{H}_y(x, z) dx dz \end{aligned} \quad (95)$$

Enforcing the condition that the transmission line is lossless simplifies the above equation significantly since the tangential electric fields  $\underline{E}_x$  on the transmission line are zero.

Furthermore, if the height of the transmission line  $h$  is small compared to the signal wavelength, a line voltage can be defined:

$$\underline{U}(x) = \int_0^h \underline{E}_z(x, z) dz \quad (96)$$

The transverse fields on the transmission lines, hence, are assumed to behave as static fields. The total voltage per-unit-length on the transmission line is given by:

$$\frac{d\underline{U}(x)}{dx} = -j\omega\mu_0 \int_0^h \underline{H}_y(x, z) dz \quad (97)$$

Furthermore, in the case that the substrate height  $h$  is assumed electrically short, the integral can be approximated by a multiplication i.e., the magnetic field is independent of  $z$  and the substrate height  $h$ .

$$\frac{d\underline{U}(x)}{dx} = -j\omega\mu_0 h \underline{H}_y(x) \quad (98)$$

Although this is an approximation and only valid for very thin substrate heights,  $h \rightarrow 0$ , it shows that the induced voltage per-unit-length is roughly proportional to the magnetic field orthogonal to the transmission line.

It must be noted at this stage that the magnetic field describes the total magnetic field comprising the incident field i.e., the excitation field of the antenna  $\underline{H}_{y, antenna}$ , and the field from the transmission line mode  $\underline{H}_{y, tml}$ .

$$\frac{d\underline{U}(x)}{dx} = -j\omega\mu_0 h \left( \underline{H}_{y, tml}(x) + \underline{H}_{y, antenna}(x) \right) \quad (99)$$

It is observed that the first term in brackets resembles the per-unit-length inductance  $L'$  of the transmission line. Therefore, the first telegrapher's equation with a distributed voltage source term  $\underline{U}'_s(x)$  is deduced directly.

$$\frac{d\underline{U}(x)}{dx} + j\omega L' \underline{I}(x) = \underline{U}_s'(x) \quad (100)$$

The first telegrapher's equation is now inhomogeneous because it contains a source term  $\underline{U}_s'$ .

$$\underline{U}_s'(x) = -j\omega\mu_0 h \underline{H}_{y, antenna}(x) \quad (101)$$

For reasons of simplicity, the magnetic field excited by the antenna will be referred to as  $\underline{H}_y$ , and not  $\underline{H}_{y, antenna}$  from here on.

$$\underline{U}_s'(x) = -j\omega\mu_0 h \underline{H}_y(x) \quad (102)$$

In a similar manner, Ampere's law (1) can be used to derive the second inhomogeneous telegrapher's equation [56]. Here the theorem is applied to a closed surface  $A_c$  so that the integral over the curl of the magnetic field vanishes.

$$\iint_{A_c} (\vec{\nabla} \times \vec{H}) d\vec{A}_c = 0 = \iint_{A_c} (j\omega\epsilon \vec{E} + \vec{J}) d\vec{A}_c \quad (103)$$

Note that  $A_c$  is interpreted as a closed cylinder surface of length  $\Delta x$  surrounding the signal conductor. Considering the directions of both electric field and current density, the following expression can be set up:

$$\underline{I}(x + \Delta x) - \underline{I}(x) + j\omega\epsilon \iint_{A_c} \vec{E} d\vec{A}_c = 0 \quad (104)$$

$\underline{I}$  is the current flowing on the transmission line.  $A_c$  denotes the "side wall" of the cylinder.

This is the field theory equivalent formulation of Kirchhoff's well known circuit law.

The total charge on the transmission line is given by the charge induced by the antenna fields  $q_{antenna}$  and the charge of the transmission line mode  $q_{tml}$ . The charge can also be expressed in terms of capacitance and voltage.

$$j\omega\epsilon\iint_{A_c}\vec{E}d\vec{A}_c = j\omega\left(\underline{q}_{antenna}(x) + \underline{q}_{lml}(x)\right) = j\omega C'(\underline{U}(x) + \underline{E}_z(x)h)dx \quad (105)$$

Considering the RHS of (105), it is observed that the voltage on the transmission line is split up into the term  $\underline{U}(x)$  of the transmission line mode and the term  $\underline{E}_z(x)h$  induced by the antenna fields on the transmission line. Finally, the second inhomogeneous telegrapher's equation with the distributed current source term  $\underline{I}'_s(x)$  is deduced.

$$\frac{d\underline{I}(x)}{dx} + j\omega C'\underline{U}(x) = \underline{I}'_s(x) \quad (106)$$

$$\underline{I}'_s(x) = -j\omega C'h\underline{E}_z(x) \quad (107)$$

The electric field can also be expressed in terms of the magnetic field, using Maxwell's first equation (1).

$$\underline{E}_z(x) = \frac{1}{j\omega\epsilon}\left(\frac{\partial}{\partial x}\underline{H}_y(x) - \frac{\partial}{\partial y}\underline{H}_x(x)\right) \quad (108)$$

At this point, the distributed sources of the transmission line with external excitation by the antenna fields have been derived. The fields must be integrated along the transmission line, considering the propagation constant and impedance characteristics of the transmission line in order to obtain the terminal responses. For this purpose, the BLT (Baum, Liu and Tesche) equations [56] are used. The transmission line parameters  $L'$ ,  $C'$  and  $\beta$  must be known.

$$\underline{U}(x=0) = -\frac{1}{2}\int_0^l(\underline{U}'_s(x) - Z_0\underline{I}'_s(x))\exp(j\beta l - j\beta x)dx \quad (109)$$

$$\underline{U}(x=l) = \frac{1}{2}\int_0^l(\underline{U}'_s(x) + Z_0\underline{I}'_s(x))\exp(j\beta x)dx \quad (110)$$

Note that the transmission line is assumed impedance controlled and matched at the terminals such that the reflection coefficients at the loads are small and can be neglected. The



transmission line losses are also considered negligible. E.g., the losses of the microstrip transmission line from Table 10 in Appendix 3 are small ( $\omega L' \gg R'$  and  $\omega C' \gg G'$ ) and can be neglected for this analysis. Therefore, the characteristic transmission line impedance  $Z_0$  is real. Expanding these equations yields the following terms.

$$\begin{aligned} \underline{U}(x=0) &= \frac{j\omega\mu_0 h}{2} \exp(j\beta l) \int_0^l \underline{H}_y(x) \exp(-j\beta x) dx \\ &\quad - \frac{C'h}{2\varepsilon} Z_0 \exp(j\beta l) \int_0^l \left( \frac{\partial}{\partial x} \underline{H}_y(x) - \frac{\partial}{\partial y} \underline{H}_x(x) \right) \exp(-j\beta x) dx \end{aligned} \quad (111)$$

$$\begin{aligned} \underline{U}(x=l) &= -\frac{j\omega\mu_0 h}{2} \int_0^l \underline{H}_y(x) \exp(j\beta x) dx \\ &\quad - \frac{C'h}{2\varepsilon} Z_0 \int_0^l \left( \frac{\partial}{\partial x} \underline{H}_y(x) - \frac{\partial}{\partial y} \underline{H}_x(x) \right) \exp(j\beta x) dx \end{aligned} \quad (112)$$

At this stage, the transmission line terminal voltages  $\underline{U}(0)$  and  $\underline{U}(l)$  have been formulated in dependency of the exciting antenna fields. To estimate the coupling, the antenna terminal voltage is required. The antenna driving voltage  $U_{in}$  can be estimated based on the input power  $P_{in}$  and feeding line impedance  $Z_0$ . Note that the phase of  $U_{in}$  is suppressed. The antenna should also be matched with a low input reflection coefficient <-10 dB for accurate results.

$$U_{in} = \sqrt{2P_{in}Z_0} \quad (113)$$

Now the coupling coefficients are formulated. Only the power transmission is of interest for the coupling model. Therefore, only the S-parameter magnitudes  $S_{12}$  [dB] and  $S_{13}$  [dB] are considered respective to the ports (terminals) of the transmission line.

$$S_{12} [dB] = 20 \log \left( \frac{|\underline{U}(x=0)|}{U_{in}} \right) dB \quad (114)$$

$$S_{13} [dB] = 20 \log \left( \frac{|\underline{U}(x=l)|}{U_{in}} \right) dB \quad (115)$$

**Generalization for an arbitrary routing path  $p$ :** So far, the coupling model has only been derived for an  $x$  directed transmission line. Transmission lines can be routed arbitrarily in  $x$  and  $y$  directions (2D). Therefore, the coupling model needs to be generalized to account for this. The first step is to modify the distributed voltage and current sources (102) and (107) along the transmission line to include  $x$  and  $y$  dependencies, which are included in  $p$ .

$$\underline{U}'_s(p) = -j\omega\mu_0 h \underline{H}_\perp(p) \quad (116)$$

$$\underline{I}'_s(p) = -\frac{C'h}{\varepsilon} \left( \frac{\partial}{\partial x} \underline{H}_y(p) - \frac{\partial}{\partial y} \underline{H}_x(p) \right) \quad (117)$$

Note the field component  $\underline{H}_\perp(p)$  is introduced describing the orthogonal magnetic field component along the transmission line. Secondly, the integration paths of (109)-(112) are modified for integration along the transmission line path  $p$ , which is routed in  $x$  and  $y$  direction. With these modifications, the coupling model is generalized for arbitrary 2D transmission line paths on the ground plane.

As a result, it has been shown that the induced voltage  $\underline{U}'_s$  and current  $\underline{I}'_s$  per-unit-length on a transmission line are proportional to the external magnetic field orthogonal to the transmission line (116) and its spatial derivative (117). Therefore, transmission lines can be systematically placed, based on the magnetic field distribution excited by the planar antenna on the ground plane. For this purpose, the magnetic field excited by the antenna is decomposed into the two tangential components  $\underline{H}_x$  and  $\underline{H}_y$  on the ground plane.

Figure 44 shows a plot of the tangential magnetic field components excited by the 24 GHz patch antenna on the ground plane. Favorable transmission line positions and orientations can be deduced qualitatively based on the magnetic field distribution. The marked positions indicate low, moderate and high potential coupling, respectively. E.g., a critical position for a transmission line orientated in the same direction as the antenna mode current is at the non radiating apertures of the patch antenna where the  $x$  component of magnetic field is high.

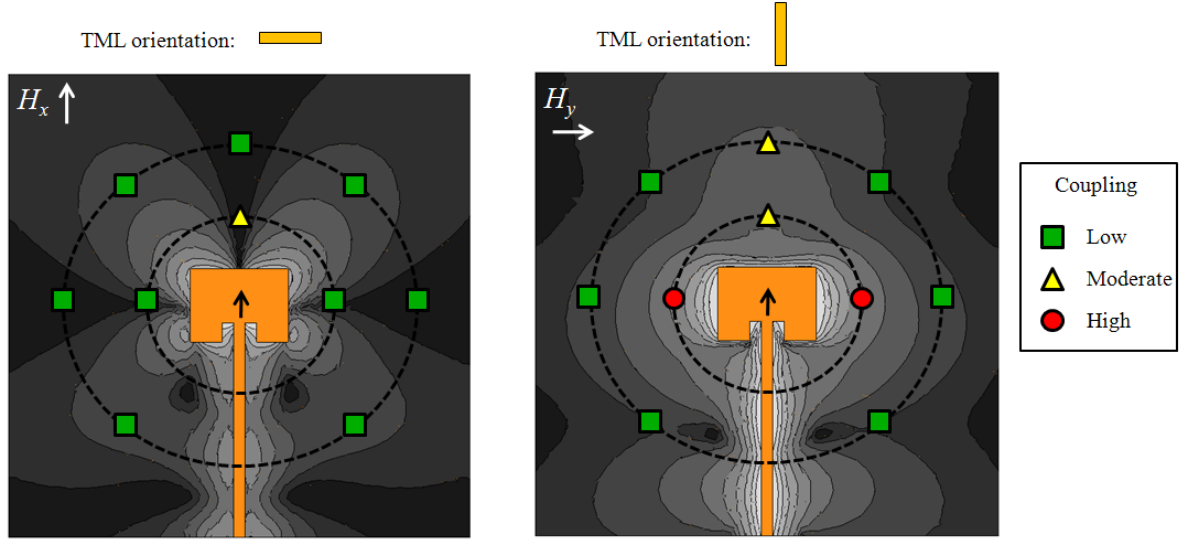


Figure 44: Simulation of the magnetic field distribution of the patch antenna split up into the two tangential components on the ground plane.

Finally, in the following a summary of the simplifications and assumptions of the coupling is given:

- Weak coupling is assumed i.e., the secondary fields excited on the transmission lines have no influence on the primary antenna fields. In other words, the transmission line must be placed outside the electromagnetic antenna boundary.
- Quasi TEM mode wave propagation is assumed on the transmission line so that it can be modeled with characteristic per-unit-length parameters.
- The effects of transmission line discontinuities are assumed to have negligible influence on the propagation of the QTEM mode in comparison to a straight transmission line.
- Only the tangential magnetic field components on the ground plane are evaluated to determine the coupling. The normal magnetic field is assumed zero. This is only valid for high ground plane conductivity values.
- The spatial dependency of the magnetic field on the height in the substrate is assumed constant for  $0 < z < h$ . This is only valid for electrically small substrate heights  $h \ll \lambda$ .

- The transmission line is assumed matched at both terminals. Therefore, standing waves and resulting transmission line resonances are assumed negligible.

Consequently, the accuracy of the coupling model needs to be quantified. This is done in the next section.

### 3.3 Quantification of Coupling Model

In order to illustrate the feasibility of using the magnetic field components on the ground plane to calculate the coupling to neighboring transmission lines, case studies were conducted, and the results are compared to complete full-wave simulations. The three planar antenna configurations that were designed and characterized in Section 2.3 are used to quantify the accuracy of the proposed coupling model. Impedance controlled and matched terminated microstrip transmission lines were routed in the vicinity of these antennas.

#### 3.3.1 Planar Antenna to Microstrip Line Coupling

Figure 45 shows four possible transmission line orientations in the vicinity of the patch, slot and dipole antennas denoted cases 1-4. The microstrip line is impedance controlled with a characteristic impedance of  $50\ \Omega$  (see Appendix 3 for details on the transmission line parameters). The line is terminated with  $50\ \Omega$  lumped ports ( $p_2$  and  $p_3$ ) at each end. The antenna is driven through port  $p_1$  at the end of the feeding line.

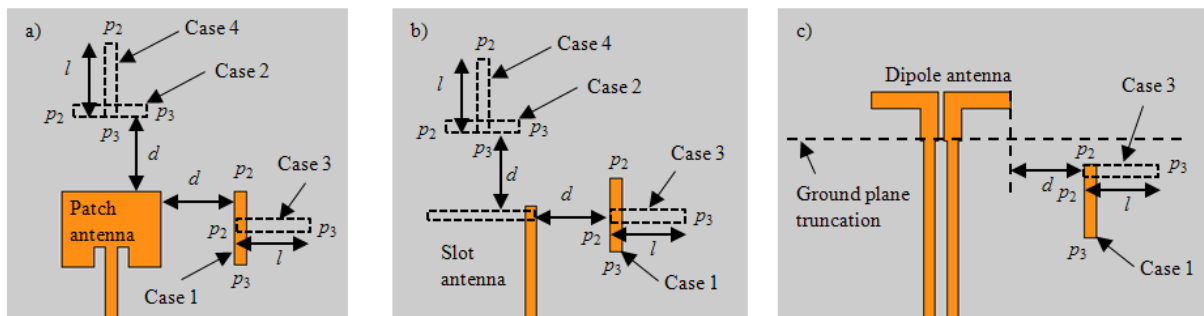
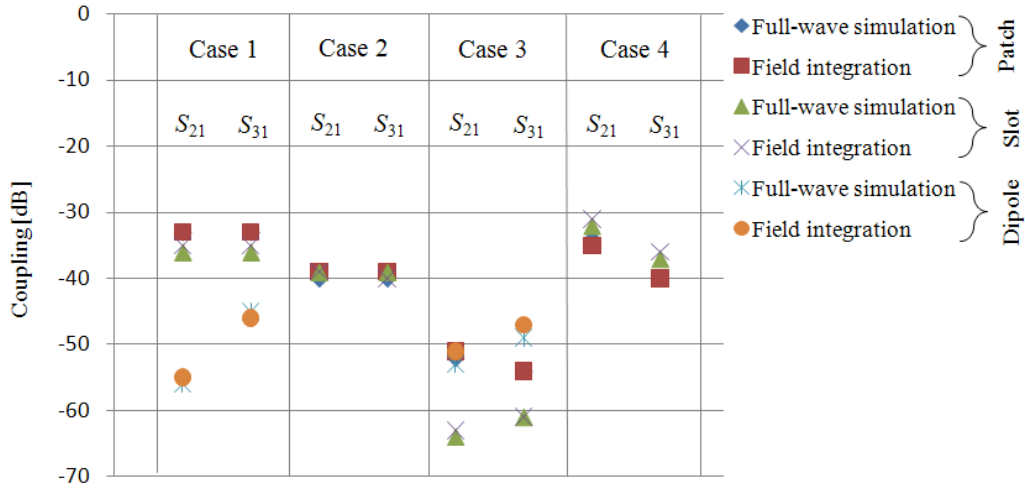


Figure 45: Overview of the different cases used to study the coupling between the three planar antennas and the microstrip transmission lines.

In case 1, the microstrip line is parallel to the feeding lines and at the side of the antennas. In case 2, the microstrip line is orientated orthogonally to the feeding lines and is in front of the

antennas. Case 3 has the same transmission line orientation as case 2 but in this case, the microstrip line is placed beside the antennas. Likewise, case 4 has the same line orientation as case 1 but the line is placed in front of the antennas. Notice that the ground plane underneath the dipole antenna is truncated. Thus, grounded transmission lines cannot be placed in front of and directly beside the dipole element. Therefore, only slightly modified cases 1 and 3 are considered for the dipole antenna. The separation distance  $d$  and transmission line length  $l$  define the location and length of the transmission line on the substrate. Figure 46 shows a comparison between complete full-wave simulations and the coupling model (field integration).



**Figure 46: Comparison of full-wave simulation with field integration (coupling model) results for the patch, slot and dipole antenna with  $l = \lambda/4$  and  $d = \lambda/4$ .**

Both parameters  $d = 3.125$  mm and  $l = 3.125$  mm, corresponding to a quarter wavelength  $\lambda$  at 24 GHz, are selected for this first comparison. The transmission line was routed outside the electromagnetic antenna boundaries. The results of the coupling model (field integration) are obtained by evaluating (114) and (115) based on the previously computed magnetic field distribution of the antenna with no transmission lines on the substrate. To obtain the full-wave simulation results, the entire transmission line is simulated together with the antenna.

It is observed that a good correlation between full-wave simulation and field integration is obtained. A discrepancy of less than 1 dB is obtained for all transmission line routing cases and antenna types. The highest coupling values are obtained for cases 1 and 4 when the transmission line is parallel to the current anti nodes on the antennas. The coupling to the dipole antenna for cases 1 and 3 is smaller compared to the coupling in the other cases. This

can be attributed to the differential nature of the dipole i.e., the magnetic field strengths excited by the dipole on the ground plane are smaller than those excited by the patch and slot antennas (see Figure 32).

Next, the influence of different transmission line lengths  $l$  and separation distances  $d$  are studied. For this purpose, the patch antenna configuration is considered. Three values of  $l$ , including 1.563 mm ( $\lambda/8$ ), 3.125 mm ( $\lambda/4$ ) and 12.5 mm ( $\lambda$ ), as well as three values of  $d$ , including 1.563 mm ( $\lambda/8$ ), 3.125 mm ( $\lambda/4$ ) and 6.25 mm ( $\lambda/2$ ), are considered. Notice that in all cases, the transmission line is again routed outside the electromagnetic antenna boundary. Figure 47 to Figure 50 show the obtained results for cases 1, 2, 3 and 4. A comparison between complete full-wave simulation and field integration is conducted.

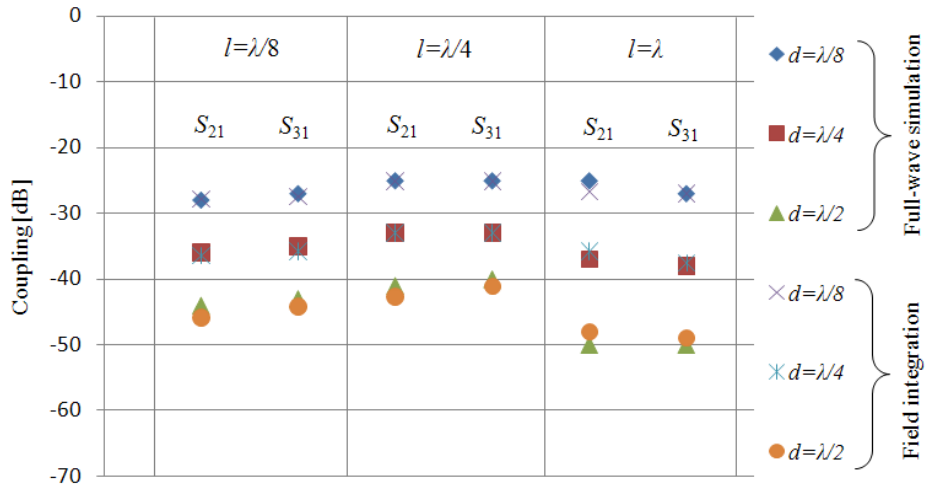


Figure 47: Comparison of full-wave simulation with field integration (coupling model) results for case 1.

In Figure 47, it is observed that the predicted coupling values obtained by field integration and full-wave simulation are within 2 dB accuracy in comparison to each other.

Similarly to case 1, the coupling values obtained by field integration and full-wave simulation for case 2 in Figure 48 correlate well. The biggest discrepancy of 2 dB is observed for the coupling values of the long transmission line with  $l=\lambda$ .

The separation distance  $d$  has more influence on the magnitude of the coupling than the line length  $l$ . The phase and amplitude of the magnetic field are not uniformly distributed along the transmission line paths. Furthermore, the individual contributions of the distributed sources along the transmission line are integrated with the appropriate phase of the transmission line mode yielding constructive and destructive forms of superposition at the transmission line terminals.

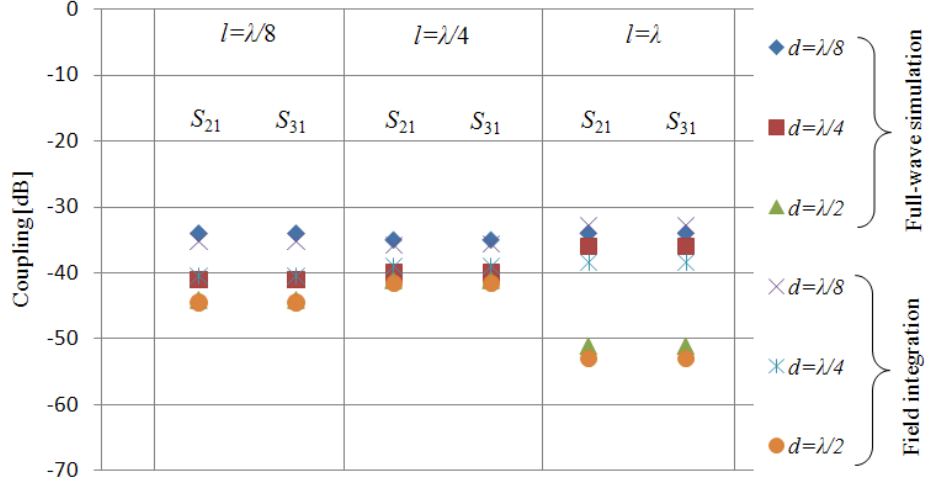


Figure 48: Comparison of full-wave simulation with field integration (coupling model) results for case 2.

For case 3, all the coupling values in Figure 49 are well below -40 dB. This results from the direction of the magnetic flux density being primarily parallel to the transmission line. This is also observed in Figure 44.

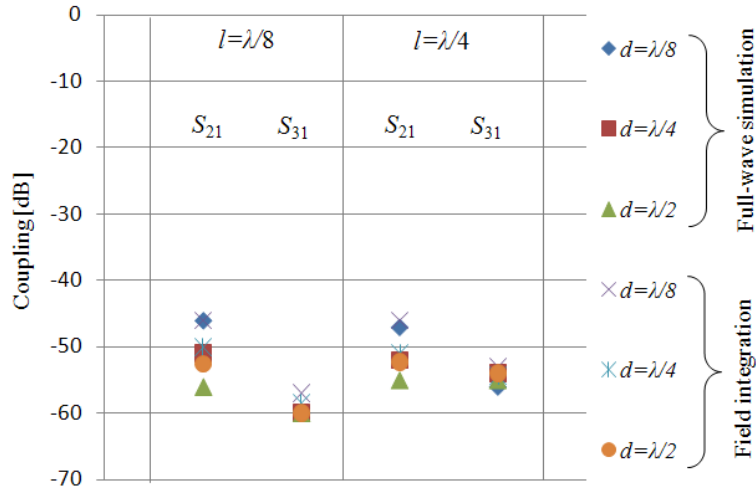


Figure 49: Comparison of full-wave simulation with field integration (coupling model) results for case 3.

The long transmission line with  $l=12.5$  mm is not considered for cases 3 and 4 because a large portion of the board would be required for routing. Finally, the results of the coupling for case 4 are depicted in Figure 50. The coupling to  $p_3$  is smaller than to  $p_2$  since  $p_2$  is closer to the antenna.

As a result, it is concluded that the predicted coupling values using the developed coupling model yield results with an accuracy of at least 2 dB compared to complete full-wave

simulations for a variety of antenna types, transmission line lengths, orientations and positions.

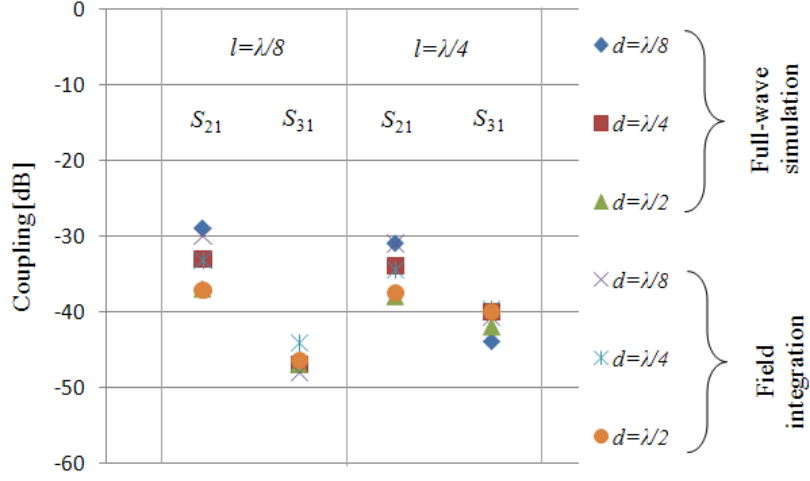


Figure 50: Comparison of full-wave simulation with field integration (coupling model) results for case 4.

### 3.3.2 Spectral Response of Complete Transmission Line Path

So far, the transmission line was uniform with no bends. However, in a realistic scenario, a routed transmission line can have multiple bends. Furthermore, it is of interest to evaluate not only one frequency point but an entire frequency band around the resonance frequency of the antenna. Therefore, the coupling model is also quantified for these cases.

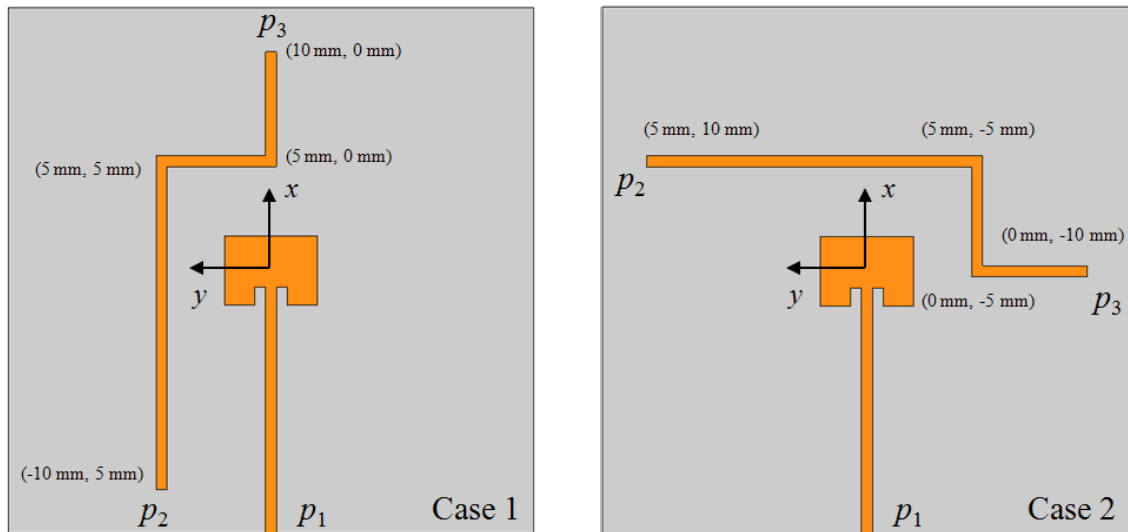
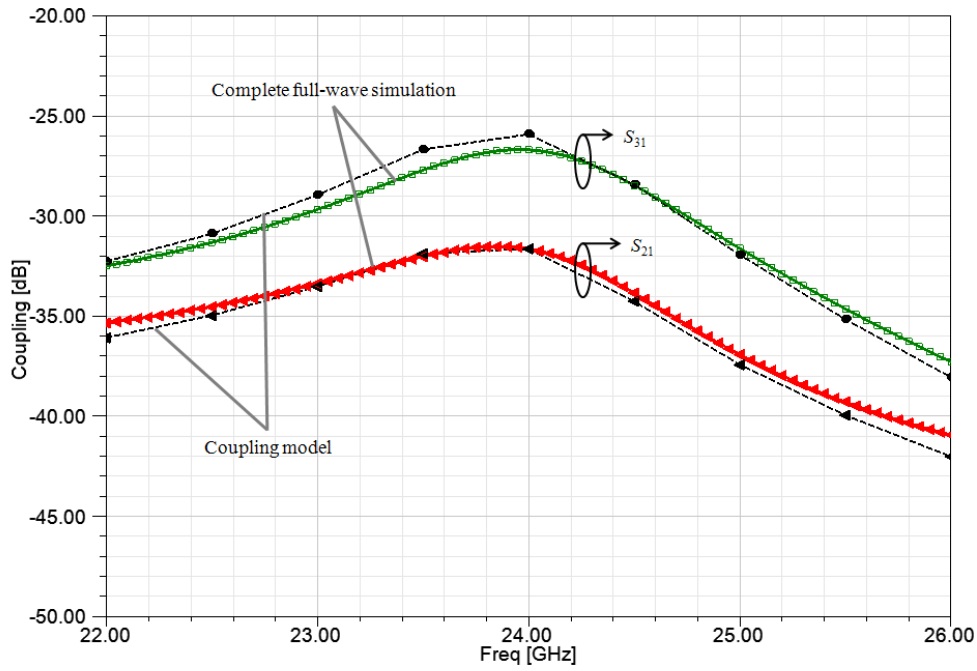


Figure 51: Overview of the patch antenna with the two transmission line routing cases with multiple bends. The  $x$ - $y$  coordinates specify the segments of the transmission line.



Figure 51 shows the two cases that are used in this study. The microstrip transmission line is routed past the antenna with two bends. It is matched terminated at the ends ( $p_2$  and  $p_3$ ). The patch antenna is fed through the feeding line at port  $p_1$ . The coupling is evaluated using the proposed coupling model (field integration) with the equations (114) and (115). The spectral response is obtained by evaluating the equations at discrete frequency points from 22 GHz to 26 GHz in 0.5 GHz steps. The magnetic fields of the excited antenna were computed at these frequency points prior to applying the coupling model.



**Figure 52: Comparison of full-wave simulation with field integration (coupling model) results with spectral response for case 1.**

The results are compared to complete full-wave simulations of the antenna and the transmission line. The frequency response was obtained by extrapolating the solution frequency at 24 GHz with a sweep. Figure 52 shows the results for case 1.

The coupling is largest at the resonance frequency of the antenna where the excited fields have maximum magnitude. It is observed that the coupling to  $p_3$  is larger than the coupling to  $p_2$ . The predicted coupling values by field integration are accurate within 1 dB compared to the complete full-wave simulation across the entire spectrum of interest.

Figure 53 shows the coupling results for case 2. Again, a satisfactory correlation between the field integration and full-wave simulation results is obtained across the entire frequency span. A maximum deviation of 2 dB is observed. The coupling to  $p_2$  is slightly higher than to  $p_3$ .

As a result, it is concluded that the proposed coupling model is suitable for efficiently calculating the spectral response of coupling from planar antennas to neighboring transmission lines with multiple bends.

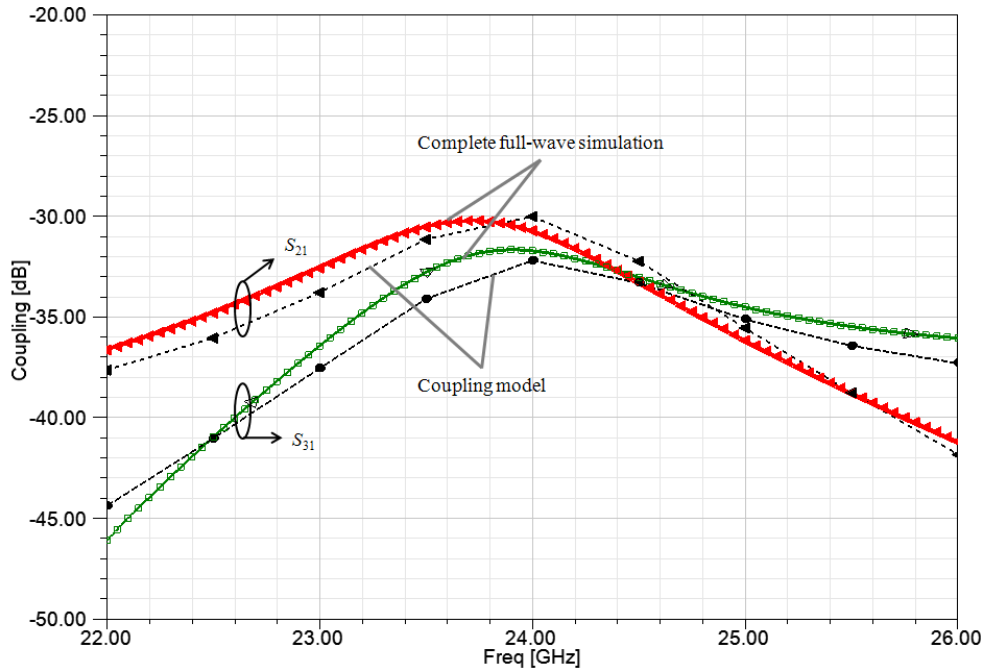
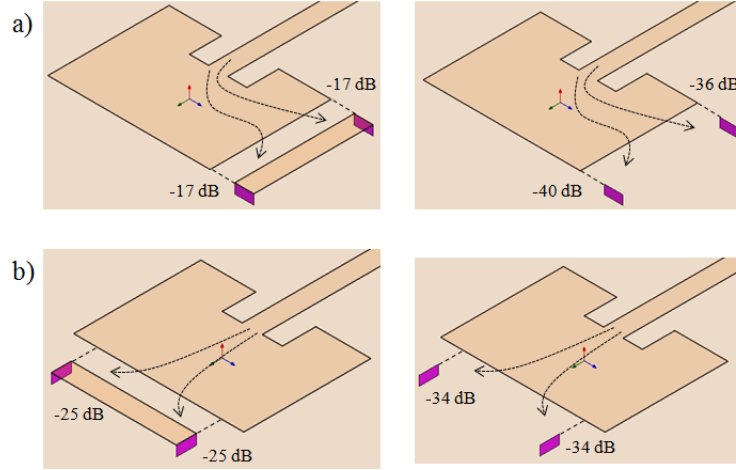


Figure 53: Comparison of full-wave simulation with field integration (coupling model) results with spectral response for case 2.

### 3.3.3 Simulation Errors caused by Lumped Ports

In the full-wave simulations, the lumped ports are not infinitesimally small such that a fraction of power couples directly to the ports. The ports are not included in the coupling model. Therefore, the influence of the ports on the coupling values needs to be quantified. Figure 54 shows the patch antenna with two different transmission line orientations with and without the transmission line. With this configuration, the magnitude of the coupling to the ports was examined.

The coupling to the ports reduces by 23 dB and 19 dB, respectively, for configuration (a) when the transmission line is removed. For configuration (b), the coupling is reduced by 9 dB for both ports when the transmission line is removed. These cases are considered a worst case scenario since the transmission lines and ports are placed directly at the electromagnetic antenna boundary. It is concluded that the coupling directly to the ports has negligible influence on the coupling results.



**Figure 54: 3D simulation models used to study the coupling to the ports for two transmission lines, (a) and (b), with and without the microstrip transmission line, respectively.**

### 3.3.4 Measurement Results

The full-wave simulation results, which are used to quantify the accuracy of the coupling model, need to be verified experimentally with measurements. Therefore, test structures of the patch antennas coupled to the microstrip transmission lines were designed and manufactured. The antenna is a one port network, and the transmission line is a two port network. Therefore, a full three port S-parameter measurement is required. With the three port measurement, all six coupling terms are characterized by magnitude and phase. Since the configurations are reciprocal, the problem reduces to three coupling terms. One of the three coupling terms is the transmission coefficient of the transmission line, which is not of interest here. Measurement results of the transmission line characteristics are presented separately in Appendix 4.

Figure 55 shows photos of two test structures (a) and (b) that were designed and manufactured. The antenna and transmission lines are contacted with GSG (ground, signal, ground) probes. At the ports  $p_1$ ,  $p_2$  and  $p_3$ , probe adapters were designed. These comprise three pads, two of which are shorted to the ground plane with vias. The manufacturing process and measurement environment is described in Appendix 4.

Since the transmission lines are placed close to the antenna for two test structures, it is necessary to ensure that the probe adapters are not too close to the patch antenna. This is necessary to ensure that stray antenna fields do not couple strongly to the GSG probes and, hence, falsify the measurement results. Furthermore, the probe positioners of the network analyzer are orientated orthogonally to one another. Therefore, the probe adapters also need to be orientated orthogonally to one another. For these two reasons, the bends were introduced at

the ends of the microstrip lines to facilitate the contacting with GSG probes. These additional bends are depicted in the simulation models and photos of Figure 55.

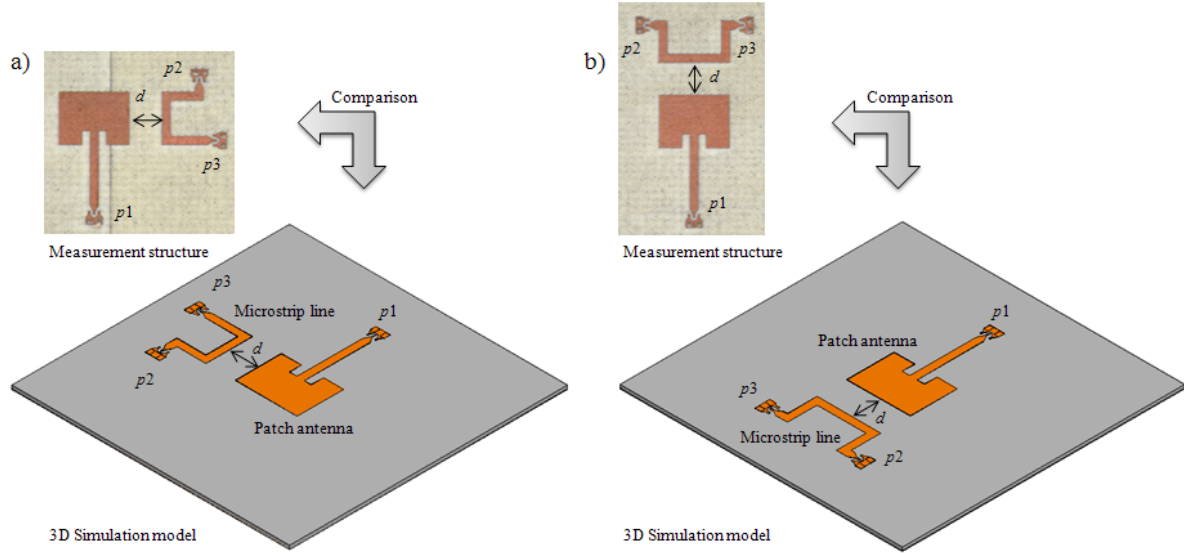


**Figure 55: Test structures and 3D simulation models used for experimental verification of the simulated coupling between the patch antenna and the microstrip transmission lines.**

Table 5 shows a summary of the measured coupling values of the test structures and a comparison to the results of the coupling model and complete full-wave simulations. Note that the effects of the GSG probe adapters are not included in the coupling model, in which an ideal termination is assumed.

Test structure	Coupling model		Full-wave simulation		Measurement	
	$S_{12}$ [dB]	$S_{13}$ [dB]	$S_{12}$ [dB]	$S_{13}$ [dB]	$S_{12}$ [dB]	$S_{13}$ [dB]
a	-28	-29	-31	-29	-31	-28
b	-32	-32	-30	-30	-29	-29

**Table 5: Comparison of the calculated, simulated and measured coupling values between the patch antenna and microstrip transmission lines at 24 GHz.**

A discrepancy of up to 3 dB is observed between the calculated values based on the coupling model and the simulation and measurement results. This is traced back to the parasitics of the GSG probe adapters and GSG probed themselves, which also couple to the fields. However, the measured coupling values match well with the results from the complete full-wave simulations. A discrepancy of 1 dB is observed here. The slight differences in measured and simulated data are also due to numerous effects. Influence factors include calibration inaccuracies, influences of the GSG probes and technological fluctuations. It must be

considered that the excited antenna fields do not only couple to the transmission lines but also directly to the GSG probes.

As a result, the full-wave simulations have been verified with measurements. Since the full-wave simulations have been used to quantify the accuracy of the coupling model, the results of the coupling model have also been verified.

### 3.4 Summary

In this chapter, a method for efficiently calculating electromagnetic coupling from planar antennas to neighboring transmission lines has been developed. The main advantage of the coupling model is that it is based on field integration of the previously computed magnetic fields on the ground plane of the excited antenna. Therefore, the coupling is calculated entirely in the post processing phase of full-wave simulations, and the coupling to different transmission line routing paths can be calculated without performing additional full-wave simulations for each routing path. By reciprocity, this also includes coupling from transmission lines, in this case the aggressor, to the antenna. It must, however, be ensured that the weak coupling assumption is fulfilled i.e., the transmission line must be routed outside the electromagnetic antenna boundary. Furthermore, it is assumed that the transmission lines are impedance controlled and matched at the ends.

The accuracy of the coupling model was quantified with a case study. It was shown that the method is suitable for efficiently obtaining coupling values to neighboring transmission lines of arbitrary length, with multiple bends as well as the spectral response.

Therefore, the coupling method efficiently supports the integration process of planar antennas in compact wireless modules by reducing simulation efforts.

## 4 Quantification of Planar Configurations to Reduce Coupling

This chapter focuses on the quantification of techniques to reduce undesired electromagnetic coupling as well as a comparison of these techniques with regards to shielding effectiveness and integration density. The focus is on shielding configurations, which can be implemented on a dielectric substrate with only two metallization layers and vias in order to facilitate low cost PCB applications.

As a starting point, the E- and H-plane coupling between two patch antennas was simulated and used as a basis for the comparison i.e., the patch antennas are used as the reference for the evaluation of the shielding effectiveness. The coupling between two resonant antennas is a worst-case-scenario. Therefore, the configurations should not be viewed from the point of an antenna array. The second antenna should rather be interpreted as a surface and space wave probe. Figure 56 shows two configurations comprising the E- and H-plane coupling cases.

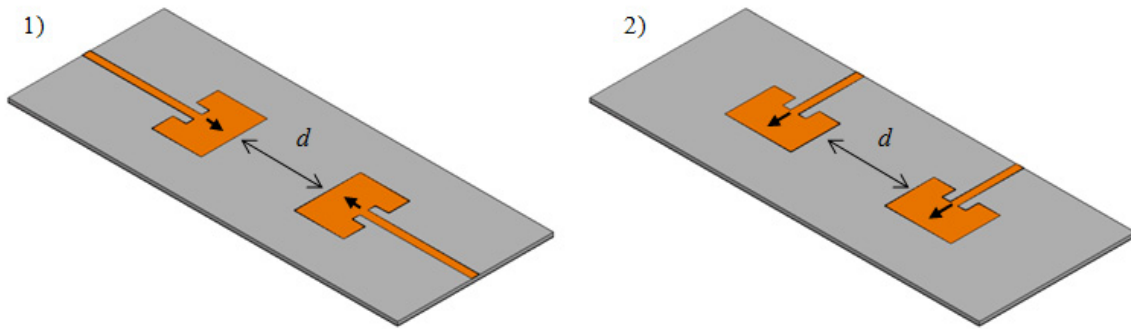


**Figure 56: 3D simulation models of the coupled patch antennas including: (1) E-plane case; and (2) H-plane case.**

The patch antennas are based on the same configuration and substrate build up that was used for the other antennas presented in Section 2.3. The coupling coefficient  $S_{21}$  between the ends of the feeding lines of the antennas was simulated for different separation distances  $d$  at the resonance frequency of the patch antennas (24 GHz).

Figure 57 shows the simulation results of the coupling. As is observed, the E-plane coupling is smaller for distances  $d < 2.5$  mm. Below this distance, the E-plane coupling between the antennas is primarily capacitive in nature resulting from the opposing charge densities at the radiating apertures of the antennas. However, the E-plane coupling "overtakes" the H-plane coupling for larger distances and does not decay as rapidly. Close to the antenna, where the H-plane coupling dominates, the primary coupling mechanism is inductive coupling. This

results from the parallel flowing currents on the antennas. It is evident that the inductive coupling is stronger than the capacitive coupling in the near-field.

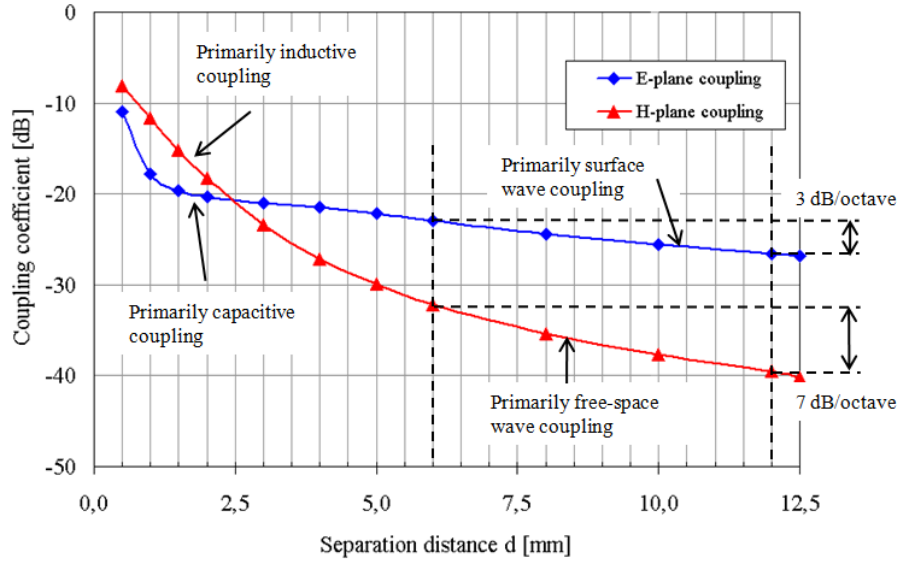


**Figure 57: Simulation results of the coupling coefficient  $S_{21}$  between the patch antennas at 24 GHz.**

The fast decreasing H-plane coupling beyond 2.5 mm is primarily attributed to the space wave coupling, which decays faster with distance compared to surface wave coupling. To illustrate this, the coupling is evaluated at a separation distance  $d$  of 6 mm and 12 mm, and the difference is calculated. The difference corresponds to a spatial decay rate of 7 dB/octave. The theoretical value for the decay rate of the space wave mode is 6 dB/octave. Thus, the primary coupling mechanism is the space wave. For the E-plane coupling case, on the other hand, the surface wave is the primary contributor. A decay rate of 3 dB/octave is observed. This corresponds to the theoretical decay rate for the surface wave mode. As a result, surface waves can cause significant coupling at board level, especially in the E-plane of patch antennas.

#### 4.1 Design and Implementation of Shielding Configurations

In the state-of-the-art presented in Section 1.2.2, two main sets of techniques for the reduction of coupling caused by surface waves were classified. The first approach is to attenuate the surface wave once it has been launched. The second approach is to design the planar antenna element in such a way that it does not excite surface waves. Therefore, in Section 4.1.1 and

Section 4.1.2, the results of the design and implementation of two of these configurations are presented and discussed.

#### 4.1.1 Planar Electromagnetic Bandgap (EBG) Structure

The impedance properties of surface waveguides on grounded substrates can be altered by integrating special periodic structures with resonance properties. Such structures are known as electromagnetic bandgap (EBG) structures and prohibit the propagation of surface waves within a bandgap region. A popular geometry is the mushroom-type EBG structure proposed by Sievenpiper [65]. This structure has been thoroughly studied in literature and comprises square metallic patches, which are shorted to the ground plane by vias. Thus, it can also be manufactured using the same low cost PCB technologies as the planar antenna. The bandgap region is determined by the resonance frequency of the EBG cell elements. The operation of the EBG is explained by considering its cross section depicted in Figure 58.

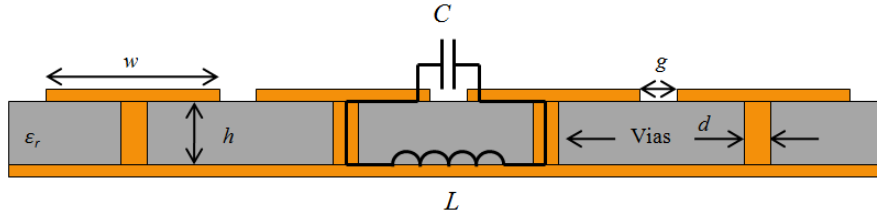


**Figure 58: Physical and electrical concept of the mushroom-type EBG structure**

The strong magnetic field of the surface wave mode, propagating in the plane of the substrate, excites a current which flows on the patches, through the shorting vias and over the ground plane. This forms a current loop between two patches. The current loop is closed by the displacement current through the gap of the patches. Based on this, an equivalent circuit model can be extracted. The lumped elements are roughly approximated using the closed form expressions given in [102]. The inductance  $L$  depends on the area enclosed by the current loop. The height of the substrate is  $h$ . This results in a sheet inductance of:

$$L = \mu_0 h \quad (118)$$

The capacitance  $C$  depends on the EBG cell gap spacing  $g$  and the EBG patch width  $w$ :



$$C = \frac{w}{\pi} \varepsilon_0 (1 + \varepsilon_r) \cosh^{-1} \left( \frac{2w + g}{g} \right) \quad (119)$$

The relative dielectric constant of the substrate is given by  $\varepsilon_r$ . The resonance frequency  $f$  of the EBG cells can be roughly estimated by neglecting edge effects and fringing fields.

$$f = \frac{1}{2\pi} \frac{1}{\sqrt{LC}} \quad (120)$$

Roughly around the resonance frequency of the EBG cells, the secondary fields, which are excited on the EBG, counter the fields of the surface wave mode propagating on the grounded substrate ideally causing a cancellation of the total fields. Thus, the propagation of the surface wave is ideally completely prohibited. From a circuit model point of view, the EBG cells behave like a distributed parallel LC filter.

The characteristics of an EBG cell are characterized with a dispersion diagram for the surface wave mode. In [103], a detailed overview of creating dispersion diagrams for EBG structures is given. Based on this approach, a dispersion diagram for the above mushroom-type EBG was created using full-wave simulations.

Figure 59 shows the Brillouin zone of a 2D periodic structure with two planes of symmetry. In the case that the unit cell is symmetrical with regards to both  $xz$  and  $yz$  planes, only combinations of orthogonal wave numbers  $k_x$  and  $k_y$  need to be considered. In this case, it is sufficient to only consider one characteristic triangle in the Brillouin zone [104] corresponding to one eighth of the entire zone.

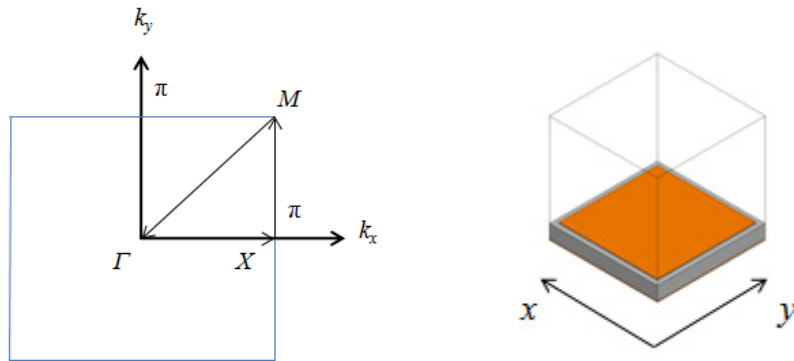


**Figure 59: Illustration of the Brillouin zone (left) for an EBG unit cell (right).**

The corresponding wave numbers of the three paths are defined in the following. For simplicity, the unit cell side lengths are normalized in this representation.

- $\Gamma$  to  $X$ :  $k_x=0$  deg/m to  $180$  deg/m,  $k_y=0$  deg/m.
- $X$  to  $M$ :  $k_x=180$  deg/m,  $k_y=0$  deg/m to  $180$  deg/m.
- $M$  to  $\Gamma$ :  $k_x=180$  deg/m to  $0$  deg/m,  $k_y=180$  deg/m to  $0$  deg/m.

The EBG unit cell was simulated using the eigenmode solver of Ansys HFSS™ (see Appendix 1). Conductor and dielectric loss are considered by assigning a finite conductivity to the copper and a dielectric loss tangent to the substrate. Radiation losses (leaky waves) are also considered. For this purpose, a PML boundary is allocated above the EBG. Master and slave boundaries are set on the outer faces of the air box in the  $xz$  and  $yz$  planes. The phases of the modes are varied according to the defined regions of the triangle. These are simulated for the lowest order  $TM_0$  surface wave mode.

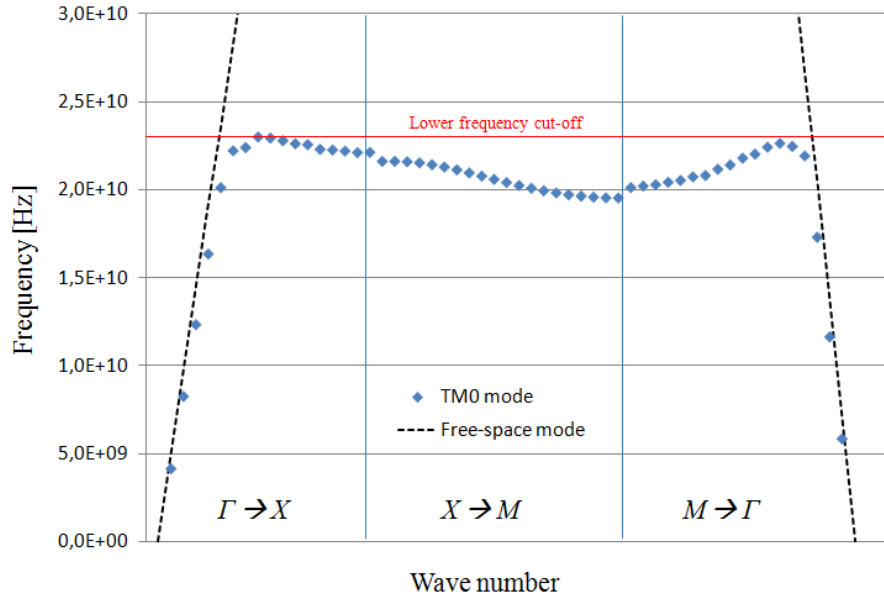


**Figure 60: Full dispersion diagram for the space and surface wave modes of the EBG cell.**

Figure 60 shows the results of the complete dispersion diagram. In addition to the surface wave mode, the space wave mode is also shown. It is evaluated by considering the wave numbers in vacuum.

$$k_x = k_y = \frac{2\pi f}{c_0} \quad (121)$$

At low frequencies, the dispersion of the EBG is similar to that of the space wave mode. At approximately 20 GHz, the resonance properties of the EBG become apparent. It is also observed that the EBG exhibits a negative dispersion for the  $TM_0$  mode propagation. The lower frequency of the  $TM_0$  mode bandgap can readily be determined. Above approximately 23 GHz, the dispersion diagram shows no solution for the  $TM_0$  mode. Determining the upper frequency bandgap involves determining the dispersion diagram of the next higher order  $TE_1$  mode. The point of intersection of the  $TE_1$  mode with the space wave mode in the dispersion diagram represents the upper bandgap frequency. However, determining this point of intersection with sufficient accuracy involves obtaining accurate eigenvalue solutions for the  $TE_1$  mode.

Although the dispersion diagram allows an in-depth analysis of the EBG structure with respect to surface wave suppression properties, a major drawback results from the fact that the EBG is assumed to extend to infinity in the lateral plane. Thus, the edge effects of a finite size EBG are not considered.

In a next step, the analyzed EBG was integrated between the patch antennas (reference structure). Altogether 15 EBG cells were chosen comprising three rows with five elements each. Since the EBG has finite lateral dimensions, the edge effects at the ends of the EBG structure and their influence on the suppression and tuning of the EBG need to be considered. Therefore, a complete full-wave simulation model was set up, as depicted in Figure 61.

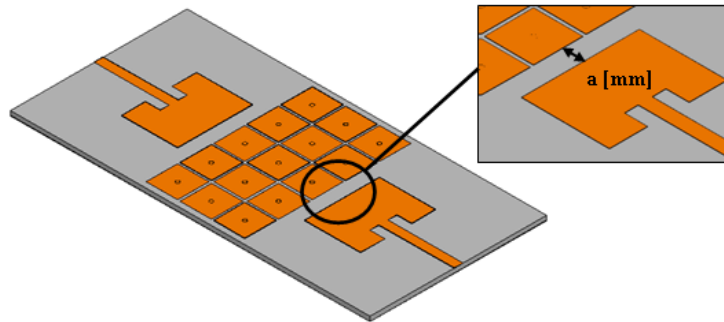


**Figure 61: Model of E-plane patch antennas with integrated EBG for the suppression of coupling.**

To determine the values of the EBG for suppression of surface waves at 24 GHz, the analytical expressions (118)-(120) were used as a first approximation and fine tuned with full-

wave simulations. In order to obtain high capacitance between the cells and, hence, ensure minimum EBG cell dimensions at 24 GHz, a small value of the cell gap  $g$  was chosen such that manufacturing with PCB technologies is still possible. The parameters  $w=1.85$  mm and  $d=300$   $\mu\text{m}$  were designed with the given  $\epsilon_r=3.75$ ,  $t=17.5$   $\mu\text{m}$  and  $h=250$   $\mu\text{m}$  values of the substrate technology.

In order to achieve high integration densities, it is desirable to place the antenna close to the EBG. Therefore, the influence of the edge-to-edge distance  $a$  is studied on the suppression properties of the EBG for the E-plane coupling case where the surface wave is excited and propagates. Figure 62 shows the simulation results.

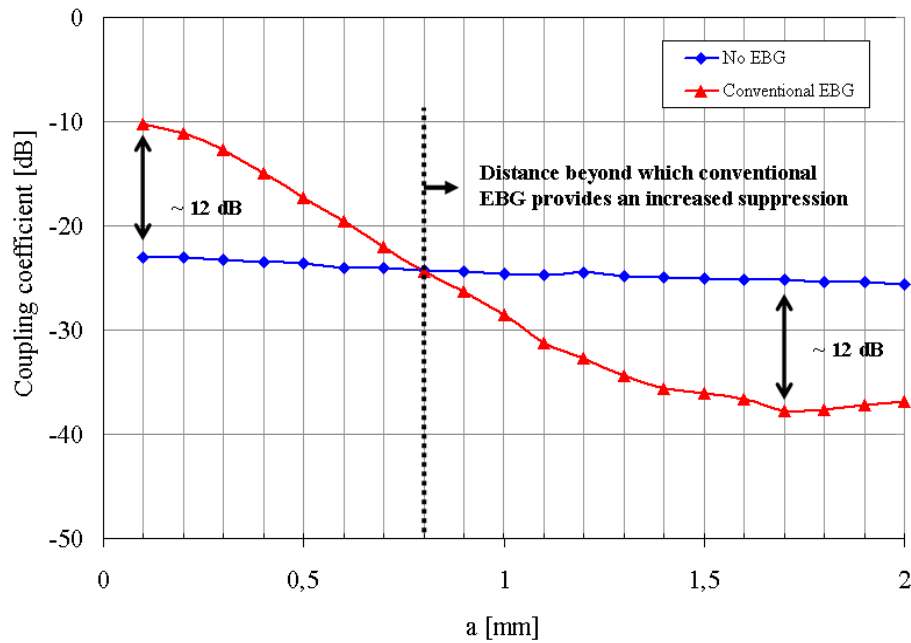


**Figure 62: Simulation results of the coupling coefficient  $S_{21}$  between the E-plane coupled patch antennas in dependency of the separation distance  $a$ .**

The edge-to-edge separation distance between the antenna elements and the EBG is  $a=2$  mm ( $0.16 \lambda$ ). At this distance, the electromagnetic interactions between the antenna's reactive near-field and the EBG is negligible i.e., the antennas are not significantly detuned by the presence of the EBG. The EBG is placed outside of the electromagnetic antenna boundary.

The coupling between the patch antennas with the EBG is -37 dB with a separation distance  $a=2$  mm. As is observed, the EBG improves the suppression between the patch antennas by 12 dB compared to the case without the EBG. However, the plots also show that below a critical separation distance, in this case  $a=0.8$  mm ( $0.06 \lambda$ ), the EBG causes a degradation of

the coupling suppression between the patch antennas. The electromagnetic interactions at the antenna near-field cause a shift in impedance parameters of the EBG.

However, in order to allow a high integration density, the EBG may need to be placed closer than the critical distance to the antenna i.e., inside the electromagnetic antenna boundary. It is shown next that the EBG can be tuned to operate with high suppression when it is placed closer to the antenna.

To compensate the additional capacitive loading of the patch antenna, the EBG patch size is increased slightly. By this means, the inductance  $L$  in (118) remains constant and the capacitance  $C$  in (119) is increased slightly. With the aid of numerical simulations, the EBG patch dimensions were optimized for suppression at a distance of  $a=400\text{ }\mu\text{m}$ . The square EBG patch size is altered from  $w=1.85\text{ mm}$  to  $w=2.05\text{ mm}$ . The gap  $g$  between the patches remains at  $150\text{ }\mu\text{m}$ . Figure 63 shows the simulation results of the coupling coefficients as well as a comparison with the conventional EBG structure. As is observed, the suppression of the optimized EBG is substantially improved compared to the conventional EBG for separation distances  $a < 1\text{ mm}$ . The suppression of the optimized EBG has a maximum at  $a=400\text{ }\mu\text{m}$  where the suppression is 27 dB higher compared to the conventional EBG. However, for larger distances, the conventional EBG performs better. The optimized EBG only operates well close to the antenna, where it is capacitively coupled to the reactive near-field.

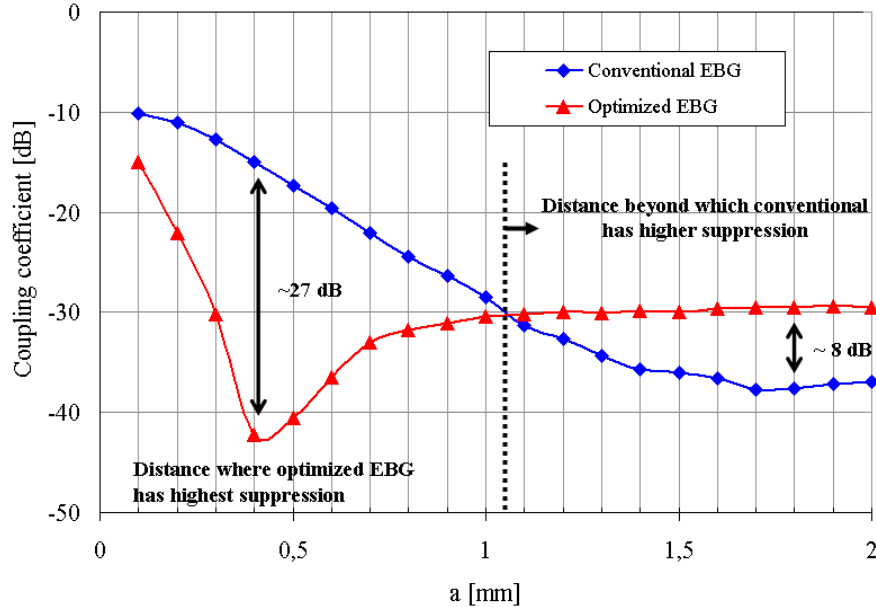


**Figure 63: Simulation results of the coupling coefficient  $S_{21}$  between the E-plane coupled patch antennas in dependency of the separation distance  $a$ .**

Ideally, the EBG structure has no influence on the antenna parameters. However, since the optimized EBG is placed at  $a=400\text{ }\mu\text{m}$  within the electromagnetic antenna boundary, changes in the antenna parameters also need to be considered. This is shown further on in Section 4.1.3.

#### 4.1.2 Planar Surface Wave Reduced (SWR) Antenna

In order to reduce the high E-plane coupling between the patch antennas, it is also possible to design the antenna in such a way that it does not excite surface waves or only reduced surface wave power. Such antenna configurations are referred to as surface wave reduced (SWR) antennas. In this section, the results of the implementation of a SWR patch antenna are presented, and the shielding effectiveness as well as the required board space are characterized.

A commonly used planar geometry for SWR antennas is a circular patch. The general approach of analysis is to introduce an equivalent magnetic current density (37) along the outer contour of the patch resonator. The magnetic current density is then regarded as the source, and the fields are calculated. Finally, the critical radius of the circular patch is determined such that the  $TM_0$  surface wave mode is not excited. The smallest patch radius  $r_p$  with respect to the surface wave phase constant  $\beta_{TM_0}$  to obtain this condition was derived by Jackson *et al.* [82].

$$\beta_{TM_0} r_p \approx 1.84 \quad (122)$$

Based on this analysis and on the theory presented by Jackson *et al.*, a circular patch antenna with critical radius was designed for operation at 24 GHz.

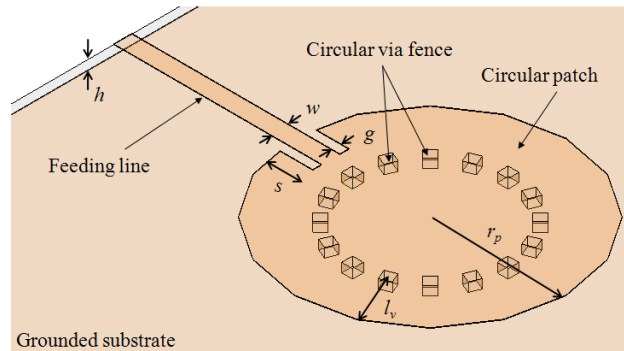
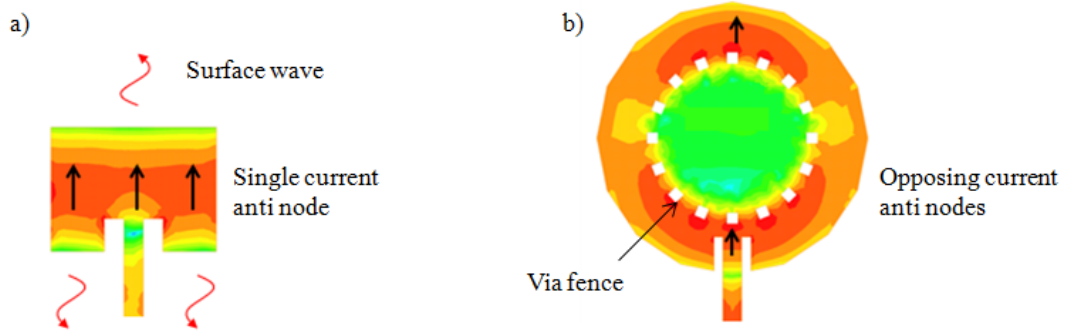


Figure 64: Configuration and dimensions of the designed SWR patch antenna.

The circular patch antenna design is based on the design of an annular ring antenna [105]. An inset feed is employed to excite the antenna. Figure 64 shows the dimensions of the SWR patch antenna, which was designed on the same substrate configuration as the other antenna designs in this work (see Section 2.3).

The radius of the SWR patch resonator  $r_p=3.75$  mm. The inset feed for impedance matching is positioned at the distance  $s=0.9$  mm from the outer edge of the patch. The gap  $g=0.25$  mm, and the impedance controlled microstrip line has the width  $w=0.5$  mm. The circular via fence is placed at the distance  $l_v=1.5$  mm from the outer perimeter of the patch and is used to tune the resonance frequency. The standing wave is formed between the outer open circuit of the patch and the inner shorted circular via fence enforcing a  $\lambda_{eff}/4$  resonance. Therefore,  $l_v$  is a sensitive and technologically critical parameter for the resonance frequency of the antenna.

Figure 65 (b) shows the SWR antenna and its excited current distribution at 24 GHz. The current distribution on the conventional rectangular patch antenna is shown in Figure 65 (a). In comparison, the conventional patch excited with the lowest order TM mode only has one current anti node at the center.



**Figure 65: Surface current distribution: on the excited (a) conventional patch antenna; and on the (b) SWR antenna. The arrows indicate the direction of the current anti nodes.**

The current on the SWR antenna flows primarily on the via fence. At the center of the patch, only small leakage currents are observed. The outer ring between the via fence and the radiating apertures can be described as a shorted parallel plate waveguide excited with its first higher order mode (enforced by the shorting wall). The current anti nodes caused by the resonance on the circular ring are both  $x$  directed. However, since the separation distance of the two current anti nodes is approximately one half wavelength at 24 GHz, the surface waves launched in positive and negative  $x$  direction are eliminated by destructive interference.

Figure 66 shows a comparison of the simulated and measured reflection coefficient of the SWR antenna. The fabrication process is highlighted in Appendix 4.

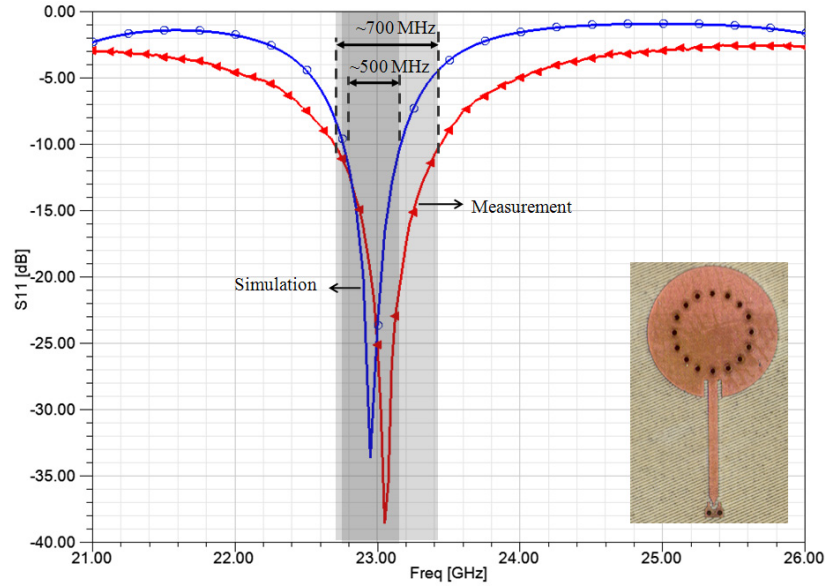


**Figure 66: Measurement results of the reflection coefficient  $S_{11}$  of the SWR patch antenna and comparison to full-wave simulation.**

It is observed that the antenna resonates at about 23 GHz with an impedance bandwidth of 700 MHz. The measured resonance frequency is slightly lower than the envisaged resonance of 24 GHz during the design of the antenna. This shift is due to technological fluctuations of the PCB prototype. The resonance frequency of the SWR antenna is particularly sensitive to the positions of the shorting vias. Therefore, the simulations were adapted slightly after fabrication and measurement. The simulated bandwidth is also slightly lower with 500 MHz. The additional losses are a result of the via fence, which is fabricated using a conductive polymer paste yielding lower conductivity values compared to conventional copper vias. The additional losses reduce the antenna Q factor resulting in an increased impedance bandwidth. Next, the electromagnetic antenna boundary of the SWR antenna is also evaluated. Figure 67 shows the simulated reactive power density on the ground plane of the SWR antenna. The same approach as already implemented in Section 2.3.5 is used to deduce the electromagnetic antenna boundary.

The width  $w=2r_p$  and length  $l=2r_p$  are introduced for better comparison with the conventional patch, slot and dipole antennas. The threshold value of the SWR antenna was calculated using (93). The SWR antenna parameters including the radiation efficiency  $\eta=67\%$  were computed resulting in a threshold value of  $13.5 \text{ mW/mm}^2$ .



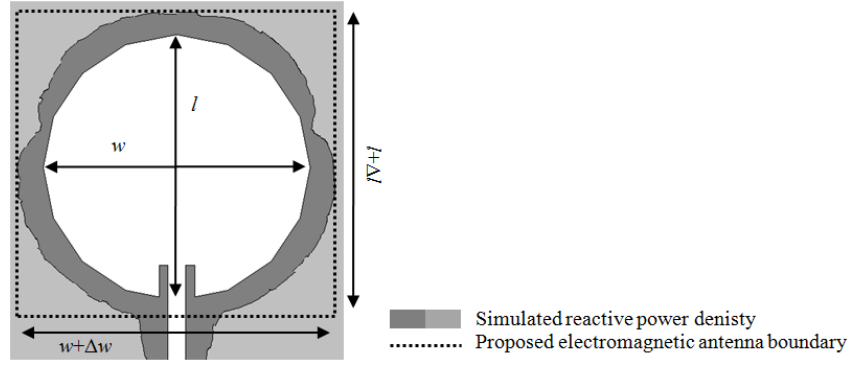


**Figure 67: Simulation of the reactive power density on the ground plane of the SWR patch antenna.**

The same procedure for estimating the electromagnetic size of the antenna, given by  $l+\Delta l$  and  $w+\Delta w$ , is applied. Table 6 shows the results in comparison to the conventional patch antenna.

Antenna	Dimensions					
	Physical size			Electrical size		
	$l$ [mm]	$w$ [mm]	Area [mm <sup>2</sup> ]	$l+\Delta l$ [mm]	$w+\Delta w$ [mm]	Area [mm <sup>2</sup> ]
Conventional patch	3.175	4.25	13.5	4.6	6.5	29.9
SWR patch	7.5	7.5	56.3	8.8	9	79.2

**Table 6: Deduced electromagnetic antenna boundary values of the SWR patch antenna and comparison to the conventional patch antenna.**

The physical and electromagnetic dimensions of the SWR antenna are significantly larger than the patch antenna. The SWR antenna requires more board space.

The shielding effectiveness of the SWR antenna is characterized next by considering the E-plane coupling and comparing the results to the results of the conventional patch antennas in Figure 56.

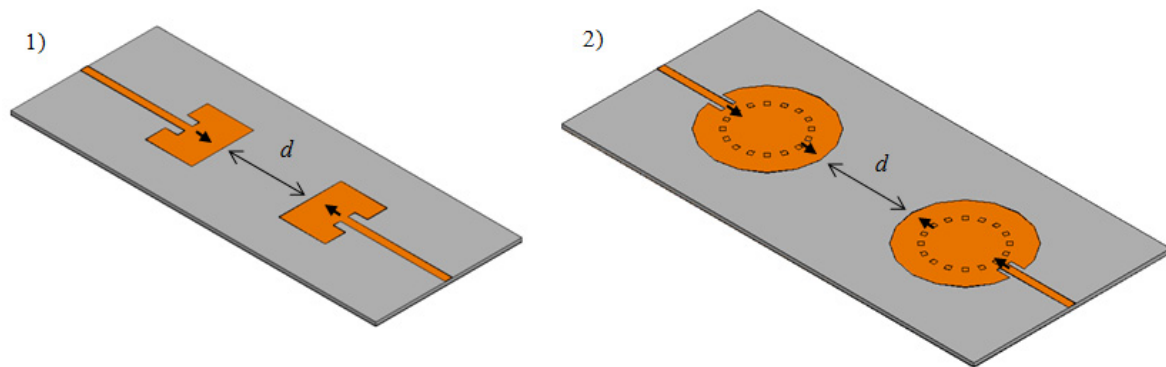


**Figure 68: 3D simulation models of the coupled antennas: (1) conventional patch antennas; and (2) SWR patch antennas.**

Figure 68 shows the 3D simulation models that were used for the shielding effectiveness characterization. Figure 69 shows the simulation results of the E-plane coupling for different separation distances  $d$ .

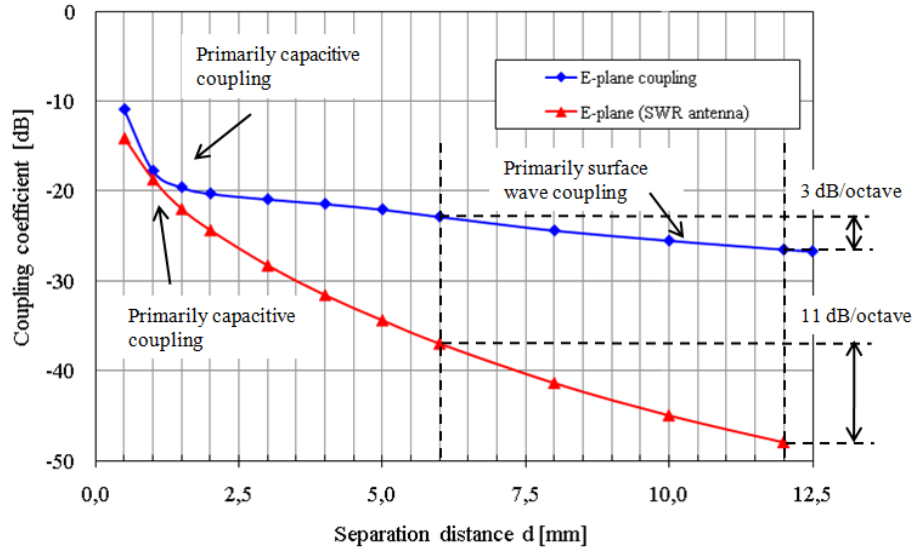


**Figure 69: Simulation results of the coupling coefficient  $S_{21}$  between two conventional patch antennas and two SWR patch antennas.**

In the near-field of both the conventional and SWR antenna, capacitive coupling at the radiating apertures dominates, and the coupling decay with distance is similar up to a distance of 1 mm. This shows that the SWR antenna is not effective in reducing capacitive near-field coupling. This is also approximately the distance where the electromagnetic antenna boundary exists, indicating that the antennas couple power through the reactive near-field. Beyond this distance, the surface wave coupling dominates for the conventional patch antenna. In the case of the SWR antenna, neither the space wave nor the surface wave coupling dominates. It is observed that the coupling decays with 11 dB/octave distance, which is faster than the space and surface wave decay rates with distance. Thus, the SWR patch antenna effectively reduces the E-plane coupling by suppressing surface wave and lateral space wave excitation in the E-plane.

#### 4.1.3 Comparison of Configurations and Measurement Results

The shielding effectiveness of the EBG structure and the SWR antenna were verified with measurements. For this purpose, test structures for measuring the coupling were manufactured. Figure 70 shows photos of the test structures. The geometrical and material

properties of the structures correspond to those of the simulation models in the previous sections.

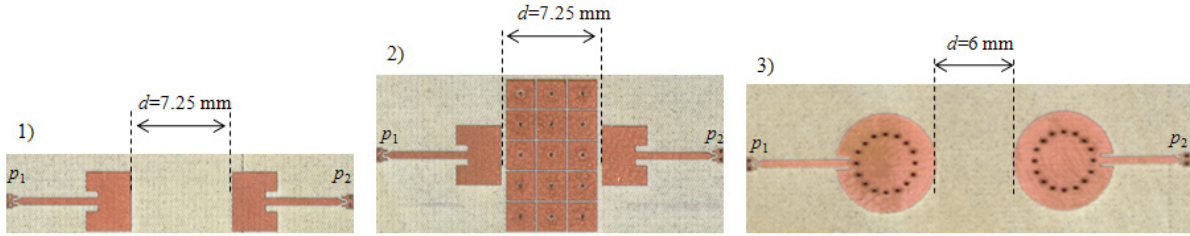


**Figure 70: Photos of the test structures used to measure the coupling: (1) conventional patch antennas; (2) patch antennas with EBG structure; and (3) SWR patch antennas.**

It is noted that the separation distance  $d$  between the patch antennas of 7.25 mm is slightly larger than between the SWR antennas of 6 mm. This was necessary to integrate the EBG structure between the patch antennas. The reflection coefficients of the antennas  $S_{11}$  and transmission coefficients between the antennas  $S_{21}$  were measured for all test structures. Since the structures are symmetrical, the coefficients  $S_{22}=S_{11}$  and  $S_{12}=S_{21}$ . Figure 71 shows the measurement results.

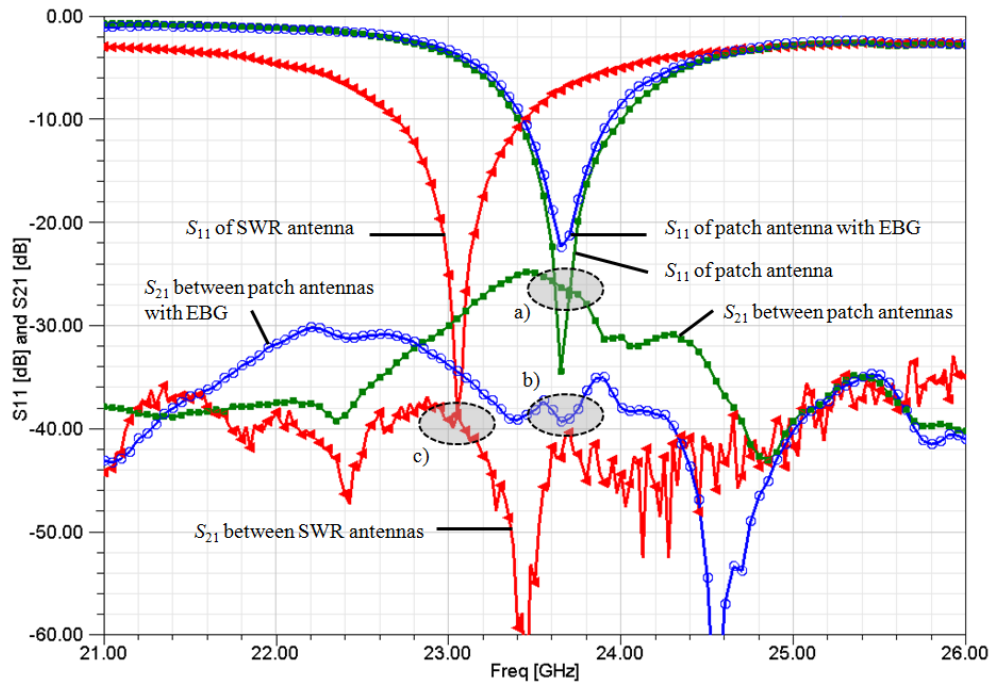


**Figure 71: Comparison of coupling measurement results: (a) conventional patch antennas; (b) patch antennas with EBG structure; and (c) SWR patch antennas.**

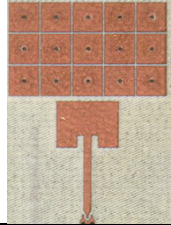
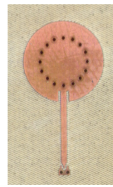
The coupling is evaluated within regions marked (a), (b) and (c) in the plot. These represent the frequency ranges around the resonance frequencies of the antennas. Note that the resonance frequency of the SWR antenna is approximately 23 GHz, slightly lower than the envisaged 24 GHz. Table 7 summarized the results.

	Patch antennas (Region a)	Patch antennas with EBG (Region b)	SWR antennas (Region c)
Coupling [dB]	-25	-40	-37

**Table 7: Evaluated coupling values of the three configurations.**

The coupling between the patch antennas is -25 dB. This matches well with the simulation results in Figure 57 and Figure 62. At the resonance frequency of the patch antenna, the EBG provides coupling of -40 dB. Therefore, the shielding is improved by 15 dB. In comparison, the simulation results (see Figure 63) predicted a coupling of -43 dB, which is only slightly lower than the measured coupling.

The resonance frequency of the patch antennas is slightly influenced by the presence of the EBG. The impedance bandwidth is decreased slightly. Furthermore, at antenna resonance,  $S_{11}$  of the patch antenna is reduced to -20 dB. This results from the presence of the EBG inside the electromagnetic antenna boundary. The EBG was, however, optimized to reside at the near-field of the patch antenna for direct coupling through the reactive near-field. Concerning the SWR antennas, it is observed that the coupling is lower than -37 dB. The measurement results match well with the simulation results in Figure 69 at a distance of 6 mm.

Configuration	EBG integration	SWR antenna
		
Suppression	15 dB	16 dB
Occupied board area	$13.5 \text{ mm}^2 + 70 \text{ mm}^2$	$13.5 \text{ mm}^2 \rightarrow 42 \text{ mm}^2$
Percentage area increase	520 %	147 %

**Table 8: Comparison of shielding effectiveness and required board space between EBG structure and SWR patch antenna.**

Finally, a comparison of the shielding effectiveness of both shielding configurations is conducted. For this purpose, the coupling between the antennas is evaluated at a fixed

distance. The separation distance  $d$  between the patch antennas with integrated and optimized mushroom-type EBG structure of 7.25 mm is selected. In the case of the SWR antenna, the reduction of the coupling between the SWR antennas at a distance of  $d=7.25$  mm is evaluated. The results are summarized in Table 8.

The additional space, required by the EBG structure, is calculated by evaluating the total area of the EBG. Approximately  $70 \text{ mm}^2$  of additional board space is required. The SWR antenna occupies more than three times the area compared to the conventional patch antenna. In total, however, the SWR antenna occupies less board space and at the same time provides higher shielding effectiveness than the EBG structure.

## 4.2 Coupling between SWR Antenna and Transmission Lines

The SWR antenna has improved performance compared to the EBG structure with regards to shielding effectiveness and required board space. In order to illustrate its feasibility for system integration with transmission lines, the coupling to the same transmission line routing path as already evaluated in Section 3.3.2 was simulated with the SWR patch antenna. Figure 72 shows the configuration with the two transmission line routing paths.

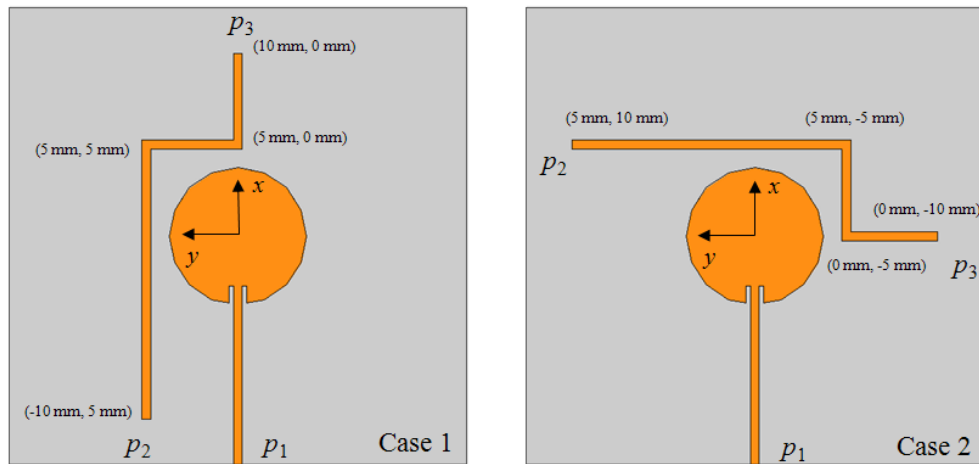


**Figure 72: Overview of the SWR patch antenna with the two microstrip transmission line routing cases with multiple bends. The  $x$ - $y$  coordinates specify the absolute routing path of the transmission line.**

Note that the transmission lines are routed outside the electromagnetic antenna boundary of the SWR antenna (see Figure 67). Also note that the transmission lines are closer to the SWR antenna in comparison to the patch antenna and the transmission lines in Figure 51. The SWR antenna occupies 147 % more board space than the conventional patch antenna.

Since the transmission lines are routed outside the electromagnetic antenna boundary, the weak coupling assumption is valid. The microstrip transmission line has a characteristic impedance of  $50\ \Omega$  and is matched terminated at the ports  $p_2$  and  $p_3$ . The coupling is also reciprocal (see Section 2.2.1.3). The coupling terms  $S_{21}$  and  $S_{31}$  are computed using full-wave simulations. Table 9 shows the results and a comparison with the conventional patch antenna.

Case	Conventional patch antenna		SWR patch antenna		Improvement [dB]	
	$S_{12}$ [dB]	$S_{13}$ [dB]	$S_{12}$ [dB]	$S_{13}$ [dB]	$\Delta S_{12}$ [dB]	$\Delta S_{13}$ [dB]
1	-32	-26	-43	-31	11	5
2	-30	-32	-30	-30	0	-2

**Table 9: Comparison of simulated coupling to the transmission lines for cases 1 and 2.**

The coupling in case 1 is reduced by 11 dB to  $p_2$  and 5 dB to  $p_3$  compared to the conventional patch antenna, respectively. For case 2, the coupling to  $p_2$  remains the same and is increased slightly to  $p_3$ , respectively. This is mainly attributed to the closer transmission line spacing. Also note that the current anti nodes on the SWR antenna are not located at the origin of the coordinate system but shifted slightly in positive and negative  $x$  direction (see Figure 65). Therefore, the current anti nodes are even closer to the transmission line for case 2. Nevertheless, the SWR patch antenna does effectively reduce coupling in case 1. Therefore, its feasibility for integration with transmission lines at board level is concluded.

### 4.3 Summary

Two planar shielding configurations, suitable for low cost PCB applications, were designed, implemented and characterized with regards to shielding effectiveness and required board space. Only two metallization layers are required to manufacture the structures. The SWR antenna obtains a higher shielding effectiveness while simultaneously occupying less board space than the EBG structure. It was also shown that the SWR antenna is suitable for integration with transmission lines, lowering the coupling to neighboring traces. As a result, the SWR antenna design is considered an appropriate technique for reducing undesired coupling and efficiently utilizing available board space.

## 5 Design Recommendations, Conclusions and Outlook

This work focused on three essential aspects for facilitating efficient board level planar antenna integration at (quasi) millimeter-wave frequencies:

- An approach for determining the electromagnetic antenna boundary for planar antennas was developed, defining the block out region around the antenna where no board components should be placed when the antenna is integrated at board level.
- A method for calculating coupling to transmission lines routed outside the electromagnetic antenna boundary on the same substrate was developed, allowing efficient evaluation of coupling in the post process to 3D full-wave electromagnetic field simulations.
- Two planar shielding configurations, comprising an EBG structure and a SWR antenna suitable for integration on low cost PCBs, were quantified. It was shown that the SWR antenna reduces coupling while efficiently utilizing available board space.

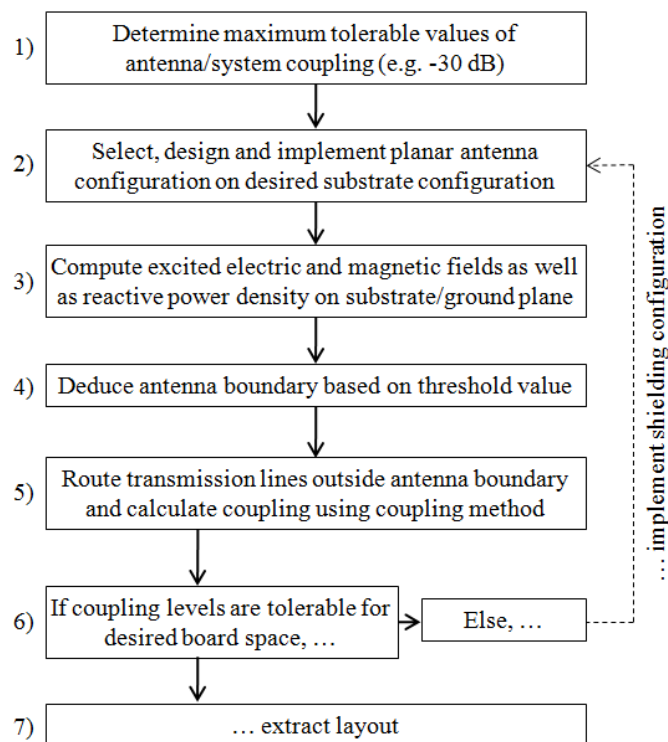


**Figure 73: Overview of an optimized design process for planar antenna integration including the approaches, methods and results proposed in this work.**

The proposed approaches, methods and results significantly reduce the required full-wave simulation efforts as well as trial-and-error iterations during the design process of compact and low cost wireless modules.

Figure 73 shows an overview of an optimized design process for planar antenna integration, considering electromagnetic interactions at board level with the aim of minimizing these.

- 1) The maximum tolerable coupling values between the planar antenna and neighboring board components are estimated prior to integration. Note that this coupling is primarily governed by the coupling between the antenna and transmission lines routed on the same substrate. Parameters such as the transmit power, receiver sensitivity, link budget and required signal-to-noise ratio also need to be considered for this estimation.
- 2) The planar antenna configuration is selected and implemented on the substrate configuration. The choice of antenna type is mainly influenced by the desired radiation characteristics (above/below of or in lateral direction to the ground plane), the required impedance bandwidth as well as on the available ground plane size and topology. Full-wave simulations are required in the design and optimization phase of the planar antenna. The considered 24 GHz planar antennas in this work have the following characteristics:
  - a. The patch antenna has 6.5 dBi gain in the direction normal to the ground plane, an impedance bandwidth of 500 MHz (2 %) and a radiation efficiency of 80 %. The physical dimensions are 4.25 mm x 3.175 mm ( $0.34 \lambda \times 0.25 \lambda$ ).
  - b. The slot antenna has 4.5 dBi gain in normal direction above and below the ground plane, an impedance bandwidth of 1 GHz (4.2 %) and a radiation efficiency of 90 %. The physical dimensions are 4.5 mm x 0.15 mm ( $0.36 \lambda \times 0.01 \lambda$ ).
  - c. The dipole antenna has 5 dBi gain in lateral direction to the ground plane, an impedance bandwidth of 9.5 GHz (39.6 %) and a radiation efficiency of 94 %. The physical dimensions are 5.95 mm x 0.75 mm ( $0.47 \lambda \times 0.06 \lambda$ ). Note that a separation distance between the dipole and the ground plane is required. Therefore, the total dipole width from the ground plane is 2.1 mm ( $0.17 \lambda$ ).



- 3) In the next step, the electric and magnetic fields on the substrate are computed once for the optimized antenna design. These are used for the determination of the electromagnetic antenna boundary and for calculating the coupling to neighboring transmission lines.
- 4) Based on this field distribution, the electromagnetic antenna boundary is deduced by evaluating the reactive power density and its threshold value. The threshold value is calculated using the resonance frequency, input power (with which the antenna fields were computed), efficiency and return loss of the antenna. Regions around the antenna with lower reactive power densities as specified by the threshold value are considered to be outside the electromagnetic antenna boundary. Board components placed there have negligible influence on the antenna parameters.

The considered planar antennas in this work have the following electromagnetic sizes as defined by their electromagnetic antenna boundaries:

- a. Patch antenna: 6.5 mm x 4.6 mm ( $0.52 \lambda \times 0.37 \lambda$ )
- b. Slot antenna: 5.5 mm x 2.7 mm ( $0.44 \lambda \times 0.22 \lambda$ )
- c. Dipole antenna (including the required separation distance from the ground plane):  
9 mm x 3.75 mm ( $0.72 \lambda \times 0.3 \lambda$ )

The ground plane sizes of the antennas should always be kept *larger* than the electromagnetic antenna boundary when the antenna is integrated. The ground plane should also remain unperturbed inside the electromagnetic boundary.

- 5) Next, the coupling between the planar antenna and different transmission line routing paths outside the electromagnetic antenna boundary can be evaluated to assist in board component placement and signal interconnection. The coupling model allows fast and efficient evaluation of coupling. Some design guidelines are summarized in the following:
  - a. Coupling from planar antennas to impedance controlled transmission lines and vice versa is typically maximal around the resonance frequencies of the antenna.

- b. Routing transmission lines outside the electromagnetic antenna boundary ensures that the antenna characteristics remain unperturbed.
  - c. Coupling values above -30 dB need to be considered, if transmission line segments are routed close to the antenna at distances smaller than  $\lambda/4$ .
  - d. Individual transmission line segments should be routed orthogonally to the antenna mode currents when placed close to the antenna for distances between up to  $\lambda/2$ . In general, the transmission line segments should also not be routed orthogonally to the computed magnetic field on the ground plane in order to reduce the magnitude of the excited equivalent sources along the transmission line.
  - e. The transmission line length has a less significant influence on the magnitude of the coupling than the separation distance of the transmission line from the antenna. To minimize coupling, a *long* transmission should rather be routed *far away* from the antenna.
  - f. The dipole antenna, being a differential configuration, inherently has the lowest coupling values to transmission lines <-45 dB for the cases considered in this work.
- 6) If the coupling values exceed the tolerable levels as governed by the application, a planar shielding configuration may need to be implemented. The additional required board space of the two shielding configurations considered in this work are summarized as follows:
- a. The mushroom-type EBG structure comprising 15 elements needs to be integrated on the substrate beside the antenna where the surface waves are launched into the substrate. It occupies an area of 10.85 mm x 6.45 mm ( $0.87 \lambda \times 0.52 \lambda$ ). Note that the EBG was optimized to operate in the near-field of the patch antenna.
  - b. The SWR patch antenna has 7.5 dBi gain in the direction normal to the ground plane, an impedance bandwidth of 500 MHz (2 %) and a radiation efficiency of 67 %. The circular patch has a diameter of 7.5 mm ( $0.6 \lambda$ ). In comparison to the

conventional patch antenna, it occupies 147 % more board space. The electromagnetic antenna boundary is located at 8.8 mm x 9 mm ( $0.7 \lambda \times 0.72 \lambda$ ).

- 7) If the coupling values are within tolerable limits for the desired board space, the layout of the antenna and favorable transmission line routing paths are extracted.

The configurations studied throughout this work were designed and implemented primarily for the 24 GHz frequency range where an ISM band is available. The implemented patch, slot, dipole and SWR antennas were manufactured using low cost PCB technologies to save cost and also show the feasibility of employing PCBs for the realization of planar antennas at these high frequencies. Nevertheless, the developed concepts are applicable to different substrate technologies, antenna configurations and operating frequencies. In general, substrate materials used for RF applications can be considered linear and isotropic. As a result, the antenna itself is a linear and isotropic system. Therefore, it is geometrically and electrically scalable.

The approach for determining the electromagnetic antenna boundary and the method for calculating coupling to transmission lines could be implemented in software for automated and fast analyses. For this purpose, the field distribution of the designed antenna, the geometrical layout of the antenna and the antenna parameters are imported into the software. The software then deduces the electromagnetic antenna boundary. After this, the user can route different transmission line paths (with specified transmission line parameters) while the software calculates the coupling by field integration in real time. As a result, different routing paths can be evaluated on-the-fly.

It is expected that planar antennas will play a significant role in future compact wireless systems operating at millimeter-wave frequencies. However, the design and integration of antennas remains simulation intensive. Therefore, the development of closed form expressions for the field decay on the substrate and ground plane near patch, slot and dipole antennas would facilitate on-the-fly estimations of the electromagnetic interactions. Furthermore, an implementation of these models even in RF circuit simulators would seem imaginable.

## Appendix 1 - Overview of Full-wave Electromagnetic Field Simulations

Analytical closed form solutions to the wave equation are only available for simple radiating structures. The accurate calculation of fields for more complex radiating structures, such as planar antennas, requires Maxwell's equations to be solved numerically. Commercially available full-wave solvers are based on the finite element method (FEM), finite difference (FD) method, finite integration (FI) method and the method of moments (MoM) in both time and frequency domains [106, 107]. The solver used in this work is based on the FEM in the frequency domain, which is implemented in the commercially available software suite High Frequency Structure Simulator (HFSS™) from Ansys (formerly Ansoft).

The FEM in the frequency domain solves the inhomogeneous vector wave equation for the electric field obtained from substituting the first two of Maxwell's equations (1) and (2) assuming time harmonic fields.

$$\vec{\nabla} \times \left( \frac{1}{\underline{\mu}} \vec{\nabla} \times \vec{E} \right) - j\omega \underline{\epsilon} \vec{E} + j\omega \vec{J} = 0 \quad (123)$$

The material constants can be set complex to account for dielectric and magnetic losses. The matrix equation is derived such that the residual is minimized for the entire domain. For this purpose, (123) is multiplied with a vector weighting function  $\vec{G}_i$  and integrated over the entire domain  $V$  to form the weighted residual equation  $F(\vec{E})$ .

$$F(\vec{E}) = \iiint_V \left( \vec{\nabla} \times \left( \frac{1}{\underline{\mu}} \vec{\nabla} \times \vec{E} \right) - j\omega \underline{\epsilon} \vec{E} + j\omega \vec{J} \right) \vec{G}_i dV = 0 \quad (124)$$

Commonly tetrahedral elements  $T_k$  are used as finite elements to discretize the computation domain because they can be naturally fitted to many geometrical shapes. The interpolating functions  $\vec{N}_n^k$  for each finite element  $T_k$  are chosen so that the electric field inside the element can be described.

$$\vec{E}^k = \sum_{n=1}^6 \vec{N}_n^k \vec{E}_n^k \quad (125)$$

$n$  references the edges of the tetrahedron, which are connected through the four vertices. Two and three tangential components of the electric field are stored at the edges and vertices, respectively, yielding a total of 24 complex values per tetrahedron.

Antennas are considered an open boundary problem. Solving differential equations, however, requires the specification of boundary conditions. Reflection-free truncation of the computation volume is an inevitable measure to reduce the computational cost that would be necessary to simulate an open boundary problem with conventional boundary conditions such as perfect electric conductor (PEC) or perfect magnetic conductor (PMC) boundaries. These enforce surfaces with a reflection coefficient of 100%. They would have to be placed at a large distance away from the radiating structure to ensure that the reflected wave is attenuated enough to not disrupt the field configuration of the simulated structure. Therefore, a perfectly matched boundary condition (PML) is implemented in FEM solvers to provide reflection-free terminations of the computation volume. The complex anisotropic material of the PML is chosen to ensure reflection-free matching of the PML to the free space impedance for all incident angles, polarizations and frequencies [108].

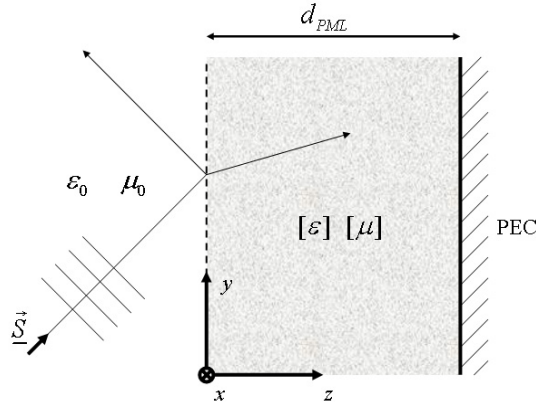


**Figure 74: Concept of PML boundary conditions at the sides of the computational domain to provide low reflections absorbing boundaries.**

A PML configuration is matched to a vacuum with the matching condition:

$$\frac{\mu_0}{\epsilon_0} = \frac{[\mu]}{[\epsilon]} \quad (126)$$

The anisotropy of the permeability and permittivity are described with tensors,  $[\mu]$  and  $[\epsilon]$ , in order to ensure impedance matching and attenuation in  $z$  direction.

## Appendices

$$[\varepsilon] = \varepsilon_0[A] \quad (127)$$

$$[\mu] = \mu_0[A] \quad (128)$$

The tensor entries must obey the following condition:

$$[A] = \begin{pmatrix} s & 0 & 0 \\ 0 & s & 0 \\ 0 & 0 & s^{-1} \end{pmatrix} \quad (129)$$

Furthermore, the entries are complex to ensure attenuation.

$$s = a - jb \quad (130)$$

The imaginary part  $b$  is used to model the electric and magnetic conductivities i.e., the losses, and the real part  $a$  models the phase of the wave propagation in the PML. The PMLs are truncated by either PECs or PMCs and must be thick enough to ensure high attenuation of the reflected wave. It is interesting to note that the imaginary parts of the  $z$  components of the above tensors are negative (different leading sign to the  $x$  and  $y$  components) implying the existence of electric  $-\kappa_e E_z$  and magnetic  $-\kappa_m H_z$  sources within the PML materials.

The radiating structure is surrounded by a 3D box. Additional PML edge elements are introduced at the edges and sides to ensure a complete reflection-free outer box surface. The impedance matching condition (126) is also applied to these elements. Figure 75 shows a possible 2D configuration comprising one corner element.

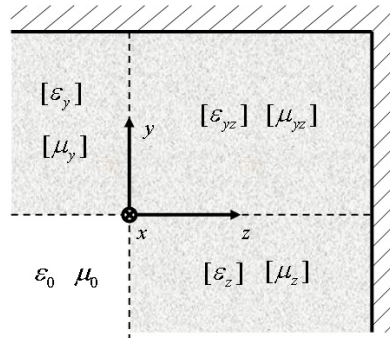


**Figure 75: Concept of PML edge elements at the corner of the box.**

High frequency models are excited by applying an exciting field distribution somewhere inside or on the surface of the computation domain. For practical applications the excitation (source) is a microstrip or coaxial mode on a transmission line. Since these modes are boundary conditions for the source regions, they must be computed before the field distribution inside the computational volume is solved. In the frequency domain, a harmonic time dependency  $\sim e^{j\omega t}$  is assumed. The electric field pattern for mode  $n$  is described as:

$$\vec{E}_n(x, y, z, \omega) = \vec{E}_n(x, y) e^{-\alpha z - j\beta z} \quad (131)$$

The computation of the S-parameters requires an accurate determination of the time averaged power density  $\vec{S}(x, y, z)$  propagating in and out of the port for each desired mode. Hence, a high accuracy of the 2D port field solution  $\vec{E}_n(x, y)$  is vital. The time averaged total complex power  $\underline{P}$  of the mode can be evaluated at the cross section of the port.

$$\underline{P} = \iint \vec{S}(x, y, z = z_0) dx dy \quad (132)$$

Concerning the stability of the computed field solution of the FEM, an adaptive mesh refinement is employed in the field solver. The simulation process is divided into a number of steps. First, a geometrical model of the antenna is set up with the 3D modeler. Material parameters, boundaries and excitations are defined. A solution setup is created with a solution frequency corresponding to the expected resonance frequency of the antenna. Next, a frequency sweep is defined covering the entire frequency range of analysis.

After the simulation is started, the field patterns that exist on the defined cross section of the ports are solved with a 2D full-wave solver. These patterns are used as boundary conditions for the excitation. Then the initial mesh is seeded in the computational domain and the field quantities and S-parameters are computed when the structure is excited with the solution frequency. To obtain a stable solution, the mesh is refined, and the solution is computed again. The maximum change  $\Delta S$  is calculated:

$$\Delta S = \max \left[ \left( S_{ij}^N - S_{ij}^{N-1} \right) \right] \quad (133)$$

From here on, the mesh is refined after each pass until a convergence criterion is met. Once a stable solution is found, the sweep is executed, which extrapolates the field solution at the solution frequency over the desired frequency range.

## Appendix 2 - Examination of Numerical Solution Accuracy

Numerical computation results are approximations of the solutions to the wave equation. Therefore, measurements need to be conducted on manufactured prototypes in order to give a validation of the simulation results. It was observed in the studies in Section 2.2.3 that the dynamic range of the field magnitudes is several orders of magnitudes down to -50 dB from the values of the fields underneath the patch antenna. Furthermore, differences at the order of 1 dB were evaluated. Therefore, the accuracy and stability of the numerical full-wave simulations need to be quantified. This includes the following: (1) quantification of the influence of the automatically generated and refined mesh on the computed fields after each pass; and (2) quantification of the influences of the solver settings (port mode refinement, mesh refinement and absorbing boundary conditions) on the computed fields.

For these quantifications, the simulated magnetic field magnitude in region 1 of the probe fed patch antenna is used (see Figure 20). In all simulations, the adaptive mesh refinement process was used to ensure stability of the computed solution. At least eight passes with a mesh refinement of 30 % were computed. Furthermore, it was ensured that at least three consecutive passes with a maximum change of the S-parameters of 0.01 were computed. A wave port was used as an excitation to feed the antenna from coaxial feeding line.

Figure 76 shows the results of the adaptive mesh refinement i.e., the change of the magnetic field strength at three defined distances ( $0.125 \lambda_0$ ,  $0.425 \lambda_0$  and  $0.725 \lambda_0$  from the patch center). It is observed that after the fourth pass the change in magnetic field strength is less than 0.5 dB indicating that the field solution has converged.

The accuracy of the field pattern on the wave port can be specified within HFSS™. The solver computes the solution for the 2D wave equation of the mode pattern for the electric and magnetic fields independently. Then, the solutions are compared to each other through the mode impedance and an error is determined. The triangular mesh on the port face is refined until this error is below a defined value. For the quantification, two values of the port field refinement are compared: 2 % and 0.01 %.



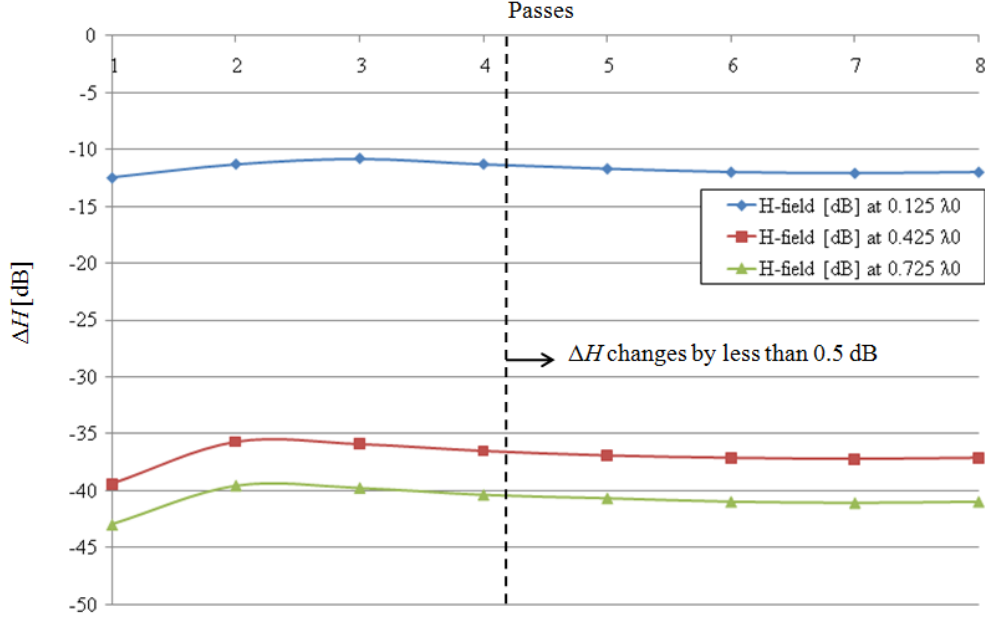


**Figure 76: Change in magnetic field strength on the ground plane of the patch antenna in region 1 in dependency of the computed passes.**

The mesh in the computation domain is generated and refined automatically by HFSS<sup>TM</sup>. However, it is also possible to define a maximum cell size manually. In order to ensure that the spatial field resolution is captured with high accuracy, a maximum mesh cell size of  $0.3 \lambda_0$  was assigned on the substrate and ground plane. First order base functions were used to describe the fields inside the mesh elements. The automatic mesh generated approximately 20000 mesh elements in the entire computation volume including the PML volumes. For the manual mesh a total number of approximately 80000 mesh elements were generated after nine passes with a maximum refinement of 30 %. For the quantification, the results of the automatic mesh are compared to the manual mesh with a maximum cell length of  $0.3 \lambda_0$  on the substrate. Figure 77 shows the (a) automatically generated and refined mesh and (b) manually generated and refined mesh. The results of both solutions are compared.

In all simulations, the PML boundary conditions implemented in HFSS<sup>TM</sup> were used. However, radiation boundary conditions can also be specified. These boundary conditions approximate the fields of the tangential field components on the boundary in a 1 D wave equation. However, unlike PML boundaries, which ideally absorb plane waves at all frequencies, incident angles and polarizations, radiation boundaries only absorb waves with normal incidence effectively. For the quantification, a comparison between PML and radiation boundaries is conducted.

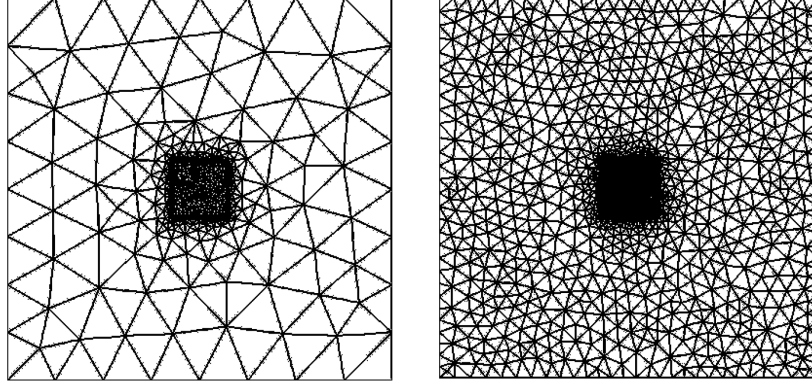


**Figure 77: Comparison of the automatically (left) and manually (right) generated meshes on the substrate.**

The change in field strength, resulting from the different solver settings, are compared to the reference. Figure 78 shows the results. It is observed that a maximum change  $\Delta H$  of less than 0.8 dB is observed for all three variations. Therefore, reproducibility and stability of the computed field solutions is given.

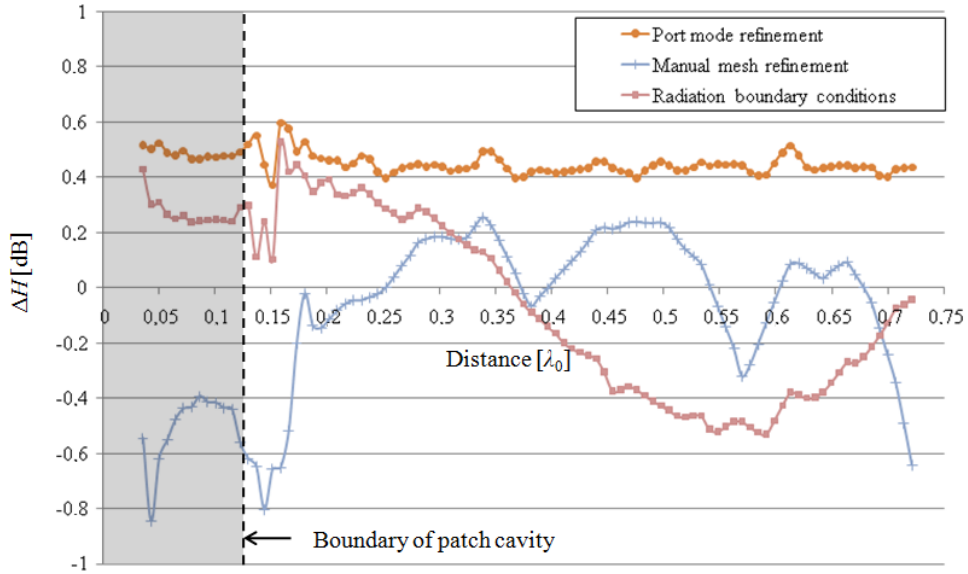


**Figure 78: Change in magnetic field strength on the ground plane of the patch antenna in region 1 for different solver settings.**

Finally, a simple test structure was fabricated and measured. Figure 79 shows a photo of the planar test antenna. The antenna was designed to operate at 4.5 GHz in order to facilitate accurate measurements of the electric field strength on the ground plane using electrically short monopole probes. To ensure comparability with (quasi) millimeter-wave frequencies, a

thick dielectric substrate was used (1.5 mm thick FR4 substrate). It has a similar electrical thickness than the studied patch antenna in Figure 15.

Additionally, seven holes were drilled into the substrate. The holes have equal separation distances from the patch antenna edges. Monopole probes with coaxial connectors were inserted into these holes. The outer conductors of the coaxial connectors were soldered to the ground plane. The monopoles themselves are the extension of the signal conductor of the coaxial connectors.

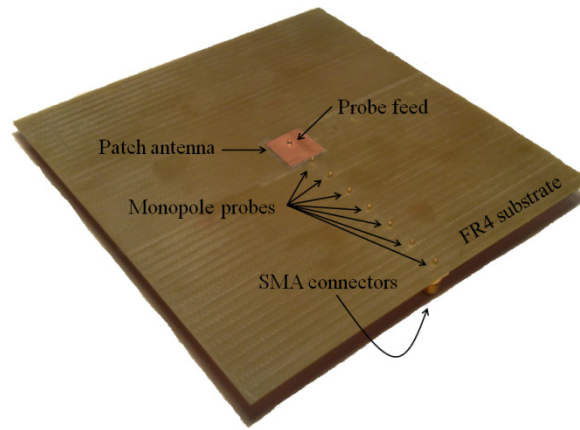


**Figure 79: Manufactured test board with patch antenna and monopole probes to measure the electric field strength at different positions on the substrate.**

The measured resonance frequency is at 4.45 GHz. The -10 dB impedance bandwidth is 140 MHz. Next, the coupling to the monopole probes, inserted into the holes in the grounded substrate, was measured. The results are shown graphically in Figure 80.

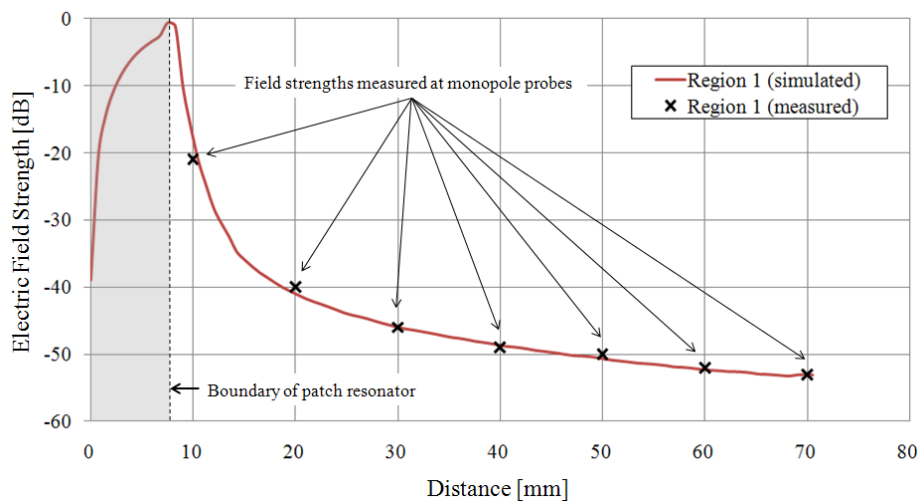


**Figure 80: Measured electric field strengths at the monopole probes on the test board of the patch antenna.**

The magnitude of the coupling coefficient  $S_{21}$  is proportional to the electric field strength at the position of the monopole probes. The measurement is scaled with an offset to match the plot of the normalized electric field strength from the simulations. Altogether, seven transmission measurements were conducted. The simulated and measured results are in good agreement with the decay rate of the electric field.

In summary, the accuracy of the computed field simulations in this work has been quantified. It is concluded that the obtained results are accurate on the order of 1 dB.

### Appendix 3 – Microstrip Transmission Line Parameters

Figure 81 shows the cross section of a microstrip transmission line on the grounded substrate configuration.

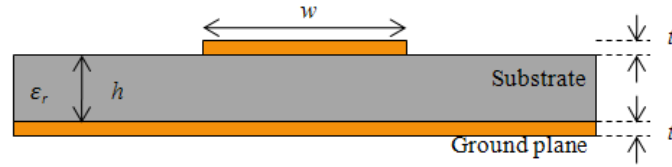


**Figure 81: Configuration of a microstrip line on the grounded substrate configuration with dimensions.**

The microstrip line is used as a feeding line for the antenna configurations and is also a typical transmission line used signal distribution on PCBs. The width  $w$  was designed for a characteristic impedance of  $50 \Omega$ . All the other parameters are fixed and governed by the substrate configuration ( $h=250 \mu\text{m}$ ,  $\epsilon_r=3.75$ ,  $\tan(\delta)=0.006$ ,  $t=17.5 \mu\text{m}$ ). The transmission line parameters, shown in Table 10, were computed using a 2D quasi-static solver.

Line parameters	Computed values
$L'$	295 pH/mm
$C'$	110 fF/mm
$R'$	76 mΩ/mm
$G'$	89 mS/mm
$Z_0$	$51.5 \Omega + j0.1 \Omega$
$\beta$	$0.86 \text{ mm}^{-1}$

**Table 10: Computed transmission line parameters at 24 GHz.**

A detailed overview of the transmission line parameters is given in Section 2.2.1.2. For the target impedance of  $50 \Omega$ ,  $w=500 \mu\text{m}$  was determined. The results show that the losses of the

microstrip line are small. The imaginary part of  $\underline{Z}_0$  is negligible compared to the real part. The transmission line exhibits satisfactory low loss performance ( $\omega L' \gg R'$  and  $\omega C' \gg G'$ ) at 24 GHz. An overview of the fabrication and experimental characterization of this transmission line is given in Appendix 4.

### Appendix 4 - Prototyping and Measurement of Planar Structures

Throughout this work, the modeling and simulation results are validated with S-parameter measurements. For this purpose, planar antennas, transmission lines and shielding structures were manufactured and measured. This appendix gives an overview of the PCB manufacturing technology and measurement techniques that were employed.

All the planar structures were designed on a high frequency substrate material (RO4350B® from Rogers Cooperation) with two metallization layers suitable for low cost PCB technologies. A 250  $\mu\text{m}$  thick substrate was selected with favorable dielectric properties for high frequency applications. The substrate was laminated with 17.5  $\mu\text{m}$  thick copper on both sides by the manufacturer. The relative dielectric constant  $\epsilon_r$  and loss tangent  $\tan(\delta)$  are approximately 3.75 and 0.006 in the frequency range considered in this work, respectively.

The manufacturing process of the planar test structures comprises a number of steps. First, the copper was structured from both sides with a laser (Protolaser S from LPKF Laser & Electronics) as defined by the layout. Then, holes were drilled at the positions where vias, connecting the top and bottom layers, are to be placed. Next, a conductive paste (ProConduct® from LPKF Laser & Electronics) was applied to fill the holes. The test structures were then placed on a vacuum table to coat the inner sides of the drilled holes. Finally, the test structures were placed into an oven for 30 minutes with a temperature of 160 °C to cure the vias. Once this process is completed, the test structures are ready for the S-parameter measurements.

The measurements were conducted with a vector network analyzer (PNA 8361A from Agilent Technologies), which is capable of measuring S-parameters up to 67 GHz. With the additional S-parameter test set, four port S-parameter measurements can also be conducted. The planar test structures were placed on the wafer chuck of a prober station. The LRRM (line, reflect, reflect, match) and SOLT (short, open, load, thru) calibration techniques [109] were used to set the reference planes to the ends of the measurements tips. The S-parameters can then be measured from these reference planes. Figure 82 shows a photo of the GSG (ground, signal,

ground) probes that were used to measure the structures. These probes have a pitch of  $300\text{ }\mu\text{m}$ .

For the calibration of the network analyzer, an impedance standard substrate (106-683) from Cascade Microtech was used. It contains all necessary standards including opens, shorts, loads, thru and lines.



**Figure 82: Photo of a GSG probe to contact the measurement structures.**

In order to contact the test structures with the GSG probe, an adapter structure was designed and implemented. All the planar structures in this work comprise grounded microstrip-type configurations. Therefore, the adapters were designed as planar pads, and the ground pads were shorted to the ground plane with two vias. The adapters are depicted in Figure 83 together with two designed  $50\text{ }\Omega$  microstrip transmission lines (see Appendix 3) of different lengths (1 mm and 5 mm), which were measured to show the transmission and reflection characteristics of the adapters and the microstrip lines. The reference planes are also shown, indicating the position of the probe tips.

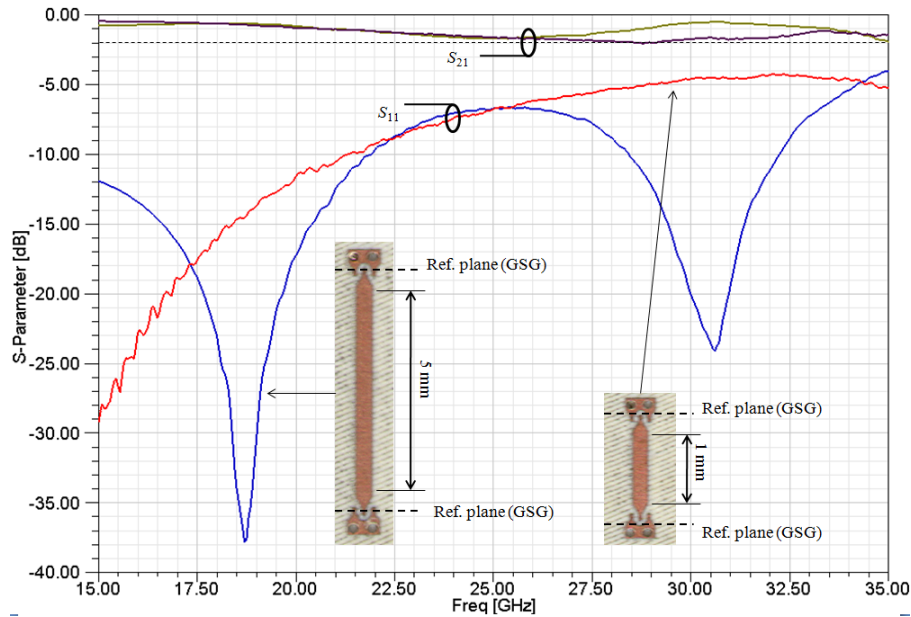


**Figure 83: Measured transmission and reflection coefficient of the manufactured microstrip transmission lines.**

## Appendices

Up to a frequency of approximately 27 GHz the reflection coefficients  $S_{11}$  are below -6 dB. This implies that less than 25 % of the input power is reflected at the probe tips. The transmission coefficients  $S_{21}$  of both lines are below 2 dB up to 35 GHz. Furthermore, the transmission coefficients are similar for both line lengths.

## References

- [1] G. Xiang, H. Hashemi, and A. Hajimiri, "A fully integrated 24-GHz eight-element phased-array receiver in silicon," *IEEE Journal of Solid-State Circuits*, vol. 39, pp. 2311-2320, 2004.
- [2] S. K. Reynolds, B. A. Floyd, U. R. Pfeiffer, T. Beukema, J. Grzyb, C. Haymes, B. Gaucher, and M. Soyuer, "A Silicon 60-GHz Receiver and Transmitter Chipset for Broadband Communications," *IEEE Journal of Solid-State Circuits*, vol. 41, pp. 2820-2831, 2006.
- [3] U. R. Pfeiffer, J. Grzyb, L. Duixian, B. Gaucher, T. Beukema, B. A. Floyd, and S. K. Reynolds, "A chip-scale packaging technology for 60-GHz wireless chipsets," *IEEE Transactions on Microwave Theory and Techniques*, vol. 54, pp. 3387-3397, 2006.
- [4] A. Natarajan, A. Komijani, X. Guan, A. Babakhani, and A. Hajimiri, "A 77-GHz Phased-Array Transceiver With On-Chip Antennas in Silicon: Transmitter and Local LO-Path Phase Shifting," *IEEE Journal of Solid-State Circuits*, vol. 41, pp. 2807-2819, 2006.
- [5] A. Babakhani, X. Guan, A. Komijani, A. Natarajan, and A. Hajimiri, "A 77-GHz Phased-Array Transceiver With On-Chip Antennas in Silicon: Receiver and Antennas," *IEEE Journal of Solid-State Circuits*, vol. 41, pp. 2795-2806, 2006.
- [6] S. Yaoming, F. Herzel, J. Borngraber, and R. Kraemer, "60 GHz Receiver Building Blocks in SiGe BiCMOS," presented at Topical Meeting on Silicon Monolithic Integrated Circuits in RF Systems, 2007.
- [7] M. Devulder, N. Deparis, I. Telliez, S. Pruvost, N. Rolland, F. Danneville, and P. A. Rolland, "60 GHz UWB Transmitter for Use in WLAN Communication," presented at International Symposium on Signals, Systems and Electronics, 2007.
- [8] K. Kornegay, "60 GHz radio design challenges," presented at 25th Annual Technical Digest Gallium Arsenide Integrated Circuit (GaAs IC) Symposium, 2003.
- [9] R. R. Tummala, M. Swaminathan, M. M. Tentzeris, J. Laskar, C. Gee-Kung, S. Sitaraman, D. Keezer, D. Guidotti, H. Zhaoran, L. Kyutae, W. Lixi, S. K. Bhattacharya, V. Sundaram, L. Fuhan, and P. M. Raj, "The SOP for miniaturized, mixed-signal computing, communication, and consumer systems of the next decade," *IEEE Transactions on Advanced Packaging*, vol. 27, pp. 250-267, 2004.



- [10] K. Wincza, S. Gruszczynski, J. Borgosz, J. Hallatt, and I. Aldred, "Design of electromagnetically coupled corner-series-fed antenna arrays with the application for 24 GHz doppler sensors," presented at Antennas and Propagation International Symposium, 2007.
- [11] J. Wernehag and H. Sjoland, "A 24-GHz Automotive Radar Transmitter with Digital Beam Steering in 130-nm CMOS," presented at Research in Microelectronics and Electronics, 2006.
- [12] M. Slovic, B. Jokanovic, and B. Kolundzija, "High efficiency patch antenna for 24 GHz anticollision radar," presented at 7th International Conference on Telecommunications in Modern Satellite, Cable and Broadcasting Services, 2005.
- [13] M. R. Nezhad Ahamdi and S. Safavi-Naeini, "On-chip antennas for 24, 60, and 77 GHz single package transceivers on low resistivity silicon substrate," presented at Antennas and Propagation International Symposium, 2007.
- [14] W. Menzel and P. J. N. Vera, "A 24 GHz Microstrip Antenna Array Incorporating a Ridge Waveguide Feed Network," presented at European Microwave Conference, 1999.
- [15] W. Mayer, A. Gronau, W. Menzel, and H. Leier, "A Compact 24 GHz Sensor for Beam-Forming and Imaging," presented at 9th International Conference on Control, Automation, Robotics and Vision, 2006.
- [16] H. Krishnaswamy and H. Hashemi, "A Fully Integrated 24GHz 4-Channel Phased-Array Transceiver in 0.13  $\mu\text{m}$  CMOS Based on a Variable-Phase Ring Oscillator and PLL Architecture," presented at IEEE International Solid-State Circuits Conference, 2007.
- [17] S. Holzwarth, R. Kulke, and J. Kassner, "Integrated stacked patch antenna array on LTCC material operating at 24 GHz," presented at Antennas and Propagation Society International Symposium, 2004.
- [18] H. Hashemi, X. Guan, and A. Hajimiri, "A fully integrated 24 GHz 8-path phased-array receiver in silicon," presented at Solid-State Circuits Conference, 2004.
- [19] I. Gresham, A. Jenkins, R. Egri, C. Eswarappa, F. Kolak, R. Wohler, J. Bennett, and J. P. Lanteri, "Ultra wide band 24 GHz automotive radar front-end," presented at Radio Frequency Integrated Circuits (RFIC) Symposium, 2003.

- [20] P. R. Grajek, B. Schoenlinner, and G. M. Rebeiz, "A 24-GHz high-gain Yagi-Uda antenna array," *IEEE Transactions on Antennas and Propagation*, vol. 52, pp. 1257-1261, 2004.
- [21] W. Chuang, Q. Rong, Y. Ming-hui, Yun Sun, Jian-zhong Gu, and Xiao-wei Sun, "A low cost 24-GHz FMCW radar for automobile application," presented at European Radar Conference, 2005.
- [22] C. Cao, Y. Ding, X. Yang, J. J. Lin, A. Verma, J. Lin, F. Martin, and O. K, "A 24-GHz Transmitter with an On-Chip Antenna in 130-nm CMOS," 2006.
- [23] A. Vimpari, A. Lamminen, and J. Saily, "Design and Measurements of 60 GHz Probed Patch Antennas on Low-Temperature Co-Fired Ceramic Substrates," presented at Microwave Conference, 2006.
- [24] S. Holzwarth and L. Baggen, "Planar antenna design at 60 GHz for high data rate point-to-point connections," presented at Antennas and Propagation Society International Symposium, 2005.
- [25] F. Ohnimus, I. Ndip, S. Guttowski, and H. Reichl, "An efficient and broadband slot antenna for 60 GHz wireless applications," presented at Electrical Design of Advanced Packaging and Systems Symposium, 2008.
- [26] Q. Yongxi and E. Yamashita, "A 60 GHz imaging array using CPW-fed twin-slots on multilayered substrates," presented at Microwave Symposium Digest, 1996.
- [27] Y. P. Zhang, M. Sun, K. M. Chua, L. L. Wai, and D. X. Liu, "Integration of slot antenna in LTCC package for 60 GHz radios," *Electronics Letters*, vol. 44, pp. 330-331, 2008.
- [28] C. Eswarappa, "Balanced antenna arrays for 24 GHz automotive UWB radar sensors," presented at Antennas and Propagation International Symposium, 2007.
- [29] J. Grzyb, L. Duxian, U. Pfeiffer, and B. Gaucher, "Wideband Cavity-backed Folded Dipole Superstrate Antenna for 60 GHz Applications," presented at Antennas and Propagation International Symposium, 2006.
- [30] J. Grzyb, L. Duixian, and B. Gaucher, "Packaging effects of a broadband 60 GHz cavity-backed folded dipole superstrate antenna," presented at Antennas and Propagation Society International Symposium, 2007.
- [31] C. Karnfelt, P. Hallbjorner, H. Zirath, P. Ligander, K. Boustedt, and A. Alping, "High gain active microstrip antenna for 60 GHz WLAN," presented at European Microwave Conference, 2005.

- [32] C. Karnfelt, P. Hallbjorner, H. Zirath, and A. Alping, "High gain active microstrip antenna for 60-GHz WLAN/WPAN applications," *IEEE Transactions on Microwave Theory and Techniques*, vol. 54, pp. 2593--2603, 2006.
- [33] P. Coquet, R. Sauleau, K. Shinohara, H. Lhermite, and T. Matsui, "Multi-layer microstrip antennas on quartz substrates: Technological considerations and performances at 60 GHz," *Microwave and Optical Technology Letters*, vol. 40, pp. 41-47, 2004.
- [34] T. Seki, N. Honma, K. Nishikawa, and K. Tsunekawa, "A 60-GHz multilayer parasitic microstrip array antenna on LTCC substrate for system-on-package," *Microwave and Wireless Components Letters*, vol. 15, pp. 339-341, 2005.
- [35] T. Seki, K. Nishikawa, I. Toyoda, and S. A. Kubota, "Microstrip Array Antenna with Parasitic Elements Alternately Arranged Over Two Layers of LTCC Substrate for Millimeter Wave Applications," presented at Radio and Wireless Symposium, 2007.
- [36] M. Al-Tikriti, S. Koch, and M. Uno, "A compact broadband stacked microstrip array antenna using eggcup-type of lens," *Microwave and Wireless Components Letters, IEEE*, vol. 16, pp. 230-232, 2006.
- [37] K. Jeong-Geun, L. Hyung Suk, L. Ho-Seon, A. Jun-Bo Yoon, and S. Hong, "60-GHz CPW-fed post-supported patch antenna using micromachining technology," *Microwave and Wireless Components Letters, IEEE*, vol. 15, pp. 635-637, 2005.
- [38] L. Hyung Suk, K. Jeong-Geun, H. Songcheol, and J.-B. Yoon, "Micromachined CPW-fed suspended patch antenna for 77 GHz automotive radar applications," presented at European Microwave Conference, 2005.
- [39] M. Caillet, O. Lafond, and M. Himdi, "Reconfigurable Microstrip Antennas in Millimeter Waves," presented at IEEE International Microwave Symposium Digest, 2006.
- [40] L. Le Garrec, M. Himdi, R. Sauleau, L. Mazonq, K. Grenier, and R. Plana, "CPW-fed slot microstrip MEMS-based reconfigurable arrays," presented at Antennas and Propagation Society International Symposium, 2004.
- [41] J.-Y. Park, Y. Wang, and T. Itoh, "A 60 GHz integrated antenna array for high-speed digital beamforming applications," presented at Microwave Symposium Digest, 2003.
- [42] I. Ndip, M. Hirte, S. Guttowski, and H. Reichl, "On the integration of a 2.4 GHz ISM band antenna in proximity to transmission lines," presented at 3rd European Conference on Antennas and Propagation, 2009.

- [43] I. Ndip, H. Reichl, and S. Guttowski, "A Novel Methodology for Defining the Boundaries of Geometrical Discontinuities in Electronic Packages," presented at Research in Microelectronics and Electronics 2006, Ph. D., 2006.
- [44] I. Ndip, "Novel Methodologies for Efficient and Accurate Modeling and Optimization of System-in-Package Modules for RF/High-Speed Applications," Technical University of Berlin, 2006.
- [45] B. C. Wadell, *Transmission Line Design Handbook*: Artech House, Inc., 1991.
- [46] X. Li and L. Yinzhao, "Transient Response of a Multiconductor Transmission Line With Nonlinear Terminations Excited by an Electric Dipole," *IEEE Transactions on Electromagnetic Compatibility*, vol. 51, pp. 805-810, 2009.
- [47] A. K. Agrawal, H. J. Price, and S. H. Gurbaxani, "Transient Response of Multiconductor Transmission Lines Excited by a Nonuniform Electromagnetic Field," *IEEE Transactions on Electromagnetic Compatibility*, vol. EMC-22, pp. 119-129, 1980.
- [48] C. W. Harrison and C. D. Taylor, "Response of a Terminated Transmission Line Excited by a Plane Wave Field for Arbitrary Angles of Incidence," *IEEE Transactions on Electromagnetic Compatibility*, vol. EMC-15, pp. 118-120, 1973.
- [49] C. W. Harrison and C. D. Taylor, "Multiconductor Antenna Transmission Lines with Arbitrarily Positioned Load Impedances in an Incident Field," *IEEE Transactions on Electromagnetic Compatibility*, vol. EMC-15, pp. 121-126, 1973.
- [50] C. Taylor, R. Satterwhite, and C. Harrison, Jr., "The response of a terminated two-wire transmission line excited by a nonuniform electromagnetic field," *IEEE Transactions on Antennas and Propagation*, vol. 13, pp. 987-989, 1965.
- [51] F. Rachidi, "Formulation of the field-to-transmission line coupling equations in terms of magnetic excitation field," *IEEE Transactions on Electromagnetic Compatibility*, vol. 35, pp. 404-407, 1993.
- [52] M. Leone and H. L. Singer, "On the coupling of an external electromagnetic field to a printed circuit board trace," *IEEE Transactions on Electromagnetic Compatibility*, vol. 41, pp. 418-424, 1999.
- [53] F. M. Tesche, "On the Analysis of a Transmission Line With Nonlinear Terminations Using the Time-Dependent BLT Equation," *IEEE Transactions on Electromagnetic Compatibility*, vol. 49, pp. 427-433, 2007.

- [54] L. Ying, N. Gu-Yan, L. Jian-Shu, Z. Xu-Feng, and S. Ji-Yuan, "The terminal responses of the two-wire transmission line in a cavity with apertures illuminated by a plane wave," presented at 3rd IEEE International Symposium on Microwave, Antenna, Propagation and EMC Technologies for Wireless Communications, 2009.
- [55] C. R. Paul, "Frequency Response of Multiconductor Transmission Lines Illuminated by an Electromagnetic Field," *IEEE Transactions on Electromagnetic Compatibility*, vol. EMC-18, pp. 183-190, 1976.
- [56] F. M. Tesche, M. V. Ianoz, and T. Karlsson, *EMC Analysis Methods and Computational Techniques*: John Wiley and Sons, Inc., 1997.
- [57] S. Grivet-Talocia, M. Bandinu, F. Canavero, I. Kelandar, and P. Kotiranta, "Fast Assessment of Antenna-PCB Coupling in Mobile Devices: a Macromodeling Approach," presented at International Symposium on Electromagnetic Compatibility, 2009.
- [58] D. Pozar, "Considerations for millimeter wave printed antennas," *IEEE Transactions on Antennas and Propagation*, vol. 31, pp. 740-747, 1983.
- [59] A. J. M. Soares, S. B. d. A. Fonseca, and A. J. Giarola, "Surface wave excitation on a microstrip ring antenna," *IEEE Transactions on Antennas and Propagation*, vol. 37, pp. 1310-1312, 1989.
- [60] G. V. Eleftheriades and Q. Meide, "Efficiency and gain of slot antennas and arrays on thick dielectric substrates for millimeter-wave applications: a unified approach," *IEEE Transactions on Antennas and Propagation*, vol. 50, pp. 1088-1098, 2002.
- [61] Y. Fan and Y. Rahmat-Samii, "Microstrip antennas integrated with electromagnetic band-gap (EBG) structures: a low mutual coupling design for array applications," *IEEE Transactions on Antennas and Propagation*, vol. 51, pp. 2936-2946, 2003.
- [62] Z. Fangming, X. Ya, and Y. Juanjuan, "Performance improvement of microstrip patch antenna and array with electromagnetic bandgap structure," presented at International Conference on Microwave and Millimeter Wave Technology, 2008.
- [63] J. Itoh, N. Michishita, and H. Morishita, "A study on mutual coupling reduction between two inverted-F antennas using mushroom-type EBG structures," presented at Antennas and Propagation Society International Symposium, 2008.
- [64] G. Ruvio and M. J. Ammann, "Performance characterization for patch antenna systems with a limited number of EBG cells using the mushroom-like structure as

- benchmark," presented at Antennas and Propagation Society International Symposium, 2007.
- [65] D. Sievenpiper, Z. Lijun, R. F. J. Broas, N. G. Alexopolous, and E. Yablonovitch, "High-impedance electromagnetic surfaces with a forbidden frequency band," *Microwave Theory and Techniques*, vol. 47, pp. 2059-2074, 1999.
- [66] E. Rajo-Iglesias, O. Quevedo-Teruel, and L. Inclan-Sanchez, "Study of mutual coupling reduction in single and stacked multilayer patch antennas by using planar EBG structures," presented at Antennas and Propagation Society International Symposium, 2007.
- [67] E. Rajo-Iglesias, O. Quevedo-Teruel, L. Inclan-Sanchez, and L. E. Garcia-Munoz, "Design of a Planar EBG Structure to Reduce Mutual Coupling in Multilayer Patch Antennas," presented at Antennas and Propagation Conference, 2007.
- [68] K. Payandehjoo and R. Abhari, "Suppression of substrate coupling between slot antennas using electromagnetic bandgap structures," presented at Antennas and Propagation Society International Symposium, 2008.
- [69] M. F. Abedin and M. Ali, "Reducing the mutual-coupling between the elements of a printed dipole array using planar EBG structures," presented at Antennas and Propagation Society International Symposium, 2005.
- [70] Y. Ang and Z. Xuexia, "A novel 2-D electromagnetic band-gap structure and its application in micro-strip antenna arrays," presented at 3rd International Conference on Microwave and Millimeter Wave Technology, 2002.
- [71] R. Coccioli, Y. Fei-Ran, M. Kuang-Ping, and T. Itoh, "Aperture-coupled patch antenna on UC-PBG substrate," *IEEE Transactions on Microwave Theory and Techniques*, vol. 47, pp. 2123-2130, 1999.
- [72] N. Llombart, A. Neto, G. Gerini, and P. de Maagt, "Planar circularly symmetric EBG structures for reducing surface waves in printed antennas," *IEEE Transactions on Antennas and Propagation*, vol. 53, pp. 3210-3218, 2005.
- [73] N. Llombart, A. Neto, G. Gerini, and P. De Maagt, "Bandwidth, efficiency and directivity enhancement of printed antenna performance using planar circularly symmetric EBGs," presented at European Conference on Wireless Technology, 2005.
- [74] R. Zhang, D. G. Fang, K. L. Wu, and W. X. Sheng, "Study on the elimination of surface wave by metal fences," presented at Asia-Pacific Conference on Environmental Electromagnetics, 2000.

- [75] C. Younkyu, J. Seong-Sik, D. Ahn, C. Jae-Ick, and T. Itoh, "High isolation dual-polarized patch antenna using integrated defected ground structure," *Microwave and Wireless Components Letters*, vol. 14, pp. 4-6, 2004.
- [76] L. Haiwen, L. Zhengfan, S. Xiaowei, and M. Junfa, "Harmonic suppression with photonic bandgap and defected ground structure for a microstrip patch antenna," *Microwave and Wireless Components Letters*, vol. 15, pp. 55-56, 2005.
- [77] S. Mohsen, M. Alireza, T. Ahad, and H. Teimur, "Mutual Coupling Reduction of Microstrip Antennas using Defected Ground Structure," presented at 10th IEEE Singapore International Conference on Communication Systems, 2006.
- [78] H. Y. D. Yang and J. Wang, "Surface waves of printed antennas on planar artificial periodic dielectric structures," *IEEE Transactions on Antennas and Propagation*, vol. 49, pp. 444-450, 2001.
- [79] D. G. Fang, C. Z. Luan, and Y. P. Xi, "Mutual coupling in microstrip antenna array: evaluation, reduction, correction or compensation," presented at IEEE International Workshop on Antenna Technology: Small Antennas and Novel Metamaterials, 2005.
- [80] P. Baccarelli, P. Burghignoli, G. Lovat, and S. Paulotto, "Surface-wave suppression in a double-negative metamaterial grounded slab," *Antennas and Wireless Propagation Letters, IEEE*, vol. 2, pp. 269-272, 2003.
- [81] I. Papapolymerou, R. F. Drayton, and L. P. B. Katehi, "Surface wave mode reduction for rectangular microstrip antennas," presented at Antennas and Propagation Society International Symposium, 1995.
- [82] D. R. Jackson, J. T. Williams, A. K. Bhattacharyya, R. L. Smith, S. J. Buchheit, and S. A. Long, "Microstrip patch designs that do not excite surface waves," *IEEE Transactions on Antennas and Propagation*, vol. 41, pp. 1026-1037, 1993.
- [83] L. Boccia, G. Amendola, and G. Di Massa, "Rectangular patch antennas with reduced surface wave radiation," presented at Antennas and Propagation Society International Symposium, 2005.
- [84] G. Amendola, L. Boccia, and G. Di Massa, "Shorted elliptical patch antennas with reduced surface waves on two frequency bands," *IEEE Transactions on Antennas and Propagation*, vol. 53, pp. 1946-1956, 2005.
- [85] M. A. Hickey, Q. Meide, and G. V. Eleftheriades, "A reduced surface-wave twin arc-slot antenna for millimeter-wave applications," *Microwave and Wireless Components Letters*, vol. 11, pp. 459-461, 2001.

- [86] C. Won-il, J. Dong Yun, and P. Chul Soon, "A surface wave reduced higher mode circular patch antenna for 60GHz LTCC SiP," presented at Asia-Pacific Microwave Conference, 2005.
- [87] R. F. Drayton, R. M. Henderson, and L. P. B. Katehi, "Monolithic packaging concepts for high isolation in circuits and antennas," *Microwave Theory and Techniques*, vol. 46, pp. 900-906, 1998.
- [88] L. Choon Sae, V. Nalbandian, and F. Schwering, "Gain enhancement of a thick microstrip antenna by suppressing surface waves," presented at Antennas and Propagation Society International Symposium, 1994.
- [89] R. G. Rojas and K. W. Lee, "Control of surface waves in planar printed antennas," presented at Antennas and Propagation Society International Symposium, 1998.
- [90] D. M. Kokotoff, R. B. Waterhouse, and J. T. Aberle, "On improving the surface wave efficiency of microstrip patches," presented at Antennas and Propagation Society International Symposium, 1997.
- [91] Y. H. Cho, P. Cheolsig, and C. Jaeick, "Gain enhancement of microstrip antenna using parasitic metallic bar," presented at Antennas and Propagation Society International Symposium, 2003.
- [92] L. Kyutae, A. Obatoyinbo, M. Davis, J. Laskar, and R. Tummala, "Development of planar antennas in multi-layer packages for RF-System-on-a-Package Applications," presented at Electrical Performance of Electronic Packaging, 2001.
- [93] C. A. Balanis, *Advanced Engineering Electromagnetics*, 1989.
- [94] C. A. Balanis, *Antenna Theory - Analysis and Design*, 2. ed, 1997.
- [95] W. L. Stutzman and G. A. Thiele, *Antenna Theory and Design*: John Wiley and Sons, Inc., 1981.
- [96] C. R. Paul, *Introduction to Electromagnetic Reliability*: John Wiley and Sons, Inc., 2006.
- [97] R. E. Collin, *Field Theory of Guided Waves*: McGraw-Hill Book Company, Inc., 1960.
- [98] R. F. Harrington, *Time-Harmonic Electromagnetic Fields*: John Wiley and Sons, Inc., 2001.
- [99] Y. Lo, D. Solomon, and W. Richards, "Theory and experiment on microstrip antennas," *IEEE Transactions on Antennas and Propagation*, vol. 27, pp. 137-145, 1979.



- [100] D. R. Jackson and N. G. Alexopoulos, "Simple approximate formulas for input resistance, bandwidth, and efficiency of a resonant rectangular patch," *IEEE Transactions on Antennas and Propagation*, vol. 39, pp. 407-410, 1991.
- [101] R. Suga, H. Nakano, Y. Hirachi, J. Hirokawa, and M. Ando, "Cost-Effective 60-GHz Antenna Package With End-Fire Radiation for Wireless File-Transfer System," *IEEE Transactions on Microwave Theory and Techniques*, vol. 58, pp. 3989-3995.
- [102] D. F. Sievenpiper, "High-impedance Electromagnetic Surfaces," UCLA, 1999.
- [103] P. Kovacs and Z. Raida, "Dispersion analysis of planar metallo-dielectric EBG structures in Ansoft HFSS," presented at Microwaves, Radar and Wireless Communications, 2008.
- [104] L. Brillouin, *Wave Propagation in Periodic Structures*: Dover Publications Inc., 1946.
- [105] G. Kumar and K. P. Ray, *Broadband Microstrip Antennas*: Artech House, Inc., 2003.
- [106] J. Jin, *The Finite Element Method in Electromagnetics*: John Wiley and Sons Inc., 1993.
- [107] D. G. Swanson and W. J. R. Hoefer, *Microwave Circuit Modeling Using Electromagnetic Field Simulation*: Artech House, 2003.
- [108] Z. S. Sacks, D. M. Kingsland, R. Lee, and J.-F. Lee, "A Perfectly Matched Anisotropic Absorber for the Use as an Absorbing Boundary Condition," *IEEE Transactions on Antennas and Propagation*, vol. 43, 1995.
- [109] S. A. Wartenberg, *RF Measurements of Die and Packages*: Artech House, 2002.

## List of Figures

Figure 1: Illustration of a compact wireless module based on a low cost PCB configuration...	2
Figure 2: Coupling between: (a) two transmission lines; and (b) a patch antenna and a transmission line at 24 GHz. ....	3
Figure 3: Cross sections of the three fundamental antenna types: (a) patch antenna on grounded substrate; (b) slot antenna in ground plane; and (c) dipole antenna on ungrounded substrate.....	4
Figure 4: Classification of techniques for the reduction of undesired electromagnetic coupling caused by surface waves. ....	8

Figure 5: Cross sections of configurations for surface wave suppression: (a) conventional substrate with ground plane; (b) integration of EBG structure; (c) integration of DGS; and (d) modification of substrate material.....	10
Figure 6: Illustration of the complex power density transfer to and from a planar antenna configuration integrated on a PCB. The coordinate system is centered, and the plane $z=0$ is on the ground plane. ....	13
Figure 7: Overview of approach to determine electromagnetic antenna boundary. ....	14
Figure 8: Equivalent circuit model of an infinitesimal transmission line piece with the distributed per-unit-length parameters. ....	19
Figure 9: Grounded substrate used for the calculation of surface wave fields. ....	25
Figure 10: Solutions of the transcendental equations for different values of $\epsilon_r$ and $h$ . ....	27
Figure 11: Longitudinal electric field of $TM_0$ surface wave with $\lambda=16.67$ mm ( $f=18$ GHz)...	28
Figure 12: Transverse electric field of $TM_0$ surface wave with $\lambda=16.67$ mm ( $f=18$ GHz). ....	28
Figure 13: Overview of coupling mechanisms between planar antennas and board components.....	31
Figure 14: Illustration of distributed nature of capacitive and inductive coupling from a resonant patch antenna. ....	31
Figure 15: Model of patch antenna on a grounded dielectric substrate. ....	32
Figure 16: Parameterized transmission line model of a conventional rectangular patch antenna for excitation with the $TM_{100}$ mode.....	34
Figure 17: Distribution of current density on the patch resonator with the "idealized" current excitation. ....	36
Figure 18: Simulation of the propagating power density excited by the patch antenna on the ground plane. ....	37
Figure 19: Simulation of the spatial complex power density excited by the patch antenna on the ground plane in region 1.....	37
Figure 20: Configuration of the coaxial probe feed and the inset distance $s$ from the patch edge. ....	38
Figure 21: Simulation of the normalized magnetic field excited by the patch antenna on the ground plane in region 1.....	39
Figure 22: Simulation of the normalized magnetic field excited by the patch antenna on the ground plane in region 2.....	39

Figure 23: Illustration of far-field waves radiated by a planar antenna configuration including: (a) the space wave mode; and (b) the surface wave mode. ....	41
Figure 24: Graphical illustration of the reactive power density, the threshold value for determining the electromagnetic antenna boundary as well as the antenna parameters. ....	43
Figure 25: Simulation model and dimensions of the 24 GHz inset fed patch antenna. ....	45
Figure 26: Measurement of the reflection coefficient $S_{11}$ of the patch antenna and comparison to full-wave simulation. The top view of the manufactured antenna with the feeding line and contact pads is also shown. ....	46
Figure 27: Simulation model and dimensions of the 24 GHz edge fed slot antenna. ....	47
Figure 28: Measurement of the reflection coefficient $S_{11}$ of the slot antenna and comparison to full-wave simulation. The top view of the manufactured antenna with the feeding line and contact pads is also shown. ....	47
Figure 29: Simulation model and dimensions of the 24 GHz center fed dipole antenna. ....	48
Figure 30: Measurement of the reflection coefficient $S_{11}$ of the dipole antenna and comparison to full-wave simulation. The top view of the manufactured antenna with the feeding line and contact pads is also shown. ....	49
Figure 31: Comparison of the simulated electric field distributions on the ground planes in the vicinity of the: (a) patch antenna; (b) slot antenna; and (c) dipole antenna. ....	49
Figure 32: Comparison of the simulated magnetic field distributions on the ground planes in the vicinity of the: (a) patch antenna; (b) slot antenna; and (c) dipole antenna. ....	50
Figure 33: Comparison of the simulated radiation patterns (gain) of the patch, slot and dipole antenna in two principle elevation planes. ....	51
Figure 34: Simulated reactive power density on the ground plane of the planar antennas. ....	52
Figure 35: Comparison between the physical and additional electrical sizes of the planar antennas. ....	54
Figure 36: Illustration of the planar antennas with microstrip transmission lines routed inside electromagnetic antenna boundary of the (a) patch and (b) slot antennas. ....	55
Figure 37: Effects on the resonance frequencies of the antennas for different transmission line separation distances $d$ . ....	56
Figure 38: Effects on the insertion loss of the microstrip transmission line routed inside the antenna boundaries. ....	56
Figure 39: Illustration of the planar antennas with reduced ground plane sizes. ....	57

Figure 40: Simulation results of the effects of reduced ground plane sizes on the antenna gains. ....	58
Figure 41: Overview of method to calculate coupling from antenna fields to transmission lines. ....	61
Figure 42: Illustration of method to calculate coupling from antenna fields to transmission lines. ....	61
Figure 43: Configuration of a microstrip transmission line on a grounded substrate. ....	62
Figure 44: Simulation of the magnetic field distribution of the patch antenna split up into the two tangential components on the ground plane. ....	68
Figure 45: Overview of the different cases used to study the coupling between the three planar antennas and the microstrip transmission lines. ....	69
Figure 46: Comparison of full-wave simulation with field integration (coupling model) results for the patch, slot and dipole antenna with $l = \lambda/4$ and $d = \lambda/4$ . ....	70
Figure 47: Comparison of full-wave simulation with field integration (coupling model) results for case 1. ....	71
Figure 48: Comparison of full-wave simulation with field integration (coupling model) results for case 2. ....	72
Figure 49: Comparison of full-wave simulation with field integration (coupling model) results for case 3. ....	72
Figure 50: Comparison of full-wave simulation with field integration (coupling model) results for case 4. ....	73
Figure 51: Overview of the patch antenna with the two transmission line routing cases with multiple bends. The $x$ - $y$ coordinates specify the segments of the transmission line. ....	73
Figure 52: Comparison of full-wave simulation with field integration (coupling model) results with spectral response for case 1. ....	74
Figure 53: Comparison of full-wave simulation with field integration (coupling model) results with spectral response for case 2. ....	75
Figure 54: 3D simulation models used to study the coupling to the ports for two transmission lines, (a) and (b), with and without the microstrip transmission line, respectively. ....	76
Figure 55: Test structures and 3D simulation models used for experimental verification of the simulated coupling between the patch antenna and the microstrip transmission lines. ....	77
Figure 56: 3D simulation models of the coupled patch antennas including: (1) E-plane case; and (2) H-plane case. ....	79

Figure 57: Simulation results of the coupling coefficient $S_{21}$ between the patch antennas at 24 GHz. ....	80
Figure 58: Physical and electrical concept of the mushroom-type EBG structure .....	81
Figure 59: Illustration of the Brillouin zone (left) for an EBG unit cell (right). ....	82
Figure 60: Full dispersion diagram for the space and surface wave modes of the EBG cell... ..	83
Figure 61: Model of E-plane patch antennas with integrated EBG for the suppression of coupling. ....	84
Figure 62: Simulation results of the coupling coefficient $S_{21}$ between the E-plane coupled patch antennas in dependency of the separation distance $a$ . ....	85
Figure 63: Simulation results of the coupling coefficient $S_{21}$ between the E-plane coupled patch antennas in dependency of the separation distance $a$ . ....	86
Figure 64: Configuration and dimensions of the designed SWR patch antenna. ....	87
Figure 65: Surface current distribution: on the excited (a) conventional patch antenna; and on the (b) SWR antenna. The arrows indicate the direction of the current anti nodes. ....	88
Figure 66: Measurement results of the reflection coefficient $S_{11}$ of the SWR patch antenna and comparison to full-wave simulation. ....	89
Figure 67: Simulation of the reactive power density on the ground plane of the SWR patch antenna. ....	90
Figure 68: 3D simulation models of the coupled antennas: (1) conventional patch antennas; and (2) SWR patch antennas. ....	90
Figure 69: Simulation results of the coupling coefficient $S_{21}$ between two conventional patch antennas and two SWR patch antennas. ....	91
Figure 70: Photos of the test structures used to measure the coupling: (1) conventional patch antennas; (2) patch antennas with EBG structure; and (3) SWR patch antennas. ....	92
Figure 71: Comparison of coupling measurement results: (a) conventional patch antennas; (b) patch antennas with EBG structure; and (c) SWR patch antennas. ....	92
Figure 72: Overview of the SWR patch antenna with the two microstrip transmission line routing cases with multiple bends. The $x$ - $y$ coordinates specify the absolute routing path of the transmission line. ....	94
Figure 73: Overview of an optimized design process for planar antenna integration including the approaches, methods and results proposed in this work. ....	96
Figure 74: Concept of PML boundary conditions at the sides of the computational domain to provide low reflections absorbing boundaries. ....	102

Figure 75: Concept of PML edge elements at the corner of the box. ....	103
Figure 76: Change in magnetic field strength on the ground plane of the patch antenna in region 1 in dependency of the computed passes. ....	106
Figure 77: Comparison of the automatically (left) and manually (right) generated meshes on the substrate. ....	107
Figure 78: Change in magnetic field strength on the ground plane of the patch antenna in region 1 for different solver settings. ....	107
Figure 79: Manufactured test board with patch antenna and monopole probes to measure the electric field strength at different positions on the substrate. ....	108
Figure 80: Measured electric field strengths at the monopole probes on the test board of the patch antenna. ....	108
Figure 81: Configuration of a microstrip line on the grounded substrate configuration with dimensions. ....	109
Figure 82: Photo of a GSG probe to contact the measurement structures. ....	111
Figure 83: Measured transmission and reflection coefficient of the manufactured microstrip transmission lines. ....	111

## List of Tables

Table 1: Summary of the spatial field decay rates near excited planar antennas. ....	41
Table 2: Comparison of the simulated parameters of the planar antennas at 24 GHz. ....	51
Table 3: Comparison of the calculated threshold values. ....	52
Table 4: Deduced dimensions of the electromagnetic antenna boundary of the antennas. ....	53
Table 5: Comparison of the calculated, simulated and measured coupling values between the patch antenna and microstrip transmission lines at 24 GHz. ....	77
Table 6: Deduced electromagnetic antenna boundary values of the SWR patch antenna and comparison to the conventional patch antenna. ....	90
Table 7: Evaluated coupling values of the three configurations. ....	93
Table 8: Comparison of shielding effectiveness and required board space between EBG structure and SWR patch antenna. ....	93
Table 9: Comparison of simulated coupling to the transmission lines for cases 1 and 2. ....	95
Table 10: Computed transmission line parameters at 24 GHz. ....	109

## Short Biography and List of Publications



Florian Ohnimus was born in Lüneburg, Germany. He received the Dipl.-Ing. degree in electrical engineering (with honors) in 2007 from the Technical University of Berlin (TUB), Germany. Since April 2007, he has been working as a research engineer in the RF and High-Speed System Design Group (RSD) at the Fraunhofer Institute for Reliability and Microintegration (IZM) and the Berlin Center of Advanced Packaging (BeCAP). Mr. Ohnimus is recipient of the Studienpreis des Jahres 2007 from the TUB, the Erwin-Stephan-Preis 2008 and the Best Paper Prize of the Loughborough Antennas and Propagation Conference 2010.

### Publications related to Dissertation

- F. Ohnimus, G. Fotheringham, I. Ndip, E. Engin, S. Guttowski, H. Reichl, K.-D. Lang, “Integration of Planar Antennas Considering Electromagnetic Interactions at Board Level, *IEEE Transactions on Electromagnetic Compatibility*, March, 2011.
- F. Ohnimus, I. Ndip, E. Engin, S. Guttowski, H. Reichl, “Modeling and Analysis of Electromagnetic Field Distribution in Vicinity of Patch Antennas at Millimeter-wave Frequencies”, presented at IEEE International Symposium on Microelectronics (IMAPS), San Jose, USA, November, 2009.
- F. Ohnimus, I. Ndip, E. Engin, S. Guttowski, H. Reichl, “Study of Shielding Effectiveness of Mushroom-type Electromagnetic Bandgap Structures in Close Proximity to Patch Antennas”, presented at IEEE Loughborough Antennas and Propagation Conference, Loughborough, UK, November, 2009.
- F. Ohnimus, I. Ndip, E. Engin, S. Guttowski, H. Reichl, “Comparison of Electromagnetic Field Distribution in Vicinity of Patch and Slot Antennas”, presented at IEEE Loughborough Antennas and Propagation Conference, Loughborough, UK, November, 2009.
- F. Ohnimus, U. Maaß, I. Ndip, S. Guttowski, H. Reichl, “Planar Antenna Design and Integration for Millimeter-wave Communication Systems”, presented at Wireless Congress, Munich, October, 2009.
- F. Ohnimus, I. Ndip, S. Guttowski, H. Reichl, “Integration of Planar Millimeter-wave Antennas considering Electromagnetic Reliability Aspects”, Smart System Integration and Reliability - Honorary Volume on the Occasion of Herbert Reichl's 65th Birthday: Goldenbogen Verlag, Dresden, 2010.

### Publications, Workshops and Talks related to other Research Activities

- F. Ohnimus, C. Hoherz, M. Hampicke, I. Ndip, S. Guttowski, K.-D. Lang, D. Lumbeck, M. Kreitmair, “Integration and Evaluation of Electrically Small 868 MHz PCB Antennas for Wireless USB Stick”,

accepted for presentation at IEEE European Microwave Conference (EuMC), Manchester, UK, October 9-14, 2011.

- F. Ohnimus, I. Ndip, A. Podlasly, A. Ostmann, T. Fritzsche, J. Wolf, S. Guttowski, K.-D. Lang, "Design and Comparison of Efficient and Compact Patch Antennas for 24 GHz Radar and Communication Systems", presented at Smart Systems Integration Conference (SSI 2011), Dresden, Germany, March 22-23, 2011.
- G. Fotheringham, C. Tschoban, F. Ohnimus, I. Ndip, S. Guttowski, K.-D. Lang, U. Fotheringham, M. Letz, "Extraction of Dielectric Properties of Glass Substrates for RF Applications up to 40 GHz using a Split-Cylinder-Resonator", presented at Smart Systems Integration Conference (SSI 2011), Dresden, Germany, March 22-23, 2011.
- F. Ohnimus, U. Maaß, G. Fotheringham, B. Curran, I. Ndip, T. Fritzsche, J. Wolf, S. Guttowski, K.-D. Lang, "Design and Comparison of 24 GHz Patch Antennas on Glass Substrates for Compact Wireless Sensor Nodes", *International Journal of Microwave Science and Technology*, Hindawi, December, 2010.
- F. Ohnimus, R. Erxleben, C. Tschoban, I. Ndip, M. Niedermayer, H. Scholtz, T. Bonin, S. Guttowski, K.-D. Lang, "Design and Characterization of a Low Profile Miniaturized UHF PIFA for Compact Wireless Sensor Nodes", presented at IEEE Loughborough Antennas and Propagation Conference, Loughborough, UK, November, 2010.
- F. Ohnimus, J. Haberland, C. Tschoban, I. Ndip, K. Heumann, C. Kallmayer, S. Guttowski, K.-D. Lang, "Design and Characterization of a Small Encapsulated UHF RFID Tag for Wood Log Monitoring", presented at IEEE Loughborough Antennas and Propagation Conference, Loughborough, UK, November, 2010.
- G. Fotheringham, F. Ohnimus, I. Ndip, S. Guttowski, H. Reichl, „RFID - Theoretische Konzepte und Anwendungsbeispiele, Jahrbuch Oberflächentechnik“, Galvanotechnik: Leuze Verlag, Ausgabe 10/10, Oktober, 2010.
- I. Ndip, F. Ohnimus, K. Löbbicke, M. Bierwirth, C. Tschoban, S. Guttowski, H. Reichl, K. D. Lang, and H. Henke, "Modeling, Quantification, and Reduction of the Impact of Uncontrolled Return Currents of Vias Transiting Multilayered Packages and Boards," *IEEE Transactions on Electromagnetic Compatibility*, vol. 52, pp. 421-435, May, 2010.
- I. Ndip, F. Ohnimus, K. Löbbicke, C. Tschoban, M. Bierwirth, S. Guttowski, H. Reichl, "Equivalent Circuit Modeling of Signal Vias Considering their Return-Current Paths", presented at IEEE Asia-Pacific International Symposium on Electromagnetic Compatibility, Beijing, China, April 12-16, 2010.
- I. Ndip, K. Löbbicke, M. Bierwirth, C. Tschoban, B. Curran, R. Erxleben, F. Ohnimus, U. Maaß, G. Fotheringham, S. Guttowski, H. Reichl, "Managing the Return-Currents of Signal Vias in Organic and Silicon Substrates", presented at Smart Systems Integration Conference (SSI 2010), Como, Italy, March 23-24, 2010.
- F. Ohnimus, G. Fotheringham, I. Ndip, S. Guttowski, H. Reichl, "Comprehensive Design Method for RFID Tags based on EM Field Simulations", presented at Ansys/Ansoft Workshop, Leipzig, November 18-20, 2009.
- F. Ohnimus, A. Podlasly, J. Bauer, A. Ostmann, I. Ndip, S. Guttowski, H. Reichl, "Electrical Design and Characterization of Elevated Antennas at PCB-Level", presented at IEEE Electrical Components and Technology Conference (ECTC), San Diego, USA, May, 2009.



- G. Fotheringham, F. Ohnimus, I. Ndip, S. Guttowski, H. Reichl, “Parameterization of Bent Coils on Curved Flexible Substrates for RFID Applications”, presented at IEEE Electrical Components and Technology Conference (ECTC), San Diego, USA, May, 2009.
- F. Ohnimus, I. Ndip, S. Guttowski, H. Reichl, “Design Challenges and Techniques for Passive RFID Tag Antennas”, presented at Semiconductor Conference Dresden, April 29-30, 2009.
- F. Ohnimus, I. Ndip, S. Guttowski, H. Reichl, “An Efficient and Broadband Slot Antenna for 60 GHz Applications”, presented at IEEE Conference on Electrical Design of Advanced Packaging and Systems (EDAPS), Seoul, South Korea, December, 2008.
- I. Ndip, F. Ohnimus, S. Guttowski, H. Reichl, “Minimizing Electromagnetic Interference in Power-Ground Cavities”, presented at IEEE Conference on Electrical Design of Advanced Packaging and Systems (EDAPS), Seoul, South Korea, December, 2008.
- F. Ohnimus, I. Ndip, S. Guttowski, H. Reichl, “Design and Characterization of Integrated Antennas for Communication Applications”, presented at Inspiring Engineering - Ansoft Global Application Workshop for High Performance Electronic Design, Munich, November 10, 2008.
- F. Ohnimus, I. Ndip, S. Guttowski, H. Reichl, “Design and Analysis of a Bent Antenna-Coil for a HF RFID Transponder”, presented at IEEE European Microwave Conference (EuMC), Amsterdam, Netherlands, October, 2008.
- F. Ohnimus, I. Ndip, S. Guttowski, H. Reichl, “Entwurf integrierter Antennen für Kommunikations- und Radaranwendungen”, presented at Wireless Communication and Information (WCI), Berlin, October 15-16, 2008.
- F. Ohnimus, I. Ndip, S. Guttowski, H. Reichl, “Entwurf Integrierter Antennen für Kommunikations- und Radaranwendungen”, presented at RadioTecC 2008, Adlershof, Berlin, October 15-16, 2008.
- U. Maaß, F. Ohnimus, B. Curran, I. Ndip, S. Guttowski, H. Reichl, “Auswirkungen von Toleranzen der Aufbau- und Verbindungstechnik auf das elektrische Verhalten integrierter HF-Komponenten”, GMM-Fachtagung Zuverlässigkeit und Entwurf, Ingolstadt, 29.9.-1.10., VDE Verlag, 2008.
- I. Ndip, F. Ohnimus, S. Guttowski, H. Reichl, “Modeling and Analysis of Return-current Paths for Microstrip-to-Microstrip Via Transitions”, presented at IEEE Electronics System-Integration Technology Conference (ESTC), Greenwich, London, UK, September, 2008.
- I. Ndip, A. Ostmann, F. Ohnimus, U. Maaß, S. Guttowski, H. Reichl, “Elektrischer Entwurf von System-in-Package, Leiterplatten und Integrierten Komponenten für HF/High-Speed Anwendungen”, Workshop SMT/Hybrid/Packaging, Nuremberg, June 5, 2008.
- F. Ohnimus, I. Ndip, S. Guttowski, H. Reichl, “Modeling and Simulation of Integrated Antennas for RFID and Wireless Communication Applications”, Workshop on Antenna Simulations for Industrial Applications, Kaiserslautern, September 11, 2007.
- I. Ndip, F. Salhi, U. Maaß, G. Fotheringham, F. Ohnimus, S. Guttowski, and H. Reichl, “Optimal Electrical Design of System Packages and Integrated Components using the M3-Approach”, presented at IEEE Electronics Packaging Technology Conference (EPTC), Nevada, USA, June, 2007.